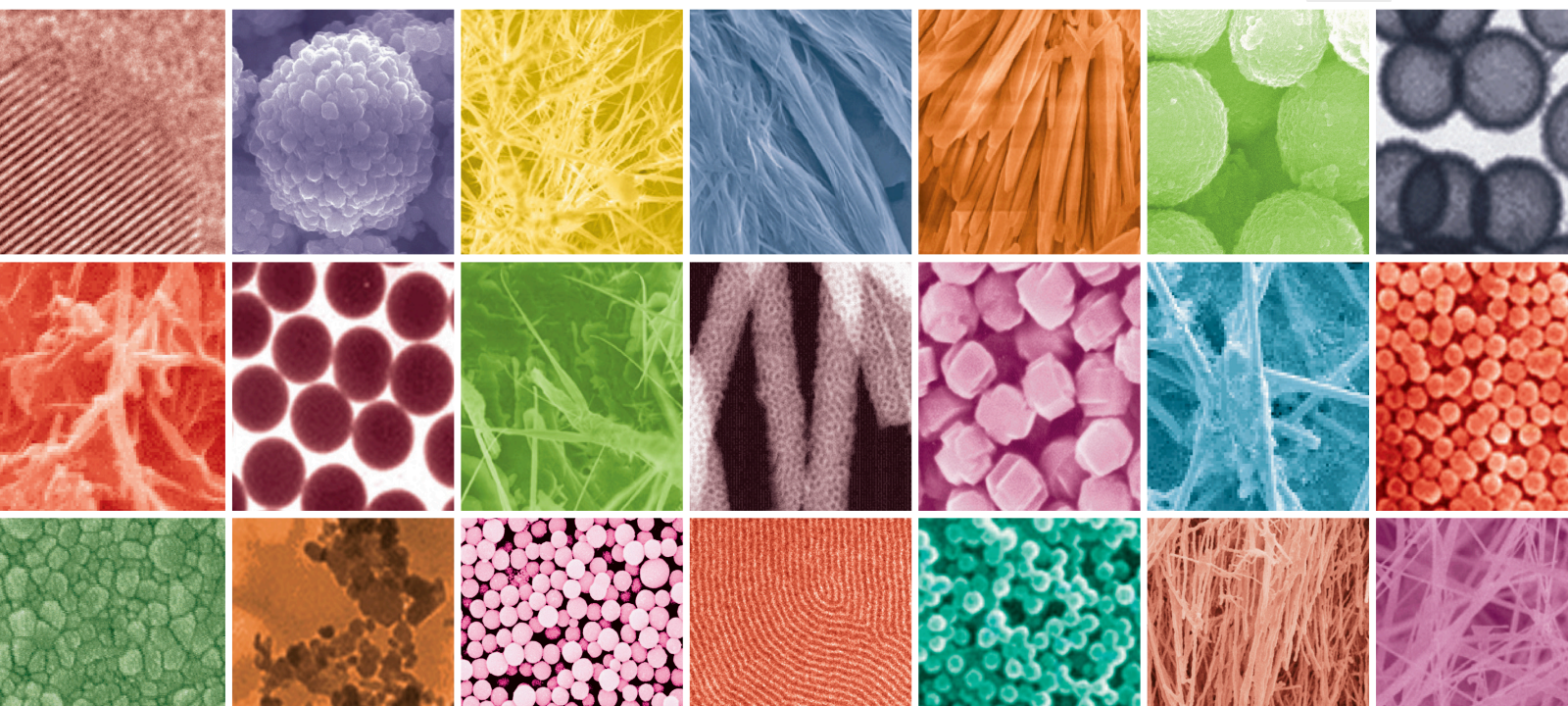


Cutting Edge Technologies by Silicon- and Silicon Oxide-Based Nanostructures

Lead Guest Editor: Francesca A. Scaramuzzo

Guest Editors: Arántzazu González-Campo and Alessandro Dell'Era





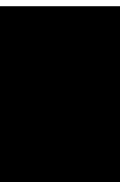
Cutting Edge Technologies by Silicon- and Silicon Oxide-Based Nanostructures

Journal of Nanomaterials

**Cutting Edge Technologies by Silicon-
and Silicon Oxide-Based Nanostructures**

Lead Guest Editor: Francesca A. Scaramuzzo

Guest Editors: Arántzazu González-Campo and
Alessandro Dell'Era



Copyright © 2021 Hindawi Limited. All rights reserved.

This is a special issue published in "Journal of Nanomaterials." All articles are open access articles distributed under the Creative Commons Attribution License, which permits unrestricted use, distribution, and reproduction in any medium, provided the original work is properly cited.

Editorial Board


Domenico Acierno, Italy
Katerina Aifantis, USA
Ibrahim Alarifi, Saudi Arabia
Nageh K. Allam, USA
Martin Andersson, Sweden
Raul Arenal, Spain
Ilaria Armentano, Italy
Hassan Azzazy, Egypt
Vincenzo Baglio, Italy
Lavinia Balan, France
Thierry Baron, France
Andrew R. Barron, USA
Stefano Bellucci, Italy
Enrico Bergamaschi, Italy
Debes Bhattacharyya, New Zealand
Sergio Bietti, Italy
Raghvendra A. Bohara, India
Mohamed Bououdina, Bahrain
Victor M. Castaño, Mexico
Albano Cavaleiro, Portugal
Bhanu P. S. Chauhan, USA
Shafiul Chowdhury, USA
Yu-Lun Chueh, Taiwan
Elisabetta Comini, Italy
Giuseppe Compagnini, Italy
David Cornu, France
Miguel A. Correa-Duarte, Spain
P. Davide Cozzoli, Italy
Anuja Datta, USA
Loretta L. Del Mercato, Italy
Yong Ding, USA
Yu Dong, Australia
Zehra Durmus, Turkey
Ovidiu Ersen, France
Ana Espinosa, France
Claude Estournès, France
Giuliana Faggio, Italy
Andrea Falqui, Saudi Arabia
Matteo Ferroni, Italy
Ilaria Fratoddi, Italy
Siddhartha Ghosh, Singapore
Filippo Giubileo, Italy
Fabien Grasset, Japan
Jean M. Greneche, France
Kimberly Hamad-Schifferli, USA
Simo-Pekka Hannula, Finland
Michael Harris, USA
Yasuhiko Hayashi, Japan
Michael Z. Hu, USA
Zafar Iqbal, USA
Balachandran Jeyadevan, Japan
Hassan Karimi-Maleh, Iran
Antonios Kelarakis, United Kingdom
Ali Khorsand Zak, Iran
Philippe Knauth, France
Prashant Kumar, United Kingdom
Eric Le Bourhis, France
Meiyong Liao, Japan
Shijun Liao, China
Silvia Licoccia, Italy
Nathan C. Lindquist, USA
Zainovia Lockman, Malaysia
Jim Low, Australia
Gaurav Mago, USA
Muhamamd A. Malik, United Kingdom
Ivan Marri, Italy
Laura Martinez Maestro, United Kingdom
Sanjay R. Mathur, Germany
Tony McNally, United Kingdom
Yogendra Mishra, Germany
Paulo Cesar Morais, Brazil
Paul Munroe, Australia
Jae-Min Myoung, Republic of Korea
Rajesh R. Naik, USA
Albert Nasibulin, Russia
Toshiaki Natsuki, Japan
Hiromasa Nishikiori, Japan
Sherine Obare, USA
Won-Chun Oh, Republic of Korea
Abdelwahab Omri, Canada
Ungyu Paik, Republic of Korea
Dillip K. Panda, USA
Mazeyar Parvinzadeh Gashti, Canada
Edward A. Payzant, USA

Alessandro Pegoretti, Italy
Oscar Perales-Pérez, Puerto Rico
Jorge Pérez-Juste, Spain
Alexey P. Popov, Finland
Thathan Premkumar, Republic of Korea
Helena Prima-García, Spain
Alexander Pyatenko, Japan
Haisheng Qian, China
You Qiang, USA
Philip D. Rack, USA
Mohammad Rahimi-Gorji, Belgium
Ilker S. Bayer, Italy
Lucien Saviot, France
Shu Seki, Japan
Gaurav Sharma, India
Donglu Shi, USA
Bhanu P. Singh, India
Surinder Singh, USA
Vladimir Sivakov, Germany
Adolfo Speghini, Italy
Kishore Sridharan, India
Marinella Striccoli, Italy
Andreas Stylianou, Cyprus
Fengqiang Sun, China
Ashok K. Sundramoorthy, India
Angelo Taglietti, Italy
Bo Tan, Canada
Leander Tapfer, Italy
Valeri P. Tolstoy, Russia
Muhammet S. Toprak, Sweden
Sri Ramulu Torati, Republic of Korea
R. Torrecillas, Spain
Achim Trampert, Germany
Takuya Tsuzuki, Australia
Tamer Uyar, USA
Luca Valentini, Italy
Antonio Vassallo, Italy
Ester Vazquez, Spain
Ajayan Vinu, Australia
Ruibing Wang, Macau
Magnus Willander, Sweden
Ping Xiao, United Kingdom
Zhi Li Xiao, USA
Yingchao Yang, USA
Hui Yao, China
Yoke K. Yap, USA
Dong Kee Yi, Republic of Korea


Jianbo Yin, China
William Yu, USA
Michele Zappalorto, Italy
Renyun Zhang, Sweden

Contents

Cutting Edge Technologies by Silicon- and Silicon Oxide-Based Nanostructures

Francesca A. Scaramuzzo , Arántzazu González-Campo , and Alessandro Dell'Era
Editorial (2 pages), Article ID 5478156, Volume 2021 (2021)

Electrochemical Characterization of Cu-Catalysed Si Nanowires as an Anode for Lithium-Ion Cells

P. P. Prosini, F. Rondino , M. Moreno, C. Cento, M. Ottaviani, A. Rufoloni, L. Pilloni, V. Orsetti, and A. Santoni
Research Article (9 pages), Article ID 4272090, Volume 2020 (2020)



Preparation of a Novel Thiol Surface Modifier and Fe₃O₄ Drug Loading Agent as well as Releasing under pH-Sensitivity

Wang Ya-zhen , Wu Xue-ying, Di Yu-tao, Lan Tian-yu, and Zu Li-wu
Research Article (14 pages), Article ID 5492953, Volume 2020 (2020)

Preparation and Thermal Decomposition Kinetics of Novel Silane Coupling Agent with Mercapto Group

Wu Xue-ying, Wang Ya-zhen , Di Yu-tao, Lan Tian-yu, and Zu Li-wu
Research Article (9 pages), Article ID 6089065, Volume 2019 (2019)

Ohmic Contact Mechanism for Ni/C-Faced 4H-n-SiC Substrate

Seongjun Kim, Hong-Ki Kim, Minwho Lim, Seonghoon Jeong, Min-Jae Kang, Min-Sik Kang, Nam-Suk Lee, Tran Viet Cuong , Hyunsoo Kim, Tobias Erlbacher, Anton Bauer, and Hoon-Kyu Shin 
Research Article (5 pages), Article ID 5231983, Volume 2019 (2019)

Comprehensive Study of Kinetics of Processes Competing during PECVD Ultrathin Silicon Layer High-Temperature Annealing

Romuald B. Beck  and Kamil Ber
Research Article (12 pages), Article ID 9628984, Volume 2019 (2019)

Editorial

Cutting Edge Technologies by Silicon- and Silicon Oxide-Based Nanostructures

Francesca A. Scaramuzzo ¹, Arántzazu González-Campo ² and Alessandro Dell'Era¹

¹Department of Fundamental and Applied Sciences for Engineering, Sapienza University, Rome, Italy

²Institut de Ciència de Materials de Barcelona (ICMAB-CSIC), Barcelona, Spain

Correspondence should be addressed to Francesca A. Scaramuzzo; francesca.scaramuzzo@uniroma1.it

Received 31 October 2020; Accepted 31 October 2020; Published 10 February 2021

Copyright © 2021 Francesca A. Scaramuzzo et al. This is an open access article distributed under the Creative Commons Attribution License, which permits unrestricted use, distribution, and reproduction in any medium, provided the original work is properly cited.

Due to its semiconductive properties, silicon has been widely used and still represents the basis of electronics-related technologies. Despite having properties often very different from the pure element, silicon derivatives (e.g., SiO₂, SiC, and silanes) are widely exploited as well in a variety of fields, ranging from photonic to biomedicine. Besides the traditional applications, the wide spreading of nanostructures, with their enhanced and in some respect unexpected properties, is now opening new perspectives for the possible uses of silicon and its derivatives. In this thematic special issue, our purpose was to highlight cutting-edge technologies and most modern applications related to these materials, especially at the nanoscale. We are glad to announce that the five original research papers published here, which we will briefly present in the following, all perfectly fit with our starting aim.

Two of the papers focus on issues related to the crucial role of Si and its derivatives for nanoelectronic and nanophotonic applications, clarifying the synthetic aspects which can substantially improve the features of the final obtainable structures. In particular, R.B. Beck and K. Ber synthesized ultrathin silicon layers by the mean of plasma-enhanced chemical vapor deposition (PECVD), analysing the influence of each parameter (i.e., type of reactor, presence of specific gases, timeframe, and temperature) on the final product quality. The authors elucidated some of the effects and interactions between the studied process conditions, thus providing useful indications to achieve layers with the desired properties, especially in terms of crystallinity.

H.-K. Shin and coworkers focused on the electrical and microstructural properties of Ni/C-faced 4H-n-SiC sub-

strates, analysing the crucial effect of temperature on ohmic contacts. Briefly, the authors were able to demonstrate that by optimizing the thermal annealing it is possible to obtain a vertically oriented NiSi phase allowing the formation of ohmic contacts; on the other hand, the horizontal-type NiSi phase obtainable at higher temperatures results in the degradation of ohmic behaviour.

Besides the electronic field, silicon and its derivatives are now recognized as useful intermediates for surface functionalization, nanostructure synthesis, and decoration. Within this context, Y. Wang and coworkers contributed to this special issue with two papers. The authors devoted their efforts to the development of rapid, efficient, and high-yield ways to obtain a new silane coupling agent, which was then fully characterized, also in terms of thermal stability. Being able to react at the same time with metal oxides and organic compounds, the synthesized thiohydrazide-iminopropyltriethoxysilane played a key role in the design and preparation of a drug carrier based on magnetic nanoparticles. As a proof of principle, the system was tested for loading doxorubicin and revealed excellent pH responsiveness for drug releasing.

Finally, within the field of Si for energy production and storage, P.P. Prosini and coworkers developed an efficient synthetic strategy for Si nanowires to be used as anodes in lithium-ion batteries. By growing Si nanostructures directly on the current collector, the authors were able at the same time (i) to overcome the problem of the volumetric expansion occurring in the anode during lithium alloying and (ii) to guarantee an excellent electric contact without adding conducting binders to the electrode. Despite the linear

capacity fade observed upon cycling, at different values of the charging current, the synthesized nanowires showed an exceptionally high-rate capability.

Due to the importance of the topic and the relevance of the achieved results, we sincerely hope that the papers published in this special issue would be of high interest for all readers of the journal.

Conflicts of Interest

The Lead Guest Editor and the Guest Editors declare that there is no conflict of interest.


Acknowledgments

We thank all authors for their valuable work and the referees for their efforts in carefully reviewing the manuscripts.

*Francesca A. Scaramuzzo
Arántzazu González-Campo
Alessandro Dell'Era*

Research Article

Electrochemical Characterization of Cu-Catalysed Si Nanowires as an Anode for Lithium-Ion Cells

P. P. Prosini,¹ F. Rondino ,² M. Moreno,¹ C. Cento,¹ M. Ottaviani,^{1,3} A. Rufoloni,² L. Pilloni,⁴ V. Orsetti,² and A. Santoni²

¹Energy Technologies Department, ENEA C.R. Casaccia, Rome, Italy

²Fusion and Technologies for Nuclear Safety and Security Department, ENEA C.R. Frascati, Italy

³SBAI Department “La Sapienza” University of Rome, Via del Castro Laurenziano 7, Rome, Italy

⁴Territorial and Production Systems Sustainability Department, ENEA C.R. Casaccia, Rome, Italy

Correspondence should be addressed to F. Rondino; flaminia.rondino@enea.it

Received 11 April 2020; Revised 24 June 2020; Accepted 6 July 2020; Published 22 July 2020

Guest Editor: Arántzazu González-Campo

Copyright © 2020 P. P. Prosini et al. This is an open access article distributed under the Creative Commons Attribution License, which permits unrestricted use, distribution, and reproduction in any medium, provided the original work is properly cited.

Silicon (Si) nanowires (NWs) grown on stainless-steel substrates by Cu-catalysed Chemical Vapour Deposition (CVD) have been prepared to be used as anodes in lithium-ion batteries. The use of NWs can overcome the problems related to the Si volume changes occurring during lithium alloying by reducing stress relaxation and preventing material fragmentation. Moreover, since the SiNWs are grown directly on the substrate, which also acts as a current collector, an excellent electrical contact is generated between the two materials without the necessity to use additional binders or conducting additives. The electrochemical performance of the SiNWs was tested in cells using lithium metal as the anode. A large irreversible capacity was observed during the first cycle and, to a lesser extent, during the second cycle. All the subsequent cycles showed good reversibility even if the coulombic efficiency did not exceed 95%, suggesting the formation of an unstable SEI film and a continuous decomposition of the electrolyte on the silicon surface. The absence of a stable SEI film was assumed responsible for a linear capacity fade observed upon cycling. On the other hand, the electrochemical characterization performed at different values of the charging current showed that SiNWs possess an exceptionally high rate capability.

1. Introduction

Rechargeable lithium-ion batteries (LIBs) are considered as one of the most versatile storage systems to power consumer electric devices, electric vehicles, and stationary energy storage systems due to their high energy density, long cycle life, and high-power performance [1, 2]. However, the development of new and sustainable electrode materials that can increase the energy density of LIB is still an open challenge. State-of-the-art electrode materials for LIBs exhibit a good capacity retention over many cycles but are characterized by a relatively low specific capacity (370 mAh g⁻¹ and 180 mAh g⁻¹ for the anode and cathode, respectively), due to the limited number of intercalation sites for Li ions. In recent years, silicon is emerging as a promising candidate to replace the conventional LIB anode based on graphite,

because it offers an impressive specific capacity (up to 3600 mAh g⁻¹) and a low delithiation potential (below 0.5 V against Li/Li⁺) [3, 4]. However, its practical application has some drawbacks such as the poor capacity retention related to the electrode pulverization promoted by the huge volume expansion (up to 400%) occurring during the charge/discharge cycles [5].

To overcome these disadvantages, great effort has been aimed at the investigation of alternative silicon structures. In this context, silicon nanoparticles [6, 7], silicon nanowires/nanotubes [8–10], nanosheets [11–13], nanofilms [14], and 3D porous structures [15, 16] have been intensely studied to improve the anode performance significantly. At the same time, extensive research has been carried out to combine the silicon nanostructures with different carbon materials [17, 18] such as amorphous carbon [19], conductive

carbon black [20], carbon nanotubes [21], and graphene [22, 23]. The insertion of metal nanoparticles has been also explored in terms of surface modification of the Si nanostructure to improve overall performance, particularly coulombic efficiency and power capability [24, 25]. Furthermore, polymeric coating has been widely investigated due to the evident improvement of the electrical conductivity of the Si-based anode and to the better capability of accepting the volume change during the charge-discharge processes [26, 27]. As a result, this kind of anode exhibits an excellent long-term cycling ability with capacity retention of 83.4% over 350 cycles at 0.5 C [28].

Among 1D nanostructures, SiNWs have attracted much attention due to the large specific surface area, short diffusion path, and reduced internal stress and, especially, because they have a high cracking strength that can improve their electrochemical performance in terms of capacity retention [29]. In addition, they can be grown directly on the current collector eliminating the need for binders or conductive materials. Despite these promising properties, SiNWs still suffer from capacity degradation when the number of charge-discharge cycles increases. In addition, SiNW-based anodes show a low first cycle coulombic efficiency (about 70%), which has been attributed to the decomposition of the electrolyte with the destruction and continuous growth of the SEI layer [30, 31]. Efficiency increases in subsequent cycles, but the capacity recovered in the charge is always less than that used during the discharge process. This aspect can be related to the enormous increase in volume that silicon undergoes during the lithiation process. Indeed, many studies have demonstrated that the large volume change occurring during lithium insertion induces cracking in the SEI that continuously produces a Si fresh surface leading to Li consumption and adding new material able to disrupt the previous SEI layer [32]. Currently, the insertion of various materials into SiNW-based anodes through metal or metal oxide doping has clearly shown to be an efficient strategy for the improvement of the electrochemical performances leading to long-term cycling and an excellent rate performance [33]. Recently, Sadeghipari et al. [34] have demonstrated that the Al_2O_3 -encapsulated SiNWs can exhibit a high reversible discharge capacity of about 3000 mAh g^{-1} at a rate of C/16, and at a higher rate density, this electrode can deliver a high capacity of 965 mAh g^{-1} with an excellent capacity retention of 94% over 120 cycles.

On the other hand, a uniform and complete carbon coating of SiNWs was also found to prevent the nanowire expansion needed to exhibit capacities of 2000 mAh g^{-1} over 300 cycles [35, 36].

Unfortunately, despite the evident progress, several drawbacks still limit the SiNW use in LIBs such as low specific energy density, low mass loading, and high processing cost.

Based on these considerations, in this paper, we have investigated the electrochemical properties of Cu-catalysed SiNWs grown directly on a stainless-steel substrate by the Vapour-Liquid-Solid (VLS) mechanism in a Chemical Vapour Deposition (CVD) reactor. The CVD method is widely used to grow SiNWs mainly with Au metal as the catalyst. However, its practical application is limited because of

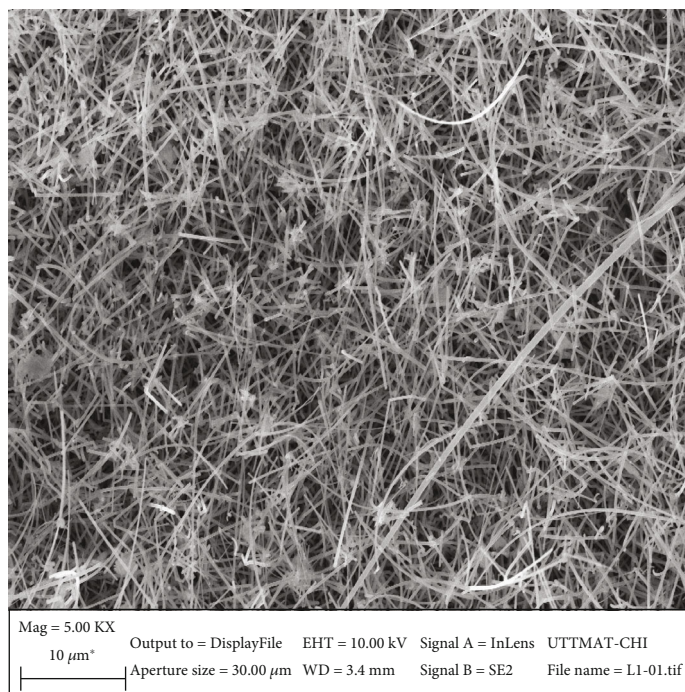
its high cost and its involvement in parasitic reactions causing the decomposition of the electrolyte or of the solvent on the SiNW surface leading to the formation of an unstable SEI layer [9, 37, 38]. Among the alternative catalyst materials, the use of the less expensive, Si-compatible Cu catalyst could be advantageous for growing SiNWs for LIB applications. Another advance to improve the ability of SiNWs to be used as anodes is the possibility to synthesize crystalline-amorphous core-shell nanowires. The electrochemical activity of the amorphous Si shells can be limited by selecting the lithiation potential. In these conditions, the crystalline core acts as a mechanical support and electrical conductor while the amorphous part stores the Li ions. Indeed, the crystalline-amorphous structure plays a fundamental role in the SiNW technology allowing to obtain high charge storage capacities (1000 mA/g) with 90% capacity retention over 100 cycles [39]. In this work, we report about the CVD synthesis on stainless steel of Cu-catalysed SiNWs with a well-defined morphology and core-shell structure. To evaluate their Li storage properties, the SiNWs were used as electrodes in an electrochemical cell against lithium metal, without using any binder or additive. The electrodes showed a large capacity and maintained a good reversibility for the first ten cycles. On the other hand, long-term cycling was considered unsuitable for practical applications.

2. Experimental

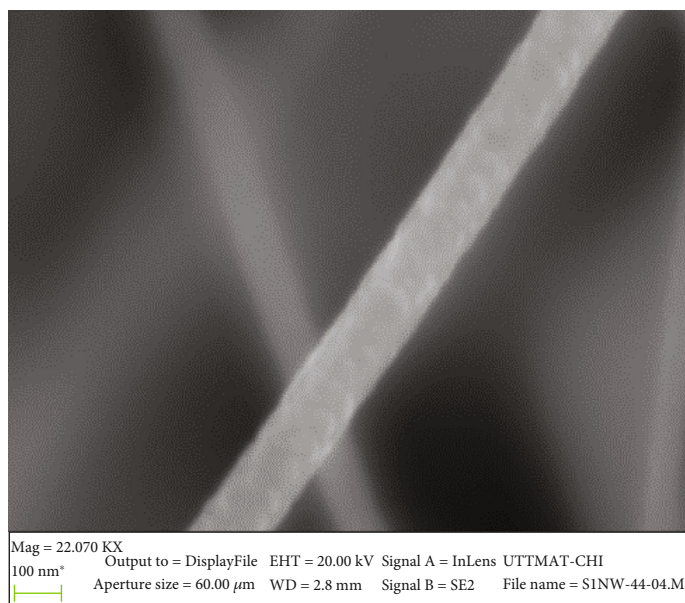
2.1. Synthesis of SiNWs. Among the various methods used to synthesize SiNWs [24], the most popular is surely CVD based on the VLS mechanism [40, 41]. According to this process, we have grown SiNWs directly on 304 stainless-steel substrates ($10 \times 10 \text{ mm}^2$, $30 \mu\text{m}$ thick) without using binders or additives. Before the insertion of the substrates into the CVD furnace (Lenton, UK), they were decorated with the Cu catalyst using a commercial suspension (PlasmaChem) that provides a known density ($6 \mu\text{g/ml}$) and a known diameter (40 nm) of the primary copper nanoparticles. In order to obtain a uniform metallic nanoparticle distribution and prevent agglomeration, a modified commercial pneumatic nebulizer for medical use (Chiesi, Clenny A Aerosol) was used. After the functionalization, the decorated substrates were inserted into a 1-inch diameter quartz tube using a ceramic container and placed into the oven.

In order to obtain suitable SiNW electrodes for LIBs, an accurate choice of the growing parameters was performed. In particular, the influence of the temperature on the SiNW growth was investigated. In fact, although the eutectic temperature of the Cu/Si alloy required for the SiNW growth by the VLS mechanism is 802°C , the synthesis of SiNWs can also occur at lower temperatures and may be ascribed to a VSS (Vapour-Solid-Solid) process [42–44]. Based on this consideration, pure silane gas (used as the Si precursor) was introduced at a pressure of around 2 Torr with a flux of 6 sccm for 12 minutes. In order to investigate the role of the temperature on the growth, the temperature was varied from the 500°C up to 800°C .

The quantity of SiNWs obtained was accurately determined by measuring the mass of the sample using a



(a)



(b)

FIGURE 1: (a) Low- and (b) high-magnification SEM images of SiNWs.

microbalance (Radwag 60/220/X) before and after the growth. The mass loading of the prepared SiNWs was about 1.2 mg/cm^2 , and this result is consistent with the literature for Cu-catalysed SiNWs grown on stainless steel [45].

2.2. Morphological Characterization. The morphology of the samples was evaluated by Scanning Electron Microscopy (SEM, HR-FEGSEM LEO 1525) and Transmission Electron Microscopy (TEM, JEOL JEM2010). When the growth temperature was set to values above 700°C , the SEM images

clearly showed the absence of SiNW and the presence of a layer of silicon covering the entire surface of the stainless steel. In fact, at these temperatures, a segregation process that occurs on the stainless-steel surface and is able to modify the roughness and surface composition hinders the VLS mechanism preventing the growth of SiNW. To avoid the segregation and favour the SiNW growth, the temperature must be lowered to about 600°C . As a result, a remarkable growth of SiNWs uniformly distributed on the steel substrate is obtained. SEM images in Figure 1 show the morphology of

the so-obtained SiNWs. SiNWs have a length of several microns (Figure 1(a)) and a diameter of about 300 nm (Figure 1(b)).

In order to evaluate the SiNW structure, TEM analysis was performed. The TEM image and the diffraction pattern of Figure 2 show a core-shell crystalline-amorphous structure with the presence of a crystalline silicon (c-Si) core having the same dimension of the copper nanoparticles used as a catalyst (40 nm) and an amorphous silicon (a-Si) shell, formed by the pyrolytic decomposition of silane on the crystalline core. The thickness of the a-Si directly depends on the growth time and the length of the SiNWs. This double morphological character of the SiNWs is crucial for the electrochemical performance of the cell. In principle, it should be possible to use only the a-Si for Li^+ ion storage employing the c-Si as an efficient electrical conducting pathway and stable mechanical support [39]. In this way, it is possible to improve the performance of the SiNW film when used as an electrode in LIBs.

2.3. Electrochemical Characterization. The SiNWs deposited on the stainless-steel substrate were directly used for the electrochemical characterization. The samples were inserted in a two-electrode cell formed by a polypropylene T-type pipe connector closed at the ends with two cylindrical stainless steel (SS316) acting as current collectors. A glass fiber (Whatman 1820-240, grade GF/A) was used as the separator. The cell was filled with ethylene carbonate/dimethyl carbonate 1:1 LiPF_6 1 M electrolyte solution (LP30, Merck, battery grade). The cycling tests were carried out automatically by means of a battery cycler (MACCOR 4000). To assess the electrochemical performance, the electrodes were galvanostatically cycled between 2.0 V and 0.005 V vs. Li/Li^+ . Cell assembly, test, and storage were performed in a dry room (R.H. < 0.1% at 20°C).

3. Results and Discussion

In order to investigate the structural transition inside the SiNWs and understand the role of SiNW morphology on the electrochemical properties, the first and second charge/discharge voltage profiles are compared with a more accurate analysis of the differential capacity dQ/dV (mAh V^{-1}) curves as shown in Figures 3(a) and 3(b) and Figures 3(c) and 3(d). The cell was cycled with a current of 0.14 mA, corresponding to the C/10 rate. During the first discharge cycle, a large plateau is observed in the region below 0.15 V (Figure 3(a), lower curve) which corresponds to the sharp peak at 140 mV identified by the letter A in the dQ/dV curve (Figure 3(c)). In this phase, two processes are taking place: the formation of the SEI film on the surface of Si-NWs and the formation of the lithium/silicon alloy. The latter occurs in a two-phase region in which crystalline silicon is lithiated and a partial amorphous lithiated silicon is formed [9, 46, 47].

After this process has completed, a second process starts at a lower voltage, and it can be identified in the dQ/dV curve as the sharp peak centred at around 50 mV and identified in Figure 3(c) by the letter B. This process continues until the cut-off potential set at 0.05 V vs Li^+/Li is reached. This peak

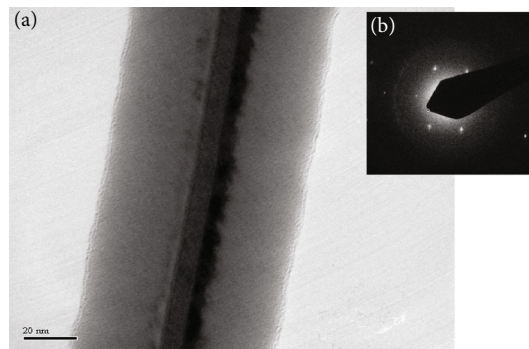


FIGURE 2: TEM image of Cu-catalysed SiNWs (a) and diffraction pattern (b).

can be attributed to a further lithiation step which transforms the amorphous lithiated silicon in a new crystalline $\text{Li}_{15}\text{Si}_4$ phase. At the end of the process, the capacity used for SEI film formation and Si lithiation amounts to about 2500 mAh/g. In the following charge curve (Figure 3(a), upper curve), it is evident that only part of the capacity (1800 mAh/g) is reversibly extracted from the electrode. The corresponding dQ/dV curve (Figure 3(c)) shows two broad peaks at 360 mV and 460 mV (identified by the letters C and D, respectively) which can be attributed to the extraction of lithium from two different delithiation degrees of amorphous lithiated silicon to form amorphous silicon.

During the second discharge cycle, an additional sloping region at about 0.3-0.2 V appears in the discharge curve (Figure 3(b), lower curve). This plateau corresponds to the peak located at 230 mV (A) in the dQ/dV curve (Figure 3(d)) which is assigned to the lithiation process of the amorphous silicon coming from the dealloying reaction. As a result, the discharge capacity is reduced down to about 1900 mAh/g. Similarly, to the first discharge curve, the second lithiation cycle also shows a sharp peak (B in Figure 3(d)) at a voltage below 50 mV attributed to a further lithiation able to transform the amorphous lithiated silicon in crystalline $\text{Li}_{15}\text{Si}_4$. The voltage profile in the second charge cycle appears similar to the profile exhibited during the first cycle with the capacity maintaining a stable value of about 1800 mAh/g (Figure 3(b), upper curve). This investigation has permitted to better understand the role of the crystalline-amorphous core-shell structure of the SiNWs on the charge and discharge processes. In particular, as described above, while the reversible process can be attributed to the lithiation of crystalline Si, the high irreversible capacity (70%) found in the first cycle can be ascribed to the formation of a SEI passivation layer on the silicon nanowire surface, induced by the reduction of the electrolyte [48, 49]. Some authors showed that a carbon coating or a conductive polymer used as a binder can drastically reduce this irreversible loss [36, 37].

In Figure 4, the discharge/charge capacity versus cycle number for the SiNW electrode together with the charge efficiency (CE) is shown. The CE is defined as the ratio between the capacity inserted into the electrode in charge and the capacity released in the previous discharge cycle ($Q_{\text{ch}}/Q_{\text{dis}}$).

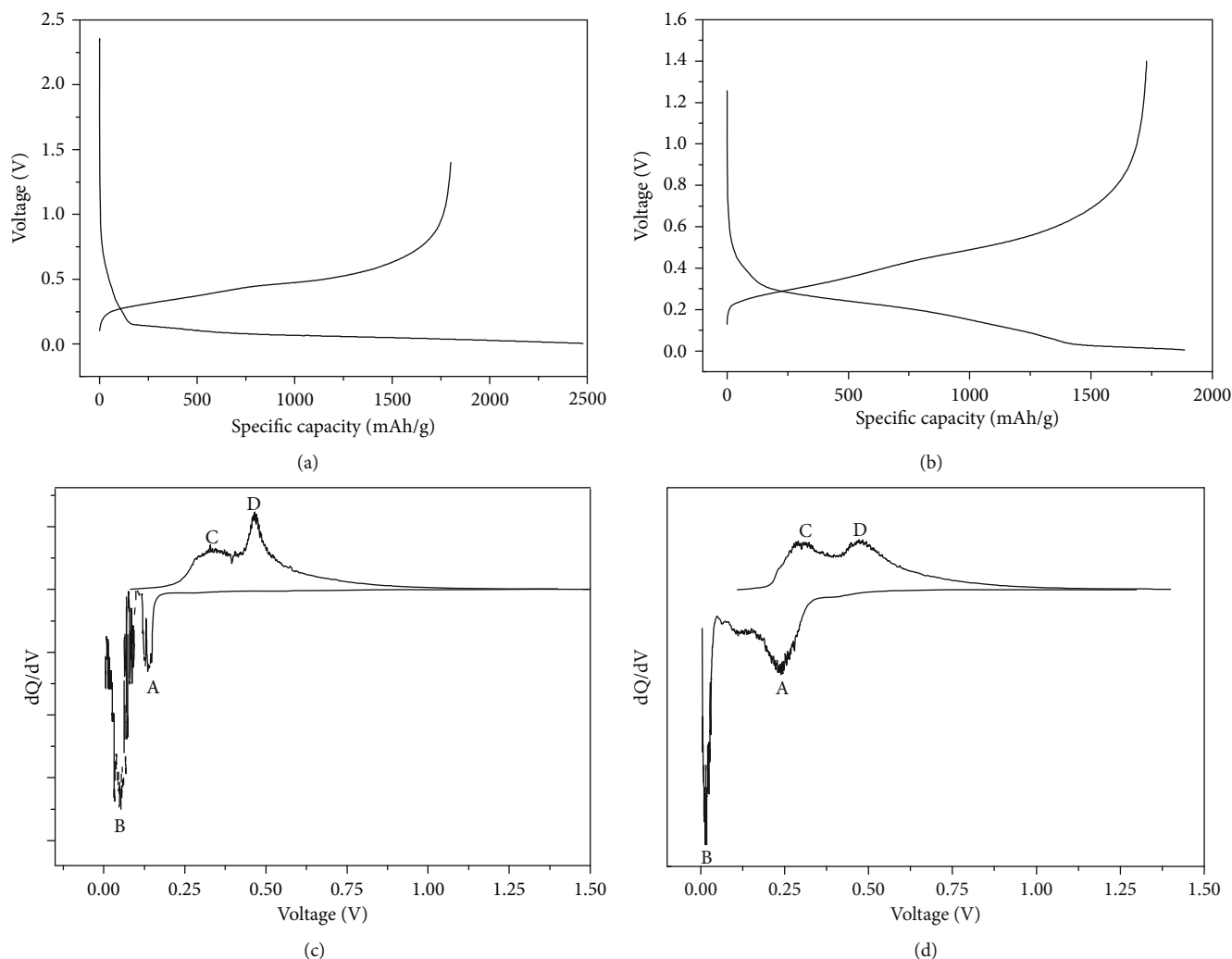


FIGURE 3: Voltage profiles as a function of capacity for the SiNWs cycled in a lithium cell at C/10 rate during the first (a) and the second (b) cycle and differential dQ/dV vs. V curves corresponding to the first (c) and the second (d) cycle.

The first test was conducted at a very low charge-discharge current (C/10 rate) and included a limited number of cycles (14 cycles). However, the limited number of cycles was enough to evaluate the goodness of the SiNWs when used as anodes in LIBs. In fact, SiNWs with inappropriate morphologies exhibit poor cycling just after few cycles due to the degradation of the Si structure occurring during the lithiation and delithiation processes [8, 14, 37]. In our case, all cycles show a discharge capacity (circles) larger than the charge capacity (squares). After the first cycle, the CE increases up to 95%, and this value was kept constant in the subsequent cycles, suggesting that no drastic change of the core-shell SiNW structure occurs and that the SiNWs remain well connected with the stainless-steel current collector. To evaluate the rate capability of the SiNWs, the cell was cycled at various charge rates. The discharge was always carried out galvanostatically at 0.2 mA (C/10 rate), and Figure 5 shows the correspondent voltage profiles. At the lowest charge current value (C/10 rate), the cell exhibits a specific capacity approaching 2000 mAh/g. Slightly lower values were observed when the charging current was increased from

C/10 to the 1C rate. When the current is increased to 2C, the capacity drops down to 1600 mAh/g. Another notable decrease in capacity is observed when charging the cell at 3C and 5C. At the 5C rate, the specific capacity goes down to 1200 mAh/g. From this result, it is possible to state that the SiNWs show good capacity retention with increasing charging rates, being able to provide 60% of the capacity exhibited at low current when discharged with a current 50 times higher. Therefore, our SiNW electrodes show good areal capacities also at fast charge/discharge rates (e.g., from 2.4 mAh cm^{-2} at 1C to 1.4 mAh cm^{-2} at 5C) although they have low material loading of 1.2 mg cm^{-2} .

Quantifying the rate performance of the SiNWs is possible by the use of a parameter as proposed by Prosini [50] and Fongy et al. [51]. They suggested the use of a parameter k (in hours) to characterize the system response in power. The k parameter is defined by $Q = Q_0 + kI_m$, where Q is the charge capacity at the charge current I_m and Q_0 is the (pseudo) equilibrium charge capacity (mAh), i.e., the capacity evaluated at the lower charge rate. The higher is the k parameter, the worse is the electrode performance in terms of power.

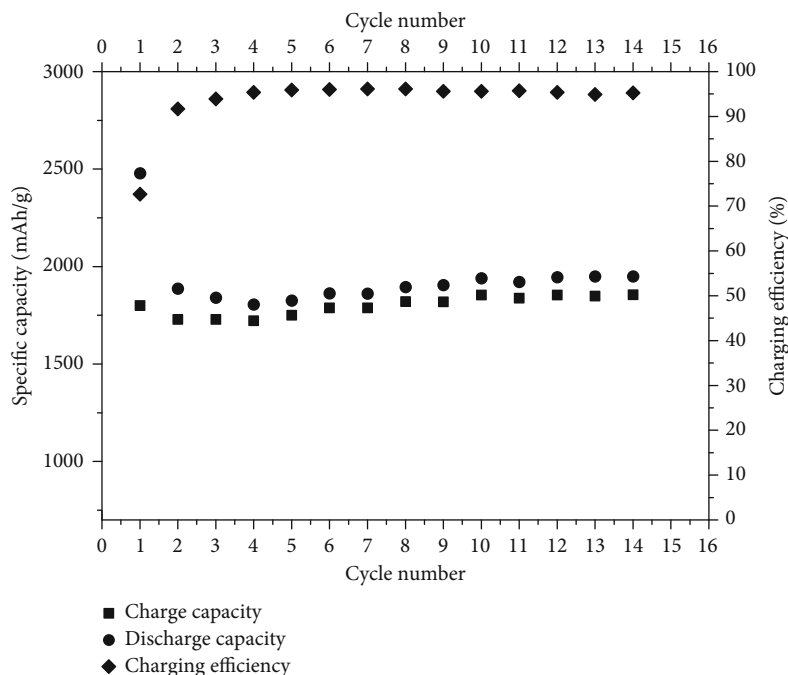


FIGURE 4: Capacity in charge and discharge and charging efficiency during the first cycles conducted at the C/10 rate.

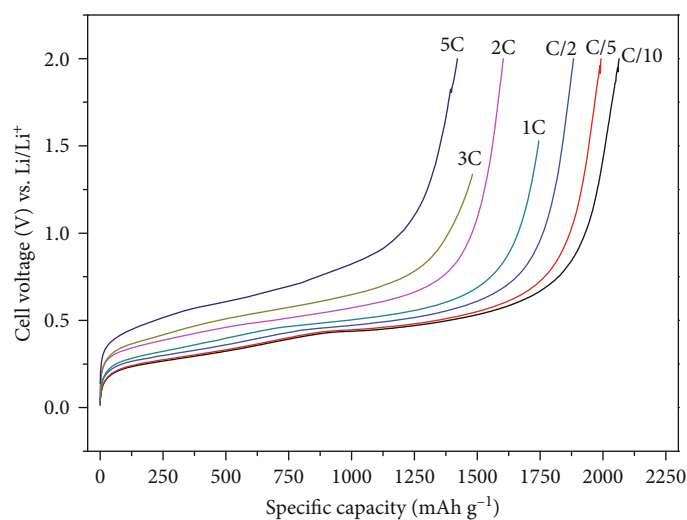


FIGURE 5: Charge capacity during seven cycles conducted at various charge rates. The C-rate values are reported in the figure.

Figure 6 shows the dependence of the capacity as a function of the charge current for the SiNW electrode. In our case, a linear behaviour is observed, and it is possible to evaluate the k value. From the slope of the regression line, the k value was calculated to be -0.095 h. This value is very low especially when compared to other active materials used in lithium-ion technology confirming the high rate capability of Cu-catalysed SiNWs [50, 51].

The cycling of the electrode at various charge rates was prolonged to evaluate the stability of the SiNWs as a function of the cycle number, and Figure 7 reports the values of the capacity at various C rates vs. cycle numbers. Contrary to what was observed during the cycles conducted at the C/10 rate, a severe capacity fading was observed for all the dis-

charge currents. To explain this behaviour, we hypothesized that at higher rates, the current distribution is uneven, and part of the silicon nanowire grows faster than the other parts. The greater expansion of these parts causes the breakdown of the SEI film and the detachment of silicon microparticles from the nanowires. These parts become electrochemically inactive, hindering the complete lithiation of silicon nanowires in subsequent cycles. Bloom et al. [52] demonstrated that the degradation of the power capability during cycling of a Li-ion cell can be related to the increase of the cell internal resistance which can also be related to the properties of the SEI. Therefore, when nanostructured silicon electrodes are cycled at very high current rates, fresh surface areas are produced by the silicon expansion during the lithiation, as

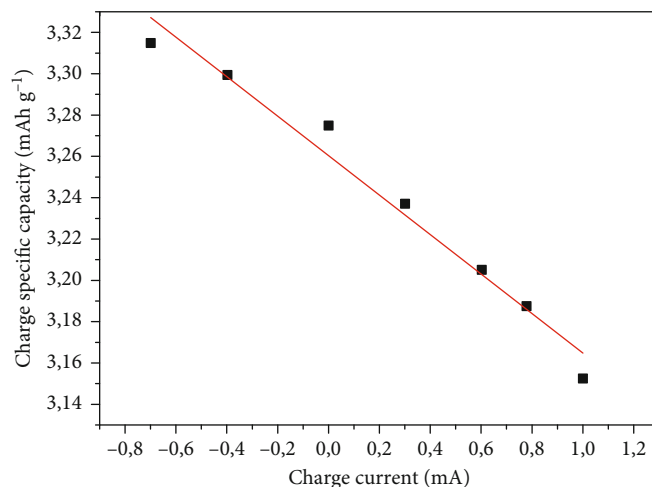


FIGURE 6: Effective capacity in charge as a function of the charge current.

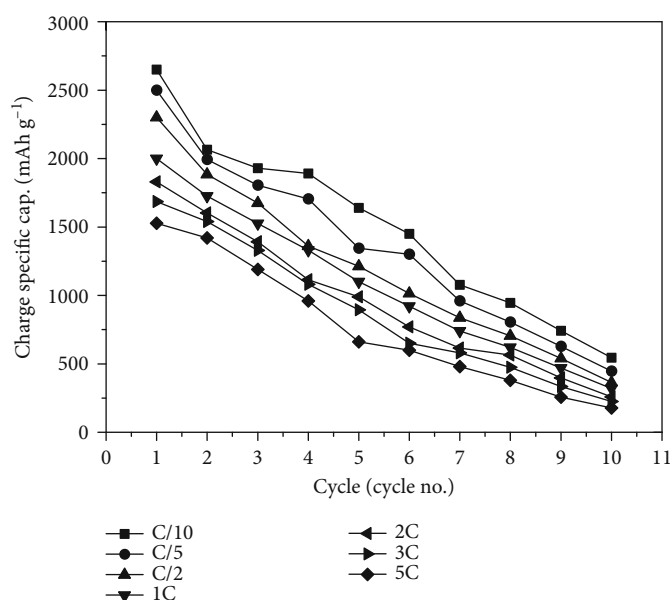


FIGURE 7: Capacity during charge as a function of the cycle number for the SiNW electrode cycled at various charge rates.

well described by the extension of Pinson's model shown in ref. [53]. According to this model, the linear capacity fade observed during the lithiation/delithiation processes of the cell can be attributed to the SEI formation on freshly exposed surfaces [31, 32]. This result confirms the crucial role of the SEI formation on the capacity fading and cycle life of the cell.

4. Conclusions

In conclusion, SiNWs were grown directly on a stainless-steel substrate by Cu nanoparticle-catalysed CVD. SEM images show that the so-obtained SiNWs have a length of several microns and diameter ranging from 200 nm to 500 nm. TEM images confirm the core-shell structure of the SiNWs with the presence of a crystalline silicon core of around 40 nm (the same dimension of the copper nanoparticles) and an amorphous silicon shell.

The electrochemical properties of the silicon electrode have been investigated using lithium foil as the counter and reference electrode. The high irreversible capacity observed mainly in the first cycle was attributed to the formation of the SEI layer on the silicon surface, while the other cycles have shown good capacity retention with a high charge efficiency above 90%. This result confirms the good electrical contact existing between the SiNWs and the stainless-steel current collector. When compared with other active materials used in lithium-ion technology, the SiNWs exhibited a high rate capability, being able to provide 60% of the capacity exhibited at the C/10 rate when discharged with a 50 times higher current. The SiNW electrodes showed rapid capacity fade during the lithiation/delithiation processes probably attributed to the SEI formation on freshly exposed surfaces. Further investigations on the mechanism of the SEI growth can help to limit this fading, improving

the performance of the cell in terms of capacity retention and long cycle life.

Data Availability

All data used in this article are available from the corresponding author upon request.

Conflicts of Interest

The authors declare that they have no conflicts of interest.

Acknowledgments

Part of this work was carried out within the framework “Ricerca di Sistema Elettrico” funded by the Italian Ministry of Economic Development.

References

- [1] B. Scrosati and J. Garche, “Lithium batteries: status, prospects and future,” *Journal of Power Sources*, vol. 195, no. 9, pp. 2419–2430, 2010.
- [2] D. Linden and T. Reddy, *Handbook of Batteries*, Mc Graw-Hill, New York, 2002.
- [3] C. J. Wen and R. A. Huggins, “Chemical diffusion in intermediate phases in the lithium-silicon system,” *Journal of Solid State Chemistry*, vol. 37, no. 3, pp. 271–278, 1981.
- [4] J. R. Szczech and S. Jin, “Nanostructured silicon for high capacity lithium battery anodes,” *Energy & Environmental Science*, vol. 4, no. 1, pp. 56–72, 2011.
- [5] H. Wu and Y. Cui, “Designing nanostructured Si anodes for high energy lithium ion batteries,” *Nano Day*, vol. 7, no. 5, pp. 414–429, 2012.
- [6] M. Raić, L. Mikac, I. Marić et al., “Nanostructured silicon as potential anode material for Li-ion batteries,” *Molecules*, vol. 25, no. 4, pp. 891–908, 2020.
- [7] S. Y. Lai, K. D. Knudsen, B. T. Sejersted, A. Ulvestad, J. P. Mæhlen, and A. Y. Kopysov, “Silicon nanoparticle ensembles for lithium-ion batteries elucidated by small-angle neutron scattering,” *ACS Applied Energy Materials*, vol. 2, no. 5, pp. 3220–3227, 2019.
- [8] C. K. Chan, H. Peng, G. Liu et al., “High-performance lithium battery anodes using silicon nanowires,” *Nature Nanotechnology*, vol. 3, no. 1, pp. 31–35, 2008.
- [9] Y. Yang, W. Yuan, W. Kang et al., “A review on silicon nanowire-based anodes for next-generation high-performance lithium-ion batteries from a material-based perspective,” *Sustainable Energy & Fuels*, vol. 4, no. 4, pp. 1577–1594, 2020.
- [10] M. H. Park, M. G. Kim, J. Joo et al., “Silicon nanotube battery anodes,” *Nano Letters*, vol. 9, no. 11, pp. 3844–3847, 2009.
- [11] J. Tang, Q. Yin, Q. Wang et al., “Two-dimensional porous silicon nanosheets as anode materials for high performance lithium-ion batteries,” *Nanoscale*, vol. 11, no. 22, pp. 10984–10991, 2019.
- [12] H. Wang, W. Tang, L. Ni et al., “Synthesis of silicon nanosheets from kaolinite as a high-performance anode material for lithium-ion batteries,” *Journal of Physics and Chemistry of Solids*, vol. 137, p. 109227, 2020.
- [13] S.-W. Park, J. H. Ha, J. M. Park, B. W. Cho, and H.-J. Choi, “2D silicon nanosheets/carbon composites based foldable anode electrode for lithium-ion batteries,” *Journal of The Electrochemical Society*, vol. 167, no. 2, article 020556, 2020.
- [14] N. Bensalah, F. Z. Kamand, M. Zaghrou, H. D. Dawoud, and T. Al Tahtamouni, “Silicon nanofilms as anode materials for flexible lithium ion batteries,” *Thin Solid Films*, vol. 690, p. 137516, 2019.
- [15] T. Ikonen, T. Nissinen, E. Pohjalainen, O. Sorsa, T. Kallio, and V.-P. Lehto, “Electrochemically anodized porous silicon: towards simple and affordable anode material for Li-ion batteries,” *Nature*, vol. 7, no. 1, article 7880, 2017.
- [16] W. Wang, Z. Favors, R. Ionescu et al., “Monodisperse Porous Silicon Spheres as Anode Materials for Lithium Ion Batteries,” *Nature*, vol. 5, no. 1, p. 8781, 2015.
- [17] H. F. Andersen, C. E. L. Foss, J. Voje et al., “Silicon-carbon composite anodes from industrial battery grade silicon,” *Scientific Reports*, vol. 9, no. 1, article 14814, 2019.
- [18] S. Chae, S. H. Choi, N. Kim, J. Sung, and J. Cho, “Integration of graphite and silicon anodes for the commercialization of high-energy lithium-ion batteries,” *Angewandte Chemie, International Edition*, vol. 59, no. 1, pp. 110–135, 2020.
- [19] G. Fang, X. Deng, J. Zou, and X. Zeng, “Amorphous/ordered dual carbon coated silicon nanoparticles as anode to enhance cycle performance in lithium ion batteries,” *Electrochimica Acta*, vol. 295, pp. 498–506, 2019.
- [20] M. Phadatar, R. Patil, N. Blomquist et al., “Silicon-nanographite aerogel-based anodes for high performance lithium ion batteries,” *Scientific Reports*, vol. 9, no. 1, article 14621, 2019.
- [21] W. Wang, R. Epur, and P. N. Kumta, “Vertically aligned silicon/carbon nanotube (VASCNT) arrays: hierarchical anodes for lithium-ion battery,” *Electrochemistry Communications*, vol. 13, no. 5, pp. 429–432, 2011.
- [22] Y. Li, K. Yan, H.-W. Lee, Z. Lu, N. Liu, and Y. Cui, “Growth of conformal graphene cages on micrometre-sized silicon particles as stable battery anodes,” *Nature Energy*, vol. 1, no. 2, article 15029, 2016.
- [23] M. S. Wang, Z. Q. Wang, R. Jia et al., “Facile electrostatic self-assembly of silicon/reduced graphene oxide porous composite by silica assist as high performance anode for Li-ion battery,” *Applied Surface Science*, vol. 456, pp. 379–389, 2018.
- [24] S. Yoo, J.-I. Lee, S. Ko, and S. Park, “Highly dispersive and electrically conductive silver-coated Si anodes synthesized via a simple chemical reduction process,” *Nano Energy*, vol. 2, no. 6, pp. 1271–1278, 2013.
- [25] Z. Chen and Z. Xie, “First-principles investigation on cluster-assembled silicon nanotubes with Eu atoms encapsulation,” *Journal of Molecular Modeling*, vol. 25, no. 8, p. 226, 2019.
- [26] M. Feng, J. Tian, H. Xie, Y. Kang, and Z. Shan, “Nano-silicon/polyaniline composites with an enhanced reversible capacity as anode materials for lithium ion batteries,” *Journal of Solid State Electrochemistry*, vol. 19, p. 2015, 2015.
- [27] C. Gan, C. Zhang, P. Liu et al., “Polymeric carbon encapsulated Si nanoparticles from waste Si as a battery anode with enhanced electrochemical properties,” *Electrochimica Acta*, vol. 307, pp. 107–117, 2019.
- [28] G. G. Eshetu and E. Figgemeier, “Confronting the challenges of next-generation silicon anode-based lithium-ion batteries: role of designer electrolyte additives and polymeric binders,” *ChemSusChem*, vol. 12, no. 12, pp. 2515–2539, 2019.

- [29] M. R. Zamfir, H. T. Nguyen, E. Moyan, Y. H. Lee, and D. Pribat, "Silicon nanowires for Li-based battery anodes: a review," *Journal of Materials Chemistry A*, vol. 1, no. 34, pp. 9566–9586, 2013.
- [30] A. Wang, S. Kadam, H. Li, S. Shi, and Y. Qi, "Review on modeling of the anode solid electrolyte interphase (SEI) for lithium-ion batteries," *npj Computational Materials*, vol. 4, no. 1, 2018.
- [31] A. L. Michan, G. Divitini, A. J. Pell, M. Leskes, C. Ducati, and C. P. Grey, "Solid electrolyte interphase growth and capacity loss in silicon electrodes," *Journal of the American Chemical Society*, vol. 138, no. 25, pp. 7918–7931, 2016.
- [32] E. Peled, D. B. Tow, A. Merson, A. Gladkikh, L. Burstein, and D. Golodnitsky, "Composition, depth profiles and lateral distribution of materials in the SEI built on HOPG-TOF SIMS and XPS studies," *Journal of Power Sources*, vol. 97-98, pp. 52–57, 2001.
- [33] M. F. Hainey and J. M. Redwing, "Aluminum-catalyzed silicon nanowires: growth methods, properties, and applications," *Applied Physics Reviews*, vol. 3, no. 4, article 040806, 2016.
- [34] M. Sadeghipari, A. Mashayekhi, and S. Mohajezadeh, "Novel approach for improving the performance of Si-based anodes in lithium-ion batteries," *Nanotechnology*, vol. 29, article 055403, 2018.
- [35] L. F. Cui, Y. Yang, C. M. Hsu, and Y. Cui, "Carbon-silicon core-shell nanowires as high capacity electrode for lithium ion batteries," *Nano Letters*, vol. 9, no. 9, pp. 3370–3374, 2009.
- [36] T. D. Bogart, D. Oka, X. Lu, M. Gu, C. Wang, and B. A. Korgel, "Lithium ion battery Performance of silicon nanowires with carbon skin," *ACS Nano*, vol. 8, no. 1, pp. 915–922, 2013.
- [37] A. M. Chockla, T. D. Bogart, C. M. Hessel, K. C. Klavetter, C. B. Mullins, and B. A. Korgel, "Influences of gold, binder and electrolyte on silicon nanowire performance in Li-ion batteries," *The Journal of Physical Chemistry C*, vol. 116, no. 34, pp. 18079–18086, 2012.
- [38] P. P. Prosini, C. Cento, A. Rufoloni, F. Rondino, and A. Santoni, "A lithium-ion battery based on LiFePO_4 and silicon nanowires," *Solid State Ionics*, vol. 269, pp. 93–97, 2015.
- [39] L.-F. Cui, R. Ruffo, C. K. Chan, H. Peng, and Y. Cui, "Crystal-line-amorphous core-shell silicon nanowires for high capacity and high current battery electrodes," *Nano Letters*, vol. 9, no. 1, pp. 491–495, 2009.
- [40] R. S. Wagner and W. C. Ellis, "Vapor-liquid-solid mechanism of single crystal growth," *Applied Physics Letters*, vol. 4, no. 5, pp. 89–90, 1964.
- [41] E. I. Givargizov, "Fundamental aspects of VLS growth," *Journal of Crystal Growth*, vol. 31, pp. 20–30, 1975.
- [42] Y. Yao and S. Fan, "Si nanowires synthesized with Cu catalyst," *Materials Letters*, vol. 61, no. 1, pp. 177–181, 2007.
- [43] J. Arbiol, B. Kalache, P. R. i. Cabarrocas, J. R. Morante, and A. F. i. Morral, "Influence of Cu as a catalyst on the properties of silicon nanowires synthesized by the vapour-solid-solid mechanism," *Nanotechnology*, vol. 18, no. 30, article 305606, 2007.
- [44] J. L. Lensch-Falk, E. R. Hemesath, D. E. Perea, and L. J. Lauhon, "Alternative catalysts for VLS growth of silicon and germanium nanowires," *Journal of Materials Chemistry*, vol. 19, no. 7, pp. 849–857, 2009.
- [45] Y. Xiao, D. Hao, H. Chen, Z. Gong, and Y. Yang, "Economical synthesis and promotion of the electrochemical performance of silicon nanowires as anode material in Li-ion batteries," *Applied Materials & Interfaces*, vol. 5, no. 5, pp. 1681–1687, 2013.
- [46] A. L. Michan, M. Leskes, and C. P. Grey, "Voltage dependent solid electrolyte interphase formation in silicon electrodes: monitoring the formation of organic decomposition products," *Chemistry of Materials*, vol. 28, no. 1, pp. 385–398, 2016.
- [47] M. N. Obrovac and L. Christensen, "Structural changes in silicon anodes during lithium insertion/extraction," *Electrochemical and Solid-State Letters*, vol. 7, no. 5, pp. A93–A96, 2004.
- [48] J. H. Cho and S. T. Picraux, "Silicon nanowire degradation and stabilization during lithium cycling by SEI layer formation," *Nano Letters*, vol. 14, no. 6, pp. 3088–3095, 2014.
- [49] G. Lee, S. L. Schweizer, and R. B. Wehrspohn, "Microstructural characterization of Li insertion in individual silicon nanowires," *Applied Physics A: Materials Science & Processing*, vol. 117, no. 3, pp. 973–979, 2014.
- [50] P. P. Prosini, "Modeling the voltage profile for LiFePO_4 ," *Journal of the Electrochemical Society*, vol. 152, no. 10, pp. A1925–A1929, 2005.
- [51] C. Fongy, A. C. Gaillot, S. Jouanneau, D. Guyomard, and B. Lestriez, "Ionic vs electronic power limitations and analysis of the fraction of wired grains in LiFePO_4 composite electrodes," *Journal of the Electrochemical Society*, vol. 157, no. 7, pp. A885–A891, 2010.
- [52] I. Bloom, B. W. Cole, J. J. Sohn et al., "An accelerated calendar and cycle life study of Li-ion cells," *Journal of Power Sources*, vol. 101, no. 2, pp. 238–247, 2001.
- [53] M. B. Pinson and M. Z. Bazant, "Theory of SEI formation in rechargeable batteries: capacity fade, accelerated 356 aging and lifetime prediction," *Journal of the Electrochemical Society*, vol. 160, pp. A243–A250, 2012.

Research Article

Preparation of a Novel Thiol Surface Modifier and Fe₃O₄ Drug Loading Agent as well as Releasing under pH-Sensitivity

Wang Ya-zhen ^{1,2,3}, Wu Xue-ying,¹ Di Yu-tao,¹ Lan Tian-yu,^{3,4} and Zu Li-wu^{3,4}

¹College of Chemistry and Chemical Engineering, Qiqihar University, Qiqihar, 161006 Heilongjiang, China

²College of Chemistry, Chemical Engineering and Resource Utilization, Northeast Forestry University, Harbin, 150040 Heilongjiang, China

³Heilongjiang Province Key Laboratory of Polymeric Composition Material, Qiqihar University, Qiqihar, 161006 Heilongjiang, China

⁴College of Materials Science and Engineering, Qiqihar University, Qiqihar, 161006 Heilongjiang, China

Correspondence should be addressed to Wang Ya-zhen; wyz6166@qqhru.edu.cn

Received 15 January 2020; Revised 12 March 2020; Accepted 23 March 2020; Published 8 May 2020

Guest Editor: Alessandro Dell'Era

Copyright © 2020 Wang Ya-zhen et al. This is an open access article distributed under the Creative Commons Attribution License, which permits unrestricted use, distribution, and reproduction in any medium, provided the original work is properly cited.

In this paper, in order to take advantage of the combination between magnetic nano-Fe₃O₄ and surface modifier, a pH-sensitive drug delivery system that could effectively deliver doxorubicin (DOX) to tumor tissue was constructed. The novel drug delivery system named Fe₃O₄-TIPTS-g-(PEI-co-PEG) was prepared through three steps. The first step, a surface modifier with the thiol group, thiohydrazide-aminopropyltriethoxysilane surface modifier (named TIPTS), was synthesized for the first time. The second step, Fe₃O₄-TIPTS was synthesized by treating nano-Fe₃O₄ with TIPTS. The last step, Fe₃O₄-TIPTS-g-(PEI-co-PEG) was synthesized in the presence of the Fe₃O₄-TIPTS, polyethyleneimine (PEI), and polyethylene glycol (PEG) by mercapto-initiated radical polymerization. Among them, magnetic nanoparticles (MNPs) were used as magnetically responsive carriers, PEG was the surface-modifying compound, and PEI was the drug loading site which primary amine reacts with doxorubicin (DOX). Targeted nanoparticles were considerably stabilize in various physiological solutions and exhibited pH-sensitive performance in drug release. Thence, Fe₃O₄-TIPTS-g-(PEI-co-PEG) is a promising nanocarrier for targeting tumor therapy.

1. Introduction

In the last few decades, the incidence and mortality of malignancy increased year by year, and it has become the leading cause of death in humans. Chemotherapy [1] was the most commonly used clinical treatment for cancers. However, traditional anticancer drug formulations were nonspecificity [2] for tumors; especially when used in large doses, severe side effects were often caused [3]. That is why the development of efficient delivery systems with the ability to improve in vivo distribution and significant controlled sustained release behavior is required. One innovative technological approach to solve this problem is nanotechnology which focuses on the transfer of nano-sized biocompatible devices into the cells [4]. Among different types of nanomaterials, Fe₃O₄ nanoparticles is one kind of MNPs that have shown great promise as novel delivery systems and theranostics for

personalized medicine due to their shape controllability and large specific surface area. And most importantly, their unique optical, electrical, and superparamagnetic properties give potential imaging development, targeted delivery, and synergistic drug therapy, suitable for drug delivery in cells [5]. Naked Fe₃O₄ NPs are easy to aggregate and oxidize and thus were often coated by hydrophilic materials and biocompatible polymers for targeted drug delivery [6–8].

The mercaptosilane surface modifier [9] is a particular kind of organosilicon compounds. The mercaptosilane surface modifier contains both a mercapto group reactive with an organic substance and a silicon functional group reactive with an inorganic substance. In view of this special molecular structure, a mercaptosilane surface modifier could be used as a “molecular bridge” [10] between organic substance and inorganic substance to prepare composite materials having excellent performances.

The surface coating [11] controls the absorption of particles by different cell types and affects biocompatibility, as well as the distribution of nanoparticles in the tissues of the organism [12–14], although many scientists use cationic bonds [15] to graft polymers onto the surface of nanoparticles as a drug carrier now. However, in the case of a pharmaceutical carrier obtained in this manner, cationic binding is extremely easily deactivated in physiological medium environment, resulting in poor stability. For this shortcoming, we use mercapto (-SH) [16] and polyethylene glycol (PEG) [17] propose for particle coating by free radical bonding, which can significantly improve the stability of nanoparticles in physiological medium environment, prolong the circulation time in the body, and improve the targeted delivery efficiency. PEG [18] in particular is considered to be a very promising material that protects the nanoparticles from the immune system, promotes a longer circulation time, and inhibits removal by the reticuloendothelial system. Although the application of polyethyleneimine (PEI) is plagued by their toxicity concerns, modification of PEI with PEG can address some of these concerns, improve the transfection efficiency, and enhance the systemic duration [19] at the same time.

Doxorubicin (DOX) is the most widely used chemotherapeutic drug. Although it has been standardized as an anticancer drug and has potential diverse toxicities, the clinical use of DOX is restricted [20]. In order to minimize the side effects, an efficient strategy is using nanoparticles as carriers for DOX delivery [21–23]. The novel drug delivery system in my manuscript is named as Fe_3O_4 -TIPTS-g-(PEI-co-PEG). PEI and PEG were grafted Fe_3O_4 through TIPTS, which may load DOX to improve selective cytotoxicity of the drug to targeted cells and reduce the systemic toxicity to normal cells.

In normal tissues, the extracellular pH is relatively basic (pH = 7.4), whereas in tumor tissues, the pH is close to endosomes (pH = 5.0 – 6.0) or lysosomes (pH = 4.5 – 5.0) [24]. This difference provides a new idea for cancer treatment, which is to build a pH-sensitive drug delivery system. In the present paper, the $-\text{NH}_2$ group belonging to PEI of Fe_3O_4 -TIPTS-g-(PEI-co-PEG) reacts with the $-\text{C}=\text{O}$ group of DOX, and the resulting bond is the hydrazone bond. The hydrazone bond is kept stable in physiological condition; once the pH value decreases to 4.0–6.0, the hydrazone bond becomes unstable and then releases *massive drugs* [25, 26]. This pH-triggered delivery system will improve the efficacy of DOX while decreasing its cytotoxicity toward healthy cells (Scheme 1).

2. Experimental

2.1. Materials and Reagents. TIPTS were lab-made by ourselves. $\text{FeCl}_3 \cdot 6\text{H}_2\text{O}$, $\text{FeCl}_2 \cdot 4\text{H}_2\text{O}$, PEG [Mn = 2000], and DOX were purchased from Aladdin Industrial Corporation (Shanghai, China). PEI was purchased from Sigma-Aldrich Industrial Corporation (Shanghai, China). Ethanol was purchased from Tianjin Fuyu Chemical Corporation Limited (Tianjin, China). N-hexane and $\text{NH}_3 \cdot \text{H}_2\text{O}$ was purchased from Tianjin Kemiou Chemical Reagent Corporation Lim-

ited (Tianjin, China). Methylbenzene was purchased from Aladdin Industrial Corporation (Shanghai, China). All of the chemicals were AR grade and were used as received without any purification. H_2O for laboratory experiments used was obtained after distillation.

2.2. Synthesis Procedure

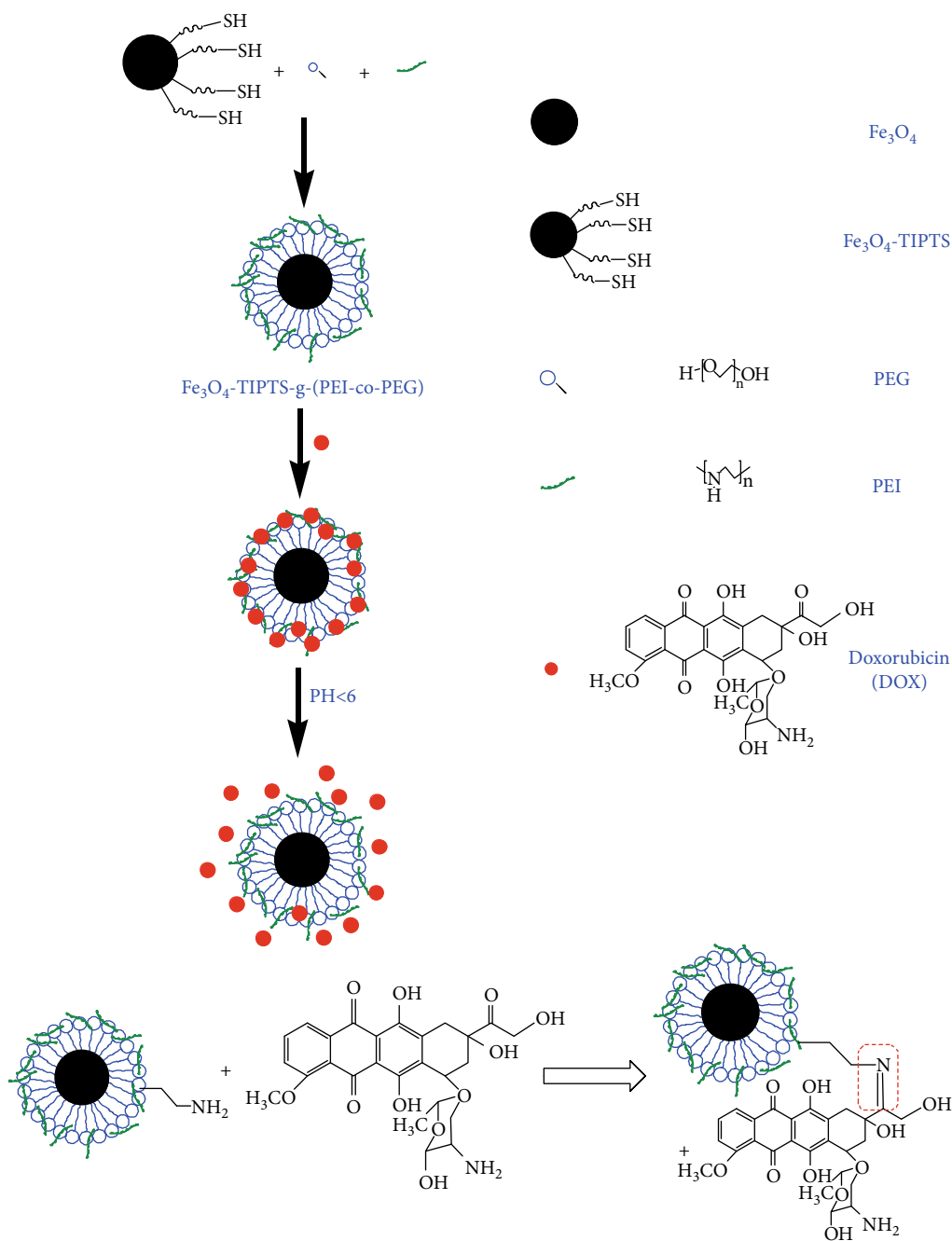
2.2.1. Synthesis of Fe_3O_4 Nanoparticles. The coprecipitation method was used to prepare the Fe_3O_4 nanoparticles: $\text{FeCl}_3 \cdot 6\text{H}_2\text{O}$ (16.2 g) and $\text{FeCl}_2 \cdot 4\text{H}_2\text{O}$ (8.1 g) in a 1 : 2 molar ratio were dissolved in distilled water (175 ml) under nitrogen atmosphere with vigorous stirring. As the solution was heated to 70°C, $\text{NH}_3 \cdot \text{H}_2\text{O}$ (28 wt%, 25 ml) was added dropwise to the solution until the pH of the solution is controlled at 10.0, under vigorous stirring, and the reaction was allowed to proceed for 5 h at 70°C. And then, the temperature was increased to 85°C to vapor the residual NH_3 , then discard the excessive-iron ions by the magnetic separation procedure and filter. This part of the experiment process is shown in Scheme 2.

2.2.2. Synthesis of Thiol-Functionalized Fe_3O_4 Nanoparticles (Fe_3O_4 -TIPTS). Fe_3O_4 nanoparticles were prepared by $\text{FeCl}_3 \cdot 6\text{H}_2\text{O}$ and $\text{FeCl}_2 \cdot 4\text{H}_2\text{O}$ in a coprecipitation method. Briefly, 25 ml methylbenzene and 1 g Fe_3O_4 nanoparticles were stirred at room temperature for 30 min. This was followed by the addition of 4 g TIPTS [27] (preparation of a lab-made novel thiol-containing silane coupling agent TIPTS was described in reference 39) and further stirring until dissolution was complete. Under purified N_2 atmosphere, this solution was heated to 65°C in a water bath, stirring for 8 h. Finally, the resulting product was filtered, washed with distilled methylbenzene for three times, and dried under vacuum for 24 h. This part of the experiment process is shown in Scheme 3.

2.2.3. Synthesis of Fe_3O_4 -TIPTS-g-(PEI-co-PEG). Fe_3O_4 -TIPTS (1.77 g) was dissolved in 50 ml methylbenzene and stirred at room temperature for 30 min. Followed by the addition of 4.425 g PEI dissolved in 10 ml ethanol and 10 g PEG dissolved in 20 ml methylbenzene. This solution was heated to 55°C in a water bath, continuous flow of nitrogen into the stream, stirring for 8 h. Finally, the resulting product was filtered, washed with distilled water for three times, and dried under vacuum for 24 h. This part of the experiment process is shown in Scheme 4.

2.2.4. Drug Loading. To load DOX on modified MNPs, 20 mg dry Fe_3O_4 -TIPTS-g-(PEI-co-PEG) was dispersed in 8 ml DMSO; 3 mg DOX was added and allowed to react with the nanoparticles for 24 h in the dark. The resulted products were collected by magnetic decantation and washed twice with deionized water. The DOX-loaded Fe_3O_4 -TIPTS-g-(PEI-co-PEG) were freeze-dried and stored in the dark at 4°C. The amount of unbound DOX was quantified using a UV-Vis spectrophotometer at 420 nm.

2.2.5. In Vitro Release Studies. Briefly, 0.01 M phosphate buffer solution (PBS) was prepared at three different pH values (4.5, 5.5, and 7.4) which each pH was chosen to imitate



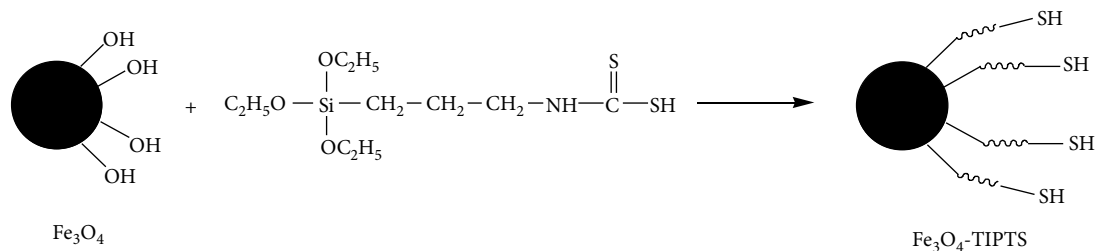
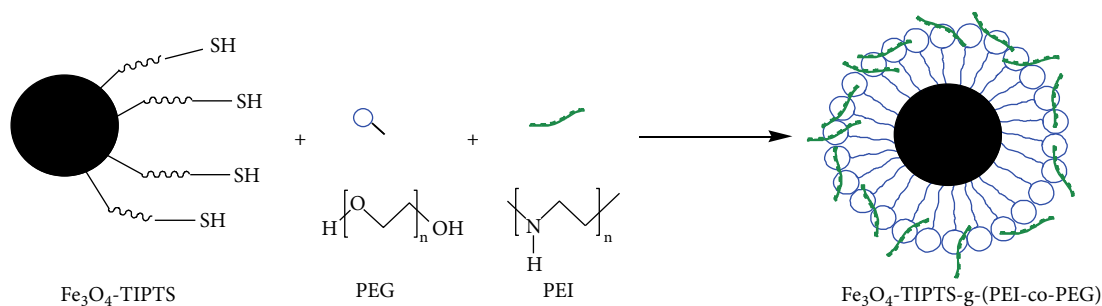
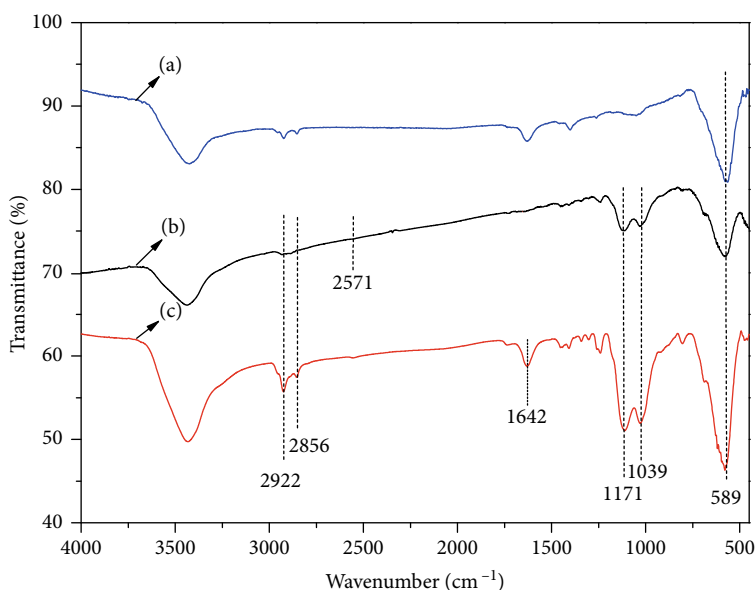
SCHEME 1: Outline for the preparation of Fe_3O_4 -TIPTS-g-(PEI-co-PEG), drug loading, and in vitro release studies.



SCHEME 2: The preparation of Fe_3O_4 nanoparticles.

conditions either within tumors or within normal tissues. 10 mg DOX-loaded Fe_3O_4 -TIPTS-g-(PEI-co-PEG) was dispersed in 3 ml PBS and then transferred to a dialysis bag that was immersed in 50 ml of the same medium. At selected time intervals, 3 ml PBS outside the dialysis bag was removed for analysis and replaced by the same volume of fresh PBS. The release experiments of each pH were conducted in triplicate.

2.3. Characterization. The samples compressed with KBr were analyzed by a FTIR spectrometer (Spectrum Two, PerkinElmer Company of United States of America) at room temperature, the spectral range was $450\text{--}4000\text{ cm}^{-1}$, and the spectral resolution was 4 cm^{-1} . The X-ray intensity was measured in the range of $10^\circ < 2\theta < 80^\circ$ with a scan speed of $2\theta/\text{min}$. A Beckman Coulter LS-880 Laser Diffraction Particle Size analyzer was used in this study. Its measuring range was $0.01\text{ }\mu\text{m}$ to $2000\text{ }\mu\text{m}$. With its PIDS (Polarization Intensity Differential Scattering) assembly, lower size limit could be extended to as low as $0.04\text{ }\mu\text{m}$. X-ray powder diffraction (XRD) analysis was performed using Rigaku Dmax2200PC

SCHEME 3: The preparation of $\text{Fe}_3\text{O}_4\text{-TIPTS}$.SCHEME 4: The preparation of $\text{Fe}_3\text{O}_4\text{-TIPTS-g-(PEI-co-PEG)}$.FIGURE 1: FTIR spectra of products. (a) Fe_3O_4 . (b) $\text{Fe}_3\text{O}_4\text{-TIPTS}$. (c) $\text{Fe}_3\text{O}_4\text{-TIPTS-g-(PEI-co-PEG)}$.

diffractometer (Rigaku Corporation, Tokyo, Japan) and Cu K-radiation. The magnetic properties of the products were determined by a vibrating sample magnetometer (VSM) (VL-072, Quantum Design Company of United States of America). UV-vis spectra were measured on a UV-vis spectrometer (Lambda 35, PerkinElmer Company of United States of America).

3. Results and Discussion

3.1. The Preparation of $\text{Fe}_3\text{O}_4\text{-TIPTS-g-(PEI-co-PEG)}$

3.1.1. FTIR Analysis. FTIR spectra of products are shown in Figure 1. From these curves, the peak could be seen at 589 cm^{-1} attributed to the stretching vibration of the Fe-O group, the peak could be seen at 1039 cm^{-1} attributed to the stretching vibration of the C-H group, the peak could be seen at 1171 cm^{-1} attributed to the C-C group, the peak could be seen at 1642 cm^{-1} attributed to the C-OH group, the peak could be seen at 2571 cm^{-1} attributed to the -SH group, and the peak could be seen at 2856 cm^{-1} and 2922 cm^{-1} attributed to the stretching vibration of the - CH_2 group.

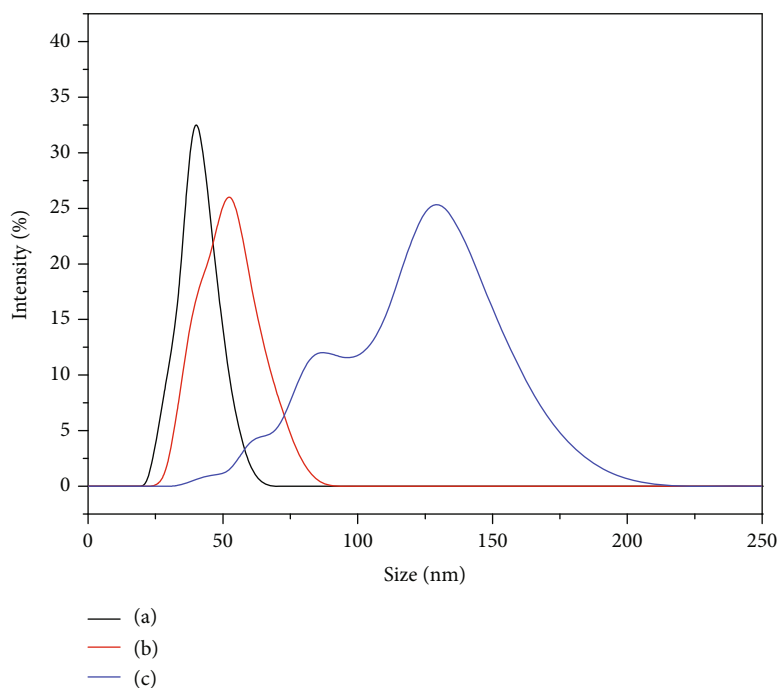


FIGURE 2: The particle size spectra of products. (a) Fe_3O_4 . (b) Fe_3O_4 -TIPTS. (c) Fe_3O_4 -TIPTS-g-(PEI-co-PEG).

From curve (a), curve (b) and curve (c), the peak at 2856 cm^{-1} and 2922 cm^{-1} could only be seen at curve (b) and curve (c), not at curve (a), because TIPTS and copolymer could make nano- Fe_3O_4 organized. The peak at 2571 cm^{-1} could only be seen at curve (b), because the -SH group was decomposed to obtain free radicals for grafting two polymers on Fe_3O_4 -TIPTS. The peak at 1642 cm^{-1} could only be seen at curve (b), because the C-OH group belongs to PEI, which further indicated that polymers were successful to be grafted on Fe_3O_4 -TIPTS.

3.1.2. Particle Size Analysis. The particle size spectra for Fe_3O_4 , Fe_3O_4 -TIPTS and Fe_3O_4 -TIPTS-g-(PEI-co-PEG) are shown in Figure 2. The results showed that the diameter size of Fe_3O_4 was 39.6 nm, the diameter size of Fe_3O_4 -TIPTS was 47.6 nm, and the diameter size of Fe_3O_4 -TIPTS-g-(PEI-co-PEG) was 112.8 nm. It indicated that the diameter size of the latter one is gradually larger than the diameter size of the previous one, because TIPTS by lab-made could modify Fe_3O_4 in a smooth way. Moreover, TIPTS could also obtain free radicals for grafting PEI and PEG onto the surface of Fe_3O_4 -TIPTS. And then, the diameter size results of all products were between 20 and 150 nm, which is beneficial to the absorption of endothelial reticular system and recognition of phagocytic cells.

3.1.3. XRD Analysis. The XRD spectra for the products for Fe_3O_4 and Fe_3O_4 -TIPTS-g-(PEI-co-PEG) are shown in Figure 3. The crystal lattice change of Fe_3O_4 upon grafting of PEI and PEG was investigated using XRD analysis. The Fe_3O_4 exhibited several sharp peaks at 18.21 (1 1 1), 29.96 (2 2 0), 35.28 (3 1 1), 42.88 (4 0 0), 53.18 (4 2 2), 56.69 (5 1 1), 62.25 (4 4 0), and 74.62 (6 2 2), respectively, as shown in

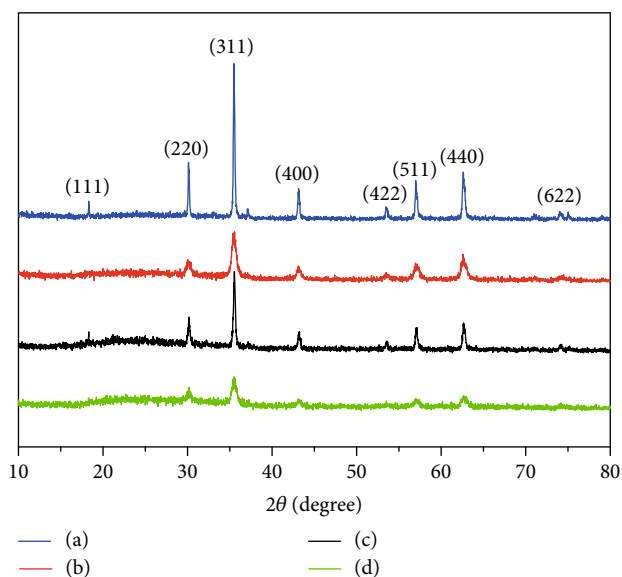


FIGURE 3: XRD spectra of products. (a) Fe_3O_4 . (b) Fe_3O_4 -TIPTS. (c) Fe_3O_4 -TIPTS-g-(PEI-co-PEG). (d) Loading DOX onto Fe_3O_4 -TIPTS-g-(PEI-co-PEG).

Figure 3. The broad peak from 17.58 to 31.88 of the XRD curve showed that PEI and PEG prepared in the absence of Fe_3O_4 was amorphous. The reflection peaks of Fe_3O_4 -TIPTS-g-(PEI-co-PEG) could all be ascribed to the crystal planes of Fe_3O_4 . The broad weak diffraction peak of PEI and PEG did not affect the crystal lattice of Fe_3O_4 . This observation indicated that the composite sample had a still ordered arrangement than PEI and PEG owing to the inclusion of Fe_3O_4 . The performance which was targetable drug delivery of Fe_3O_4 was not affected by the grafted polymer.

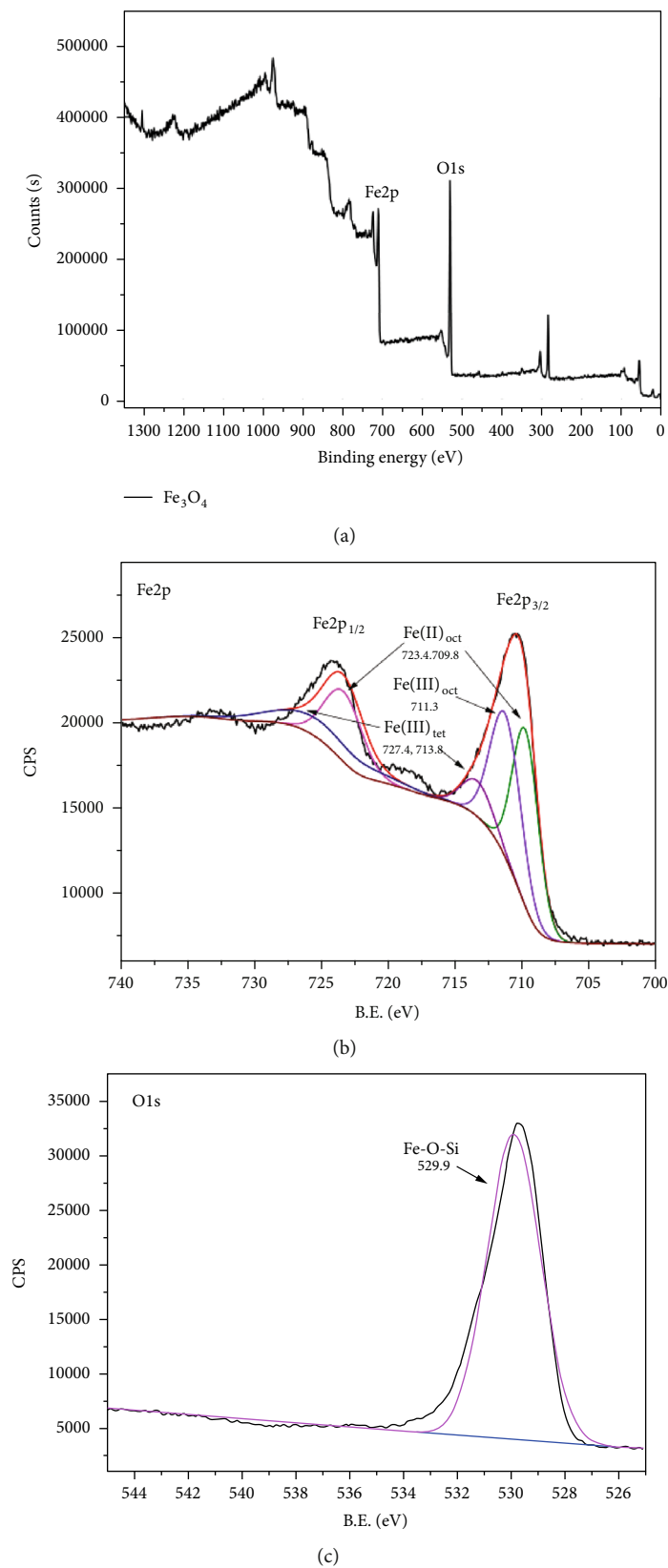
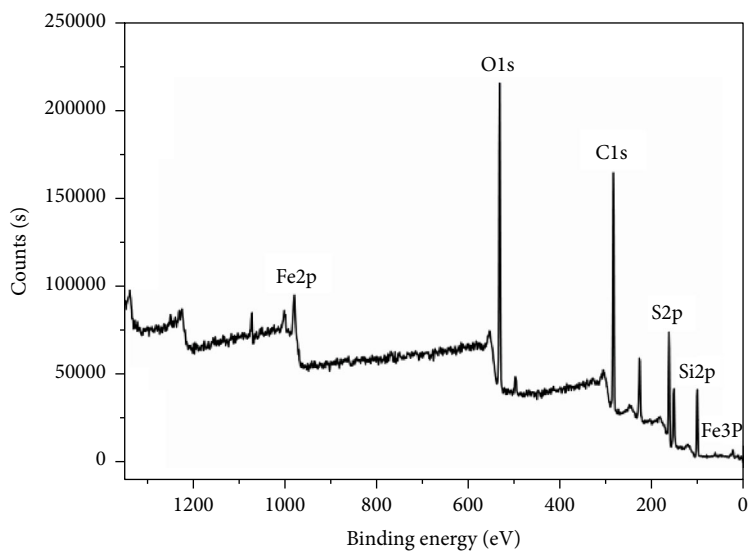
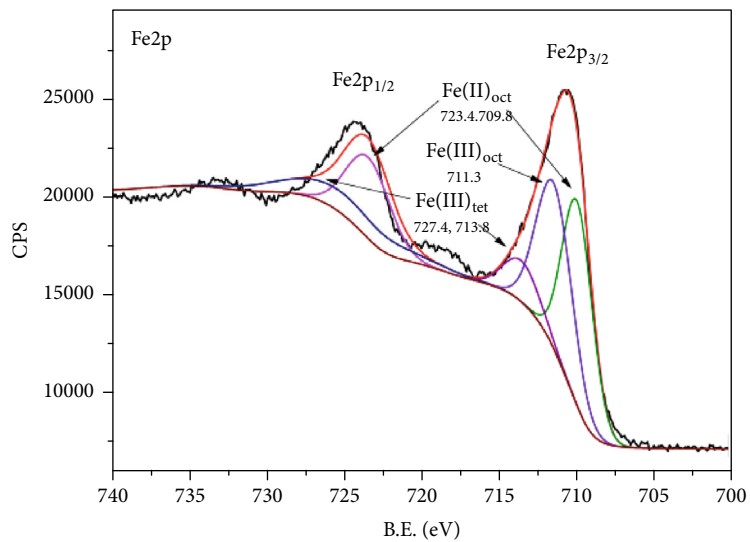


FIGURE 4: XPS spectra of Fe_3O_4 . (a) Full spectrum of Fe_3O_4 . (b) Peak separation of Fe. (c) Peak separation of O.

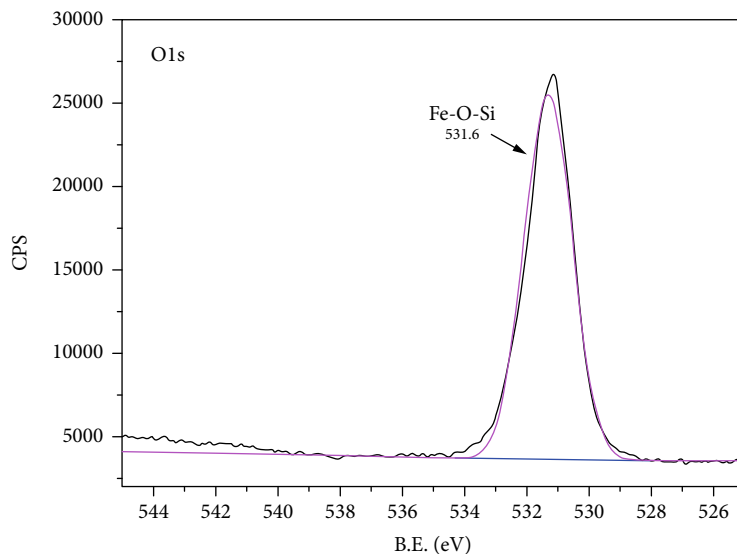


(a)

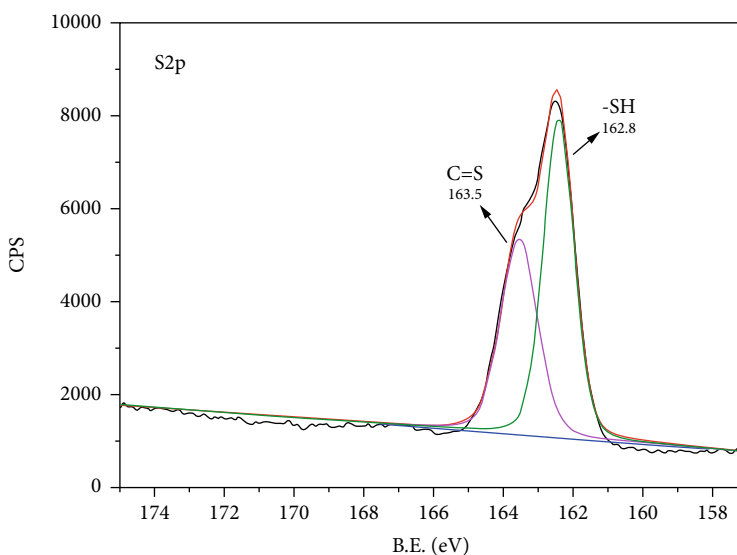


(b)

FIGURE 5: Continued.



(c)



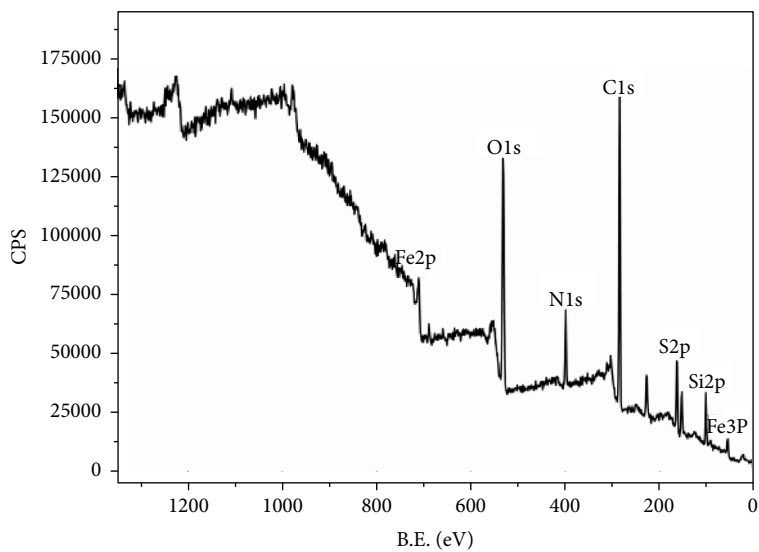
(d)

FIGURE 5: XPS spectra of Fe_3O_4 -TIPTS. (a) Full spectrum of Fe_3O_4 -TIPTS. (b) Peak separation of Fe. (c) Peak separation of O. (d) Peak separation of S.

3.1.4. XPS Analysis. From Figures 4–6, it separately showed XPS spectra of Fe_3O_4 , Fe_3O_4 -TIPTS, and Fe_3O_4 -TIPTS-g-(PEI-co-PEG). Every full spectra contained all the distinct peaks of the elements, and the location was accurate. Peak separation of each element was obtained by peak separation and fitting for each element. Every peak separation by Fe of Fe_3O_4 , Fe_3O_4 -TIPTS, and Fe_3O_4 -TIPTS-g-(PEI-co-PEG) was exactly the same. Every peak separation by S and O of Fe_3O_4 , Fe_3O_4 -TIPTS and Fe_3O_4 -TIPTS-g-(PEI-co-PEG) appeared different, but the fitting results are consistent with the whole curve. The above results further prove that the structure of Fe_3O_4 , Fe_3O_4 -TIPTS and Fe_3O_4 -TIPTS-g-(PEI-co-PEG) prepared by the experiment were accurate.

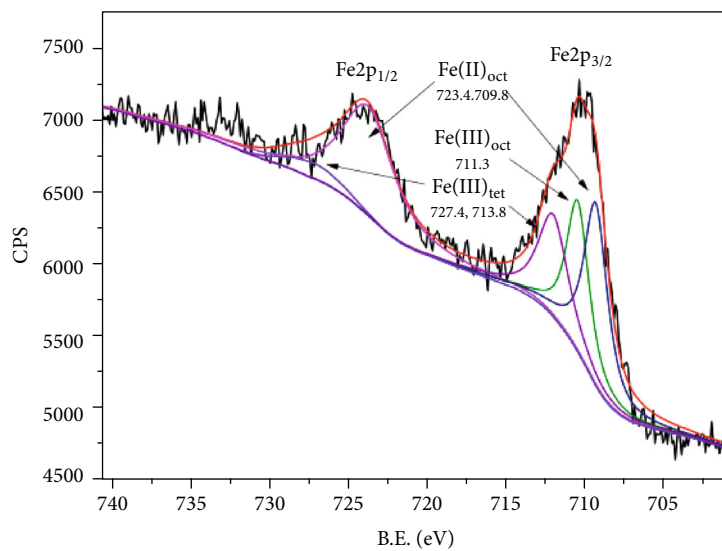
3.1.5. VSM Analysis. Neither the remanence nor the coercivity was observed in the three hysteresis curves; therefore, the

magnetization results shown in Figure 7 suggested that Fe_3O_4 -TIPTS-g-(PEI-co-PEG) was indeed superparamagnetic and had a strong magnetic response. They exhibited superparamagnetism with the saturation magnetization (M_s) values of 68.23, 63.58, and 55.22 emu/g at 25°C, respectively. It indicated that the polymerization did not affect the magnetic properties of the superparamagnetic nanoparticles because the structure of the Fe_3O_4 nanoparticles remained in the polymerization procedure. Therefore, the DOX-loaded Fe_3O_4 -TIPTS-g-(PEI-co-PEG) can be easily controlled by an external magnetic field to accurately deliver DOX to the target area. Furthermore, the decrease in the saturation magnetization of the Fe_3O_4 -TIPTS and Fe_3O_4 -TIPTS-g-(PEI-co-PEG) nanoparticles compared with the Fe_3O_4 was ascribed to the TIPTS and the copolymer of PEI and PEG ingredients grafted.



— $\text{Fe}_3\text{O}_4\text{-g-(PEI-co-PEG)}$

(a)



(b)

FIGURE 6: Continued.

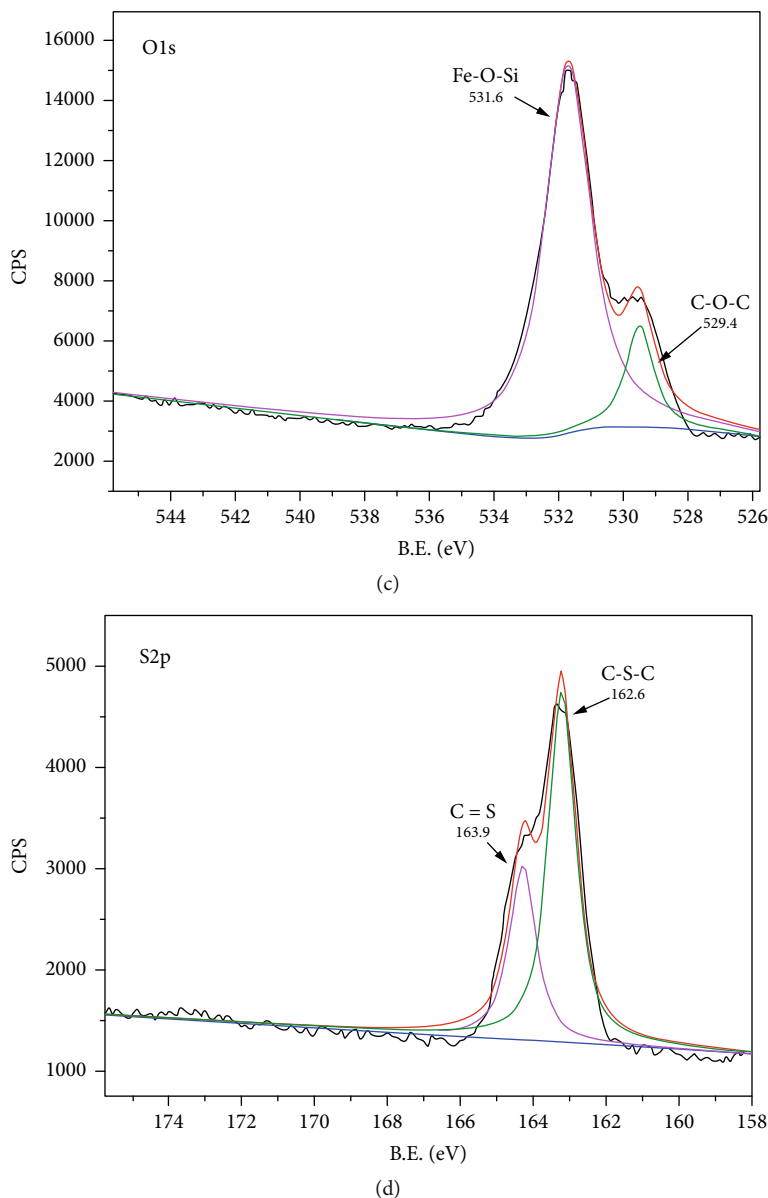


FIGURE 6: XPS spectra of Fe_3O_4 -TIPTS-g-(PEI-co-PEG). (a) Full spectrum of Fe_3O_4 -TIPTS-g-(PEI-co-PEG). (b) Peak separation of Fe. (c) Peak separation of O. (d) Peak separation of S.

3.1.6. SEM Analysis. From Figure 8, it showed SEM images of Fe_3O_4 , Fe_3O_4 -TIPTS, and Fe_3O_4 -TIPTS-g-(PEI-co-PEG), respectively. From Figure 8(a), the Fe_3O_4 synthesized by the method in this paper presented a uniform particle size, and each nano-microsphere is basically in an independent state. Figure 8(b) shows the higher magnification image of Fe_3O_4 -TIPTS; it could be seen that TIPTS (a silane surface modifier with thiols group) was grafted on the surface of Fe_3O_4 . Figure 8(c) shows the higher magnification image of Fe_3O_4 -TIPTS-g-(PEI-co-PEG). Under the action of a mercapto group, branching and cluster polymers were formed by PEI and PEG grafted onto Fe_3O_4 . And then, the particle size of Fe_3O_4 -TIPTS-g-(PEI-co-PEG) was uneven due to the difference in the amount of the graft polymer.

3.2. Drug Loading and In Vitro Release Studies

3.2.1. FTIR Analysis. FTIR spectra of DOX and DOX-loaded Fe_3O_4 -TIPTS-g-(PEI-co-PEG) are shown in Figure 9. From these curves, the peak could be seen at 558 cm^{-1} attributed to the stretching vibration of the Fe-O group, the peak could be seen at 2851 cm^{-1} and 2920 cm^{-1} attributed to the stretching vibration of the $-\text{CH}_2$ group, the peak at 3332 cm^{-1} could be attributed to the O-H groups of PEG and DOX. The peaks at 1617 cm^{-1} could be attributed to N-H bending. The peaks at 1280 cm^{-1} could be attributed to C-N stretching modes. The peaks at 1408 cm^{-1} could be attributed to quinine. The peaks at $1,285\text{ cm}^{-1}$ could be attributed to anthracycline. The peaks at 1730 cm^{-1} could be attributed to 13-carbonyl

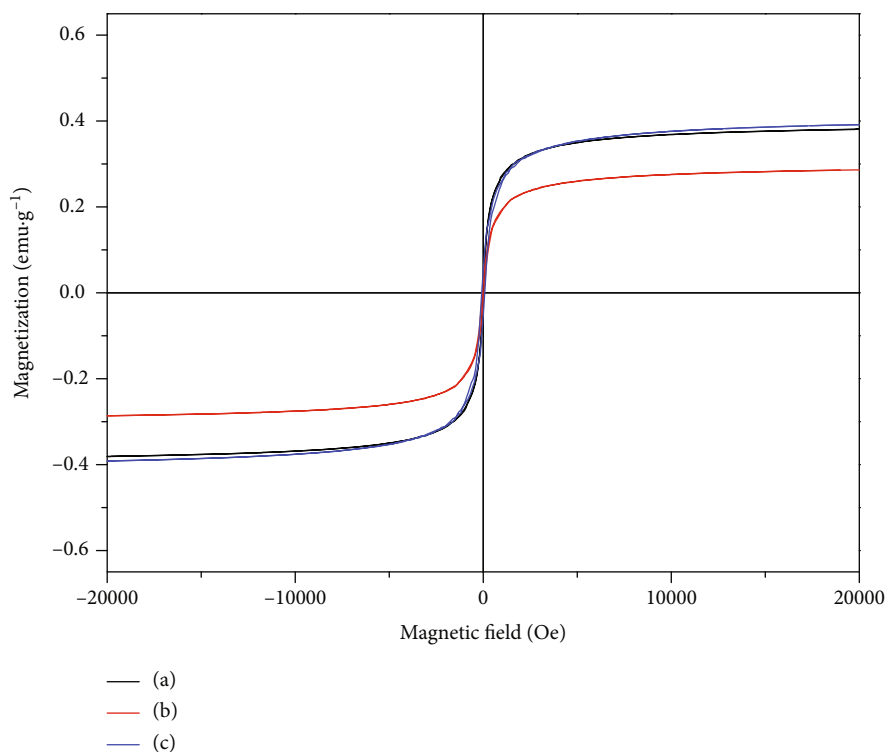


FIGURE 7: VSM measurements. (a) Fe_3O_4 ; (b) Fe_3O_4 -TIPTS; (c) Fe_3O_4 -TIPTS-g-(PEI-co-PEG).

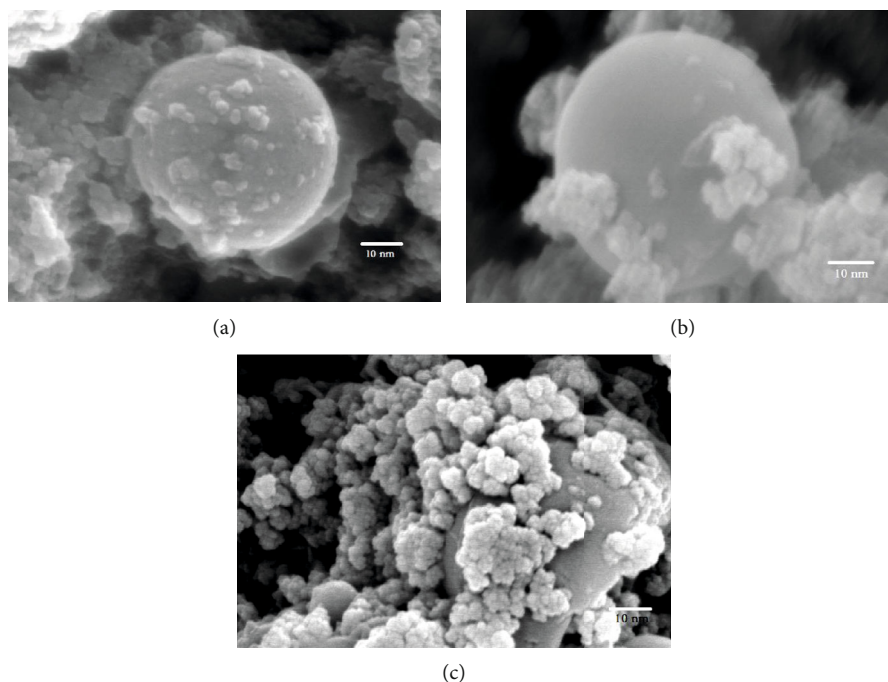


FIGURE 8: SEM images of the products. (a) Fe_3O_4 ; (b) Fe_3O_4 -TIPTS; (c) Fe_3O_4 -TIPTS-g-(PEI-co-PEG).

moieties. 1343 cm^{-1} could be attributed to hydrazone bond. The quinone, anthracycline, and 13-carbonyl moieties were all in DOX. Through comparison, the peak at 1730 cm^{-1} does not appear in DOX-loaded Fe_3O_4 -TIPTS-g-(PEI-co-PEG)

and the peak at 1343 cm^{-1} was the characteristic peak only appear in the curve of DOX-loaded Fe_3O_4 -TIPTS-g-(PEI-co-PEG). In summary, DOX was successfully loaded onto Fe_3O_4 -TIPTS-g-(PEI-co-PEG).

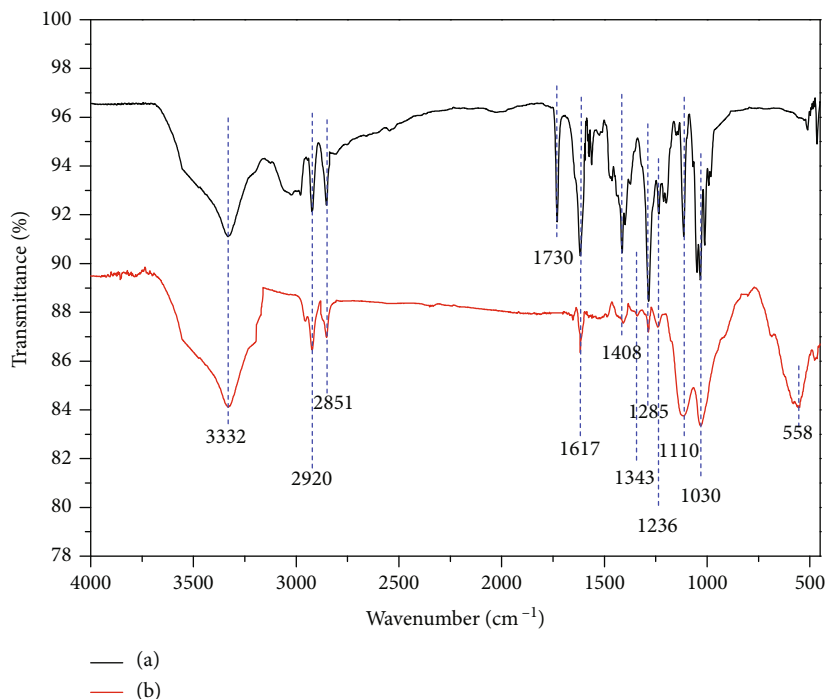


FIGURE 9: FTIR spectra of products. (a) DOX; (b) DOX-loaded Fe_3O_4 -TIPTS-g-(PEI-co-PEG).

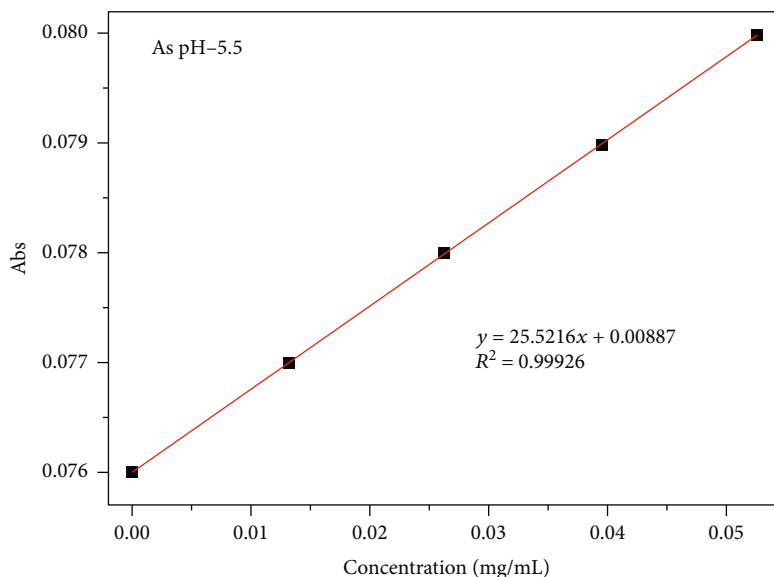


FIGURE 10: Standard curve of vitro release of DOX.

3.2.2. In Vitro Release Studies. The results of vitro release are shown in Figure 10. In vitro release studies of DOX over time were studied by monitoring the absorbance at 482 nm. In vitro release of DOX from Fe_3O_4 -TIPTS-g-(PEI-co-PEG) was simulated at 37°C . Standard curve was calculated at pH 5.5. The relationship between the absorption value (Abs) and the concentration is derived according to

$$\text{Abs} = \left(V * c_1 + V^i * \sum c_i \right) / m_{\text{drug}} \quad (1)$$

Thus, the standard curve of vitro release of DOX was

$$y = 25.5216x + 0.00887 (R^2 = 0.99926). \quad (2)$$

The result of pH sensitive about vitro release of DOX is shown in Figure 11. It indicated that DOX onto Fe_3O_4 -TIPTS-g-(PEI-co-PEG) was relatively stable at blood pH and more effectively released its payload at pH = 4.5 than pH = 5.5 or pH = 7.4. The functionalized particles slowly released DOX over 80 h at 37°C under pH 4.5 (lysosomes),

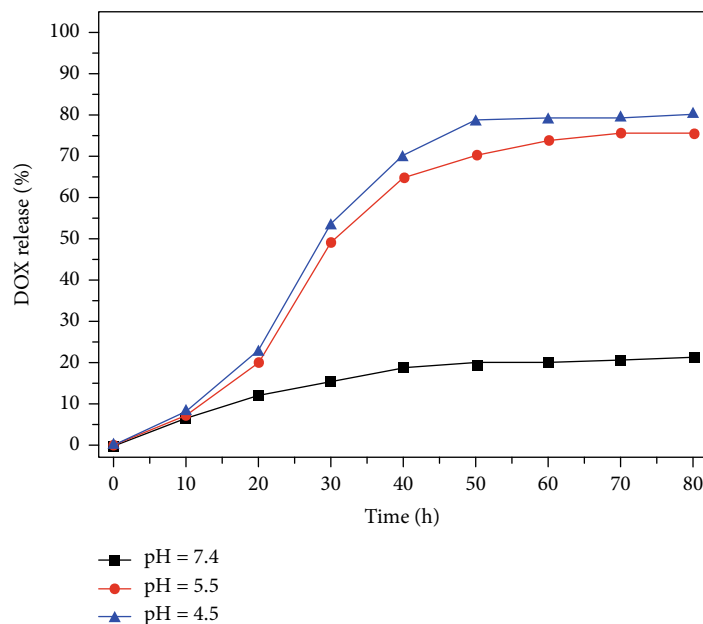


FIGURE 11: In vitro release of DOX at pH 4.5, 5.5, and 7.4.

5.5 (endosomes), and 7.4 (normal tissues) PBS solutions, which was both time- and pH-dependent; the cumulative dissolution profiles of nanoparticles are shown in Figure 11. It indicated that only 21.06% of drug was released from Fe_3O_4 -TIPTS-g-(PEI-co-PEG) at pH 7.4, separately, over the process of 80 h, while at pH 5.5, it demonstrated higher release satisfied with 75.68% and at pH = 4.5 up to 80.24%. The result indicated that nanoparticles under acidic conditions showed higher DOX release rates at endosomal pH (4.5–5.5) as compared with normal tissues pH (7.4). This phenomenon could be attributed to the fact that after placing Fe_3O_4 -TIPTS-g-(PEI-co-PEG) in acidic PBS, the C=N bond between DOX and Fe_3O_4 -TIPTS-g-(PEI-co-PEG) is attacked by H^+ , releasing DOX. While from pH 5.5 to 4.5, the release rate of DOX was also increased slightly. This phenomenon was due to the protonation of the DOX amino group, which could give DOX a positive charge to enhance its solubility in acidic conditions; accordingly, a faster drug release was caused.

4. Conclusion

In summary, our research results have synthesized a DOX-loaded pH-sensitive magnetic system for targeted drug delivery. Nano- Fe_3O_4 was modified by the mercaptosilane surface modifier TIPTS, and block copolymer poly(ethylene glycol-co-ethyleneimine) grafted Fe_3O_4 to obtain Fe_3O_4 -TIPTS-g-(PEI-co-PEG). The nano- Fe_3O_4 was a core of Fe_3O_4 -TIPTS-g-(PEI-co-PEG) which possesses the targeted function. DOX was bonded with Fe_3O_4 -TIPTS-g-(PEI-co-PEG) by a hydrazone bond. At different pH, the hydrazone bond could act as the switch to control the release of the drug encapsulated, so the potential of DOX-loaded Fe_3O_4 -TIPTS-g-(PEI-co-PEG) as the carrier for pH-sensitive drug release is demonstrated. In vitro, DOX was released more readily at pH 4.5, which 80.24% DOX was released within

80 h. Therefore, the results demonstrate the versatility of the DOX-loaded magnetic nanoparticles as a potential anti-tumor drug delivery system.

Data Availability

The data used to support the findings of this study are available from the corresponding author upon request.

Conflicts of Interest

No potential conflict of interest was reported by the authors.

Acknowledgments

The authors are grateful for support from the National Natural Science Foundation of China (grant number: 21376127), the Scientific Research Projects Foundation of Heilongjiang Education Department (grant number: YSTSXK201860), and the Fundamental Research Funds in Heilongjiang Provincial Universities (grant number: 135309110).

References

- [1] J. Xi, L. Da, C. Yang et al., “ Mn^{2+} -coordinated PDA@-DOX/PLGA nanoparticles as a smart theranostic agent for synergistic chemo-photothermal tumor therapy,” *International Journal of Nanomedicine*, vol. 12, pp. 3331–3345, 2017.
- [2] U. Sang Shin, J. W. Seo, B. Kundu, H. W. Kim, and M. Eltohamy, “Super-magnetic smart hybrid doxorubicin loaded nanoparticles effectively target breast adenocarcinoma cells,” *Microporous and Mesoporous Materials*, vol. 243, pp. 206–213, 2017.
- [3] F. Farvadi, A. M. Tamaddon, Z. Sobhani, and S. S. Abolmaali, “Polyionic complex of single-walled carbon nanotubes and

- PEG-grafted-hyperbranched polyethyleneimine (PEG-PEI-SWNT) for an improved doxorubicin loading and delivery: development and in vitro characterization,” *Artificial Cells, Nanomedicine, and Biotechnology*, vol. 45, no. 5, pp. 855–863, 2017.
- [4] R. Klingeler, S. Hampel, and B. Büchner, “Carbon nanotube based biomedical agents for heating, temperature sensing and drug delivery,” *International Journal of Hyperthermia*, vol. 24, no. 6, pp. 496–505, 2009.
- [5] L. Huang, L. Ao, W. Wang, D. Hu, Z. Sheng, and W. Su, “Multifunctional magnetic silica nanotubes for MR imaging and targeted drug delivery,” *Chemical Communications*, vol. 51, no. 18, pp. 3923–3926, 2015.
- [6] H. Song, F. Quan, Z. Yu et al., “Carboplatin prodrug conjugated Fe₃O₄ nanoparticles for magnetically targeted drug delivery in ovarian cancer cells,” *Journal of Materials Chemistry B*, vol. 7, no. 3, pp. 433–442, 2019.
- [7] A. Nordborg, F. Limé, A. Shchukarev, and K. Irgum, “A cation-exchange material for protein separations based on grafting of thiol-terminated sulfoethyl methacrylate telomers onto hydrophilized monodisperse divinylbenzene particles,” *Journal of Separation Science*, vol. 31, no. 12, pp. 2143–2150, 2008.
- [8] A. Beiraghi, K. Pourghazi, and M. Amoli-Diva, “Au nanoparticle grafted thiol modified magnetic nanoparticle solid phase extraction coupled with high performance liquid chromatography for determination of steroid hormones in human plasma and urine,” *Analytical Methods*, vol. 6, no. 5, pp. 1418–1426, 2014.
- [9] A. H. M. Yusoff, N. S. Midhat, and F. J. Mohd, “Synthesis and characterization of biocompatible Fe₃O₄ nanoparticles at different pH,” *Advanced Materials Technologies*, vol. 1835, no. 1, article 020010, 2017.
- [10] S. Davaran, D. Asgari, S. Davaran et al., “Preparation and in vitro evaluation of doxorubicin-loaded Fe₃O₄ magnetic nanoparticles modified with biocompatible copolymers,” *International Journal of Nanomedicine*, vol. 7, pp. 511–526, 2012.
- [11] L. Sun, J. Wang, and Z. Wang, “Recognition and transmembrane delivery of bioconjugated Fe₂O₃@Au nanoparticles with living cells,” *Nanoscale*, vol. 2, no. 2, pp. 269–276, 2010.
- [12] D. Li, M. Hua, K. Fang, and R. Liang, “BSA directed-synthesis of biocompatible Fe₃O₄ nanoparticles for dual-modal T₁ and T₂ MR imaging *in vivo*,” *Analytical Methods*, vol. 9, no. 21, pp. 3099–3104, 2017.
- [13] J. Yang, M. Pan, R. Shi et al., “Novel Fe₃O₄ Hollow microspheres: nontemplate hydrothermal synthesis, superparamagnetism and biocompatibility,” *Nanoscience and Nanotechnology Letters*, vol. 9, no. 2, pp. 109–117, 2017.
- [14] D. Li, M. Deng, Z. Yu et al., “Biocompatible and stable GO-coated Fe₃O₄ Nanocomposite: a robust drug delivery carrier for simultaneous tumor MR imaging and targeted therapy,” *ACS Biomaterials Science & Engineering*, vol. 4, no. 6, pp. 2143–2154, 2018.
- [15] Z. Li, X. Liu, X. Chen, M. X. Chua, and Y. L. Wu, “Targeted delivery of Bcl-2 conversion gene by MPEG-PCL-PEI-FA cationic copolymer to combat therapeutic resistant cancer,” *Materials Science And Engineering: C*, vol. 76, pp. 66–72, 2017.
- [16] H. Shao, J. Qi, T. Lin, Y. Zhou, and F. Yu, “Characterization of Fe₃O₄@CS@NMDP magnetic nanoparticles with core-shell structure prepared by chemical cross-linking method,” *Functional Materials Letters*, vol. 10, no. 5, article 1750056, 2017.
- [17] J. V. Jokerst, T. Lobovkina, R. N. Zare, and S. Gambhir, “Nanoparticle PEGylation for imaging and therapy,” *Nanomedicine*, vol. 6, no. 4, pp. 715–728, 2011.
- [18] Y. Fang, J. Xue, S. Gao et al., “Cleavable PEGylation: a strategy for overcoming the “PEG dilemma” in efficient drug delivery,” *Drug Delivery*, vol. 24, no. 2, pp. 22–32, 2017.
- [19] H. Danafar, A. Sharafi, H. Kheiri Manjili, and S. Andalib, “Sulforaphane delivery using mPEG-PCL co-polymer nanoparticles to breast cancer cells,” *Pharmaceutical Development and Technology*, vol. 22, no. 5, pp. 642–651, 2017.
- [20] A. Pugazhendhi, T. N. J. I. Edison, B. K. Velmurugan, J. A. Jacob, and I. Karuppusamy, “Toxicity of doxorubicin (Dox) to different experimental organ systems,” *Life Sciences*, vol. 200, pp. 26–30, 2018.
- [21] M. I. Majeed, Q. Lu, W. Yan et al., “Highly water-soluble magnetic iron oxide (Fe₃O₄) nanoparticles for drug delivery: enhanced in vitro therapeutic efficacy of doxorubicin and MION conjugates,” *Journal Of Materials Chemistry B*, vol. 1, no. 22, pp. 2874–2884, 2013.
- [22] C. H. Fan, Y. H. Cheng, C. Y. Ting et al., “Ultrasound/magnetic targeting with SPIO-DOX-microbubble complex for image-guided drug delivery in brain tumors,” *Theranostics*, vol. 6, no. 10, pp. 1542–1556, 2016.
- [23] X. Jia, Z. Yang, Y. Wang et al., “Hollow mesoporous silica@metal-organic framework and applications for pH-responsive drug delivery,” *ChemMedChem*, vol. 13, no. 5, pp. 400–405, 2018.
- [24] Z. Zhou, F. Hu, S. Hu et al., “pH-activated nanoparticles with targeting for the treatment of oral plaque biofilm,” *Journal of Materials Chemistry B*, vol. 6, no. 4, pp. 586–592, 2018.
- [25] M. Huan, B. Zhang, Z. Teng et al., “In vitro and in vivo antitumor activity of a novel pH-activated polymeric drug delivery system for doxorubicin,” *PLoS One*, vol. 7, no. 9, article e44116, 2012.
- [26] W. Chen, F. Meng, R. Cheng, and Z. Zhong, “pH-sensitive degradable polymersomes for triggered release of anticancer drugs: a comparative study with micelles,” *Journal of Controlled Release Official Journal of the Controlled Release Society*, vol. 142, no. 1, pp. 40–46, 2010.
- [27] W. Xue-Ying, W. Ya-Zhen, D. Yu-Tao, L. Tian-Yu, and Z. Li-Wu, “Preparation and thermal decomposition kinetics of novel silane coupling agent with mercapto group,” *Journal of Nanomaterials*, vol. 2019, Article ID 6089065, 9 pages, 2019.

Research Article

Preparation and Thermal Decomposition Kinetics of Novel Silane Coupling Agent with Mercapto Group

Wu Xue-ying,¹ Wang Ya-zhen ,^{2,3} Di Yu-tao,¹ Lan Tian-yu,^{2,3} and Zu Li-wu^{2,3}

¹College of Chemistry and Chemical Engineering, Qiqihar University, Qiqihar, 161006 Heilongjiang, China

²College of Materials Science and Engineering, Qiqihar University, Qiqihar, 161006 Heilongjiang, China

³Heilongjiang Key Laboratory of Polymer Matrix Composites, Qiqihar University, Qiqihar, 161006 Heilongjiang, China

Correspondence should be addressed to Wang Ya-zhen; 1473278332@qq.com

Received 30 July 2019; Revised 21 October 2019; Accepted 25 November 2019; Published 18 December 2019

Guest Editor: Alessandro Dell'Era

Copyright © 2019 Wu Xue-ying et al. This is an open access article distributed under the Creative Commons Attribution License, which permits unrestricted use, distribution, and reproduction in any medium, provided the original work is properly cited.

Using carbon disulfide and 3-aminopropyltriethoxysilane as raw materials, a novel silane coupling agent with a terminal group was synthesized for the first time. The compound was synthesized in two steps in ethanol water solvent under the action of the catalyst triethylamine and a sulfhydryl-protecting agent. The product was characterized by FT-IR, ¹H NMR, and mass spectra to determine and prove its structure. The best experimental scheme was explored by a single factor experiment: a thiol-protecting agent selected iodomethane, the total reaction time was 2 hours, the two-step reaction temperature was 15°C and 10°C, respectively, and $n(\text{carbon disulfide}) : n(3 - \text{aminopropyl three ethoxysilane}) = 1.4 : 1$. Under these conditions, the product yield was up to 74.28%. Secondly, using the nonisothermal decomposition method, the thermal stability and thermal decomposition enthalpy of a thiohydrazide-iminopropyltriethoxysilane coupling agent were measured by a differential scanning calorimeter (DSC). Thereby, the thermal decomposition kinetic parameters and kinetic equations of the thiohydrazide-iminopropyltriethoxysilane coupling agent were derived.

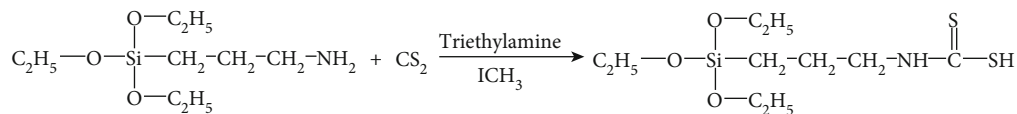
1. Introduction

The mercaptosilane coupling agent is a special kind of organosilicon compound [1]. The structural formula can be represented by $\text{OR}_3\text{-Si-Y-SH}$ [2], wherein Y represents normally a propyl group and Si-OR_3 represents a siloxy group such as a methoxy or ethoxy group. From this, it was shown that the mercaptosilane coupling agent contains both a carbon functional group reactive with an organic substance and a silicon functional group reactive with an inorganic substance. Due to this special molecular structure, a mercaptosilane coupling agent could be used as a “molecular bridge” [3] between an organic material and an inorganic material to prepare an organic polymer composite having excellent properties. Therefore, mercaptosilane coupling agents are widely used in batteries [4], coatings [5], pollution control [6], composite materials, and other fields.

The mercapto group was oxidized easily. In the presence of free radical-producing substances, sulfhydryl groups could form sulfur radicals through -S atom transfer and ini-

tiate monomer polymerization [7]. Therefore, sulfonium-containing silane coupling agents have attracted the interest of many researchers in the fields of biomedicine [8] and nanoscience [9]. Chen et al. [10] used the two-component initiating system of the mercapto group and benzoyl peroxide (BPO) to initiate the polymerization of HEMA grafted on SiO_2 to study the adsorption of quercetin by SiO_2 -g-PHEMA. Motevalizadeh et al. [11] used MPTMS to modify MNP, the mercapto group, and butylactam and formed a two-component initiating system to initiate the copolymerization of St and AL, and studied the rate of drug delivery control. Servant et al. [12] modified organoclay by MPTMS and initiated free radical polymerization on its surface to prepare polystyrene-organoclay composites.

However, in the process of silane coupling and modification of inorganic materials with polymers, many common silane coupling agents require the addition of an initiator to initiate the polymerization of the monomers. If the silane coupling agent has both a polymerization-initiating group and a functional group bonded to the



SCHEME 1: The preparation of thiohydrazide-iminopropyltriethoxysilane coupling agent.

inorganic nanoparticles, the silane coupling agent can initiate polymerization of the monomer while modifying the inorganic nanoparticles, thereby simplifying the reaction step [13].

Therefore, this paper is devoted to the synthesis of a silane coupling agent with both coupling and initiating functions. In this paper, a sulfonyl coupling with a thiol group was prepared by using carbon disulfide and 3-aminopropyltriethoxysilane as raw materials. The structure was confirmed and characterized by FT-IR, ^1H NMR, and mass spectra. Through DSC, the thermal decomposition kinetics of a thiohydrazide-iminopropyltriethoxysilane coupling agent was investigated, including thermal stability, decomposition constants (K_d), and activation energy (E_a), and then the equation of thermal decomposition kinetics was obtained.

2. Experimental

2.1. Materials. 3-Aminopropyltriethoxysilane (KH550), carbon disulfide, and triethylamine were purchased from Aladdin Industrial Corporation (Shanghai, China). Ethanol was purchased from Tianjin Fuyu Chemical Co. Ltd. (Tianjin, China). Methyl iodide was purchased from Shanghai Tanghao Chemical Technology Co. Ltd. (Shanghai, China). n-Hexane was purchased from Tianjin Kemiou Chemical Reagent Co. Ltd. (Tianjin, China). All of the chemicals were AR grade and were used as received without any purification. H_2O used for laboratory experiments was obtained after distillation.

2.2. Preparation of Thiohydrazide-Iminopropyltriethoxysilane Coupling Agent. KH550 (1 g), 5 ml ethanol aqueous solution (water : ethanol = 1 : 17), and 20 ml triethylamine were added into a three-neck flask, stirred at 10°C under a purified N_2 atmosphere. After 20 minutes, carbon disulfide (0.1 g) and methyl iodide (1 g) were added into the three-neck flask. The reaction was continued also at 10°C for several hours. The primary product was obtained by cooled to room temperature.

Finally, n-hexane was used to extract and wash the primary product, and then the final product was collected after drying in vacuum under 60°C for over 24 hours. The final product was a liquid. This part of the experiment process is shown in Scheme 1.

2.3. Characterization. The samples which were compressed with KBr were analyzed by an FT-IR spectrometer (Spectrum Two, PerkinElmer, USA) at room temperature, at a spectral range of $450\text{--}4000\text{ cm}^{-1}$, and at a spectral resolution of 4 cm^{-1} . A Bruker AV600 ^1H -NMR spectrometer (Bruker Technology Co., Ltd., Germany) was used to record the ^1H -NMR spectra. Mass spectra was recorded

using a mass spectrometer (Waters Xevo G2 QTof, Waters Corporation, USA).

5-10 mg sample was added into a crucible and protected by a high-purity N_2 atmosphere. The thermal stability and thermal decomposition dynamics of the product were measured using a DSC 204-F1 (NETZSCH, Germany), ranging from 20 to 350°C at a heating rate of 5°C min^{-1} . The isothermal thermodynamic method was used to obtain the relationship between heat flow and time under constant temperature. Thereby, the thermal decomposition kinetics of the thiohydrazide-iminopropyltriethoxysilane coupling agent was investigated, including thermal stability, decomposition constants (K_d), and activation energy (E_a), and then the equation of thermal decomposition kinetics was obtained [14].

3. Results and Discussion

3.1. Effects of Reaction Conditions on Product Yield

3.1.1. Selection of Mercapto Protective Agent. The sulfhydryl-protective agents mainly include methyl iodide and benzyl chloride [15]. Between them, methyl iodide can be reused. The price of methyl iodide is relatively high, but the actual reaction yield is high, and it can be industrially applied. Although benzyl chloride is inexpensive, according to the method described in the literature, it is necessary to carry out the reaction in a solution of tetrahydrofuran. It has been found that tetrahydrofuran cannot be miscible with the reaction raw materials required for the experiment, and the entire experiment cannot be carried out. Therefore, methyl iodide, a highly effective protective agent, is selected as a sulfhydryl-protective agent.

3.1.2. Effects of Reaction Temperature on Product Yield. According to the single-variable method, a chemical reaction is carried out under the same conditions in addition to reaction temperatures. As could be seen from Figure 1, the yield reaches the highest at 15°C when different reaction temperatures were increased. When the temperature exceeded 15°C , the rate of decrease in yield increased as the temperature increases. When the temperature was lower than 15°C , the radical substitution reaction in the system was inhibited and the product yield was affected. Since the hydrolysis of the alkoxy group attached to the silicon atom (Si-OR) of KH550 made it an unstable group, the silicon atom could be partially broken as the reaction temperature was increased, so that the product was reduced and the product yield was also lowered.

3.1.3. Effects of Reaction Time on Product Yield. Also according to the single-variable method, the chemical reaction was carried out under different reaction times. As could be seen from Figure 2, as the reaction time reached 2 hours, the product yield was the highest. As the reaction time exceeded 2

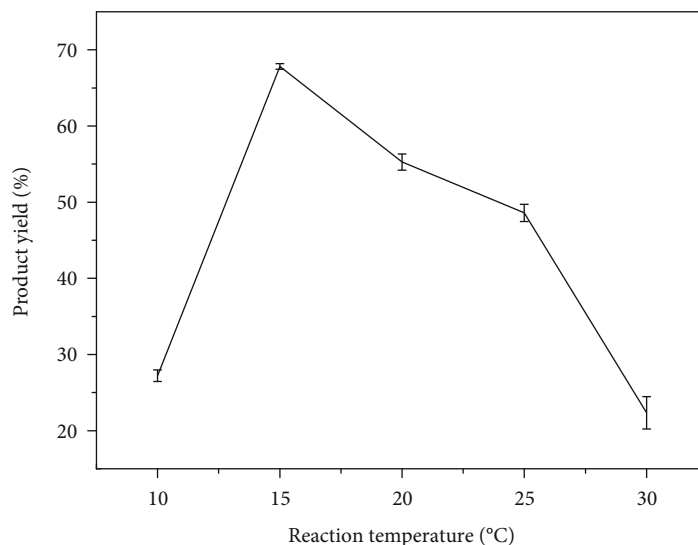


FIGURE 1: Effect of different reaction temperatures on yield.

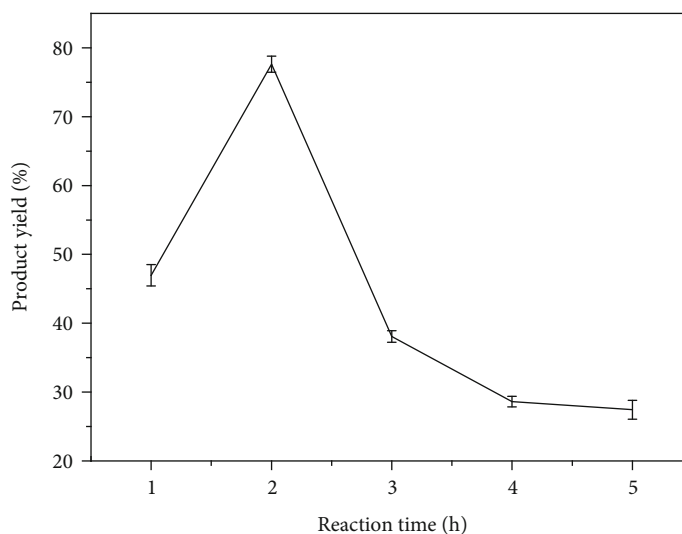


FIGURE 2: Effect of different reaction times on yield.

hours, the product yield also decreased. The radical replacement reaction was required to be carried out at a certain time, and an excessively long reaction time caused the bond between the mercapto group and the carbonyl group to be broken, resulting in the decomposition of the product, which greatly reduced the product yield.

3.1.4. Effects of Material Ratio on Product Yield. The chemical reaction was carried out under different material ratios, as could be seen from Figure 3.

3.2. Confirmation on the Chemical Structure of Thiohydrazide-Iminopropyltriethoxysilane Coupling Agent

3.2.1. ¹H-NMR Analysis. All the functional groups of the product were obtained by ¹H-NMR test, and the results are presented in Figure 4. ¹H NMR (600 MHz, DMSO, TMS): δ 1.10 (m, 9H, OCH₂CH₃), 3.43 (m, 6H, OCH₂CH₃), 0.60

(t, 2H, Si-CH₂CH₂CH₂), 1.62 (m, 2H, Si-CH₂CH₂CH₂), 2.78 (m, Si-CH₂CH₂CH₂), 8.70 (t, 1H, NH), and 9.60 (s, 1H, SH).

3.2.2. FT-IR Analysis. All the functional groups of the product were obtained by FT-IR test, and the results are presented in Figure 5. The peaks that could be seen at 2930 and 2886 cm⁻¹ are attributed to the stretching vibration of -CH₂-, the peak at 2586 cm⁻¹ is attributed to -SH, the peak at 1443 cm⁻¹ is attributed to the hydrocarbon bending vibration of -CH₃, the peak at 1390 cm⁻¹ is attributed to the stretching vibration of -C-C-, the peak at 1073 cm⁻¹ is attributed to the antisymmetric stretching vibration peak of C-H, the peak at 1067 cm⁻¹ is attributed to the stretching vibration peak of C=S, and the peak at 798 cm⁻¹ is attributed to the stretching vibration peak of Si-O-CH₃. From curve (a) and curve (b), the peaks at 2586 cm⁻¹ and 1067 cm⁻¹ were only attributed to curve (b). This indicated that

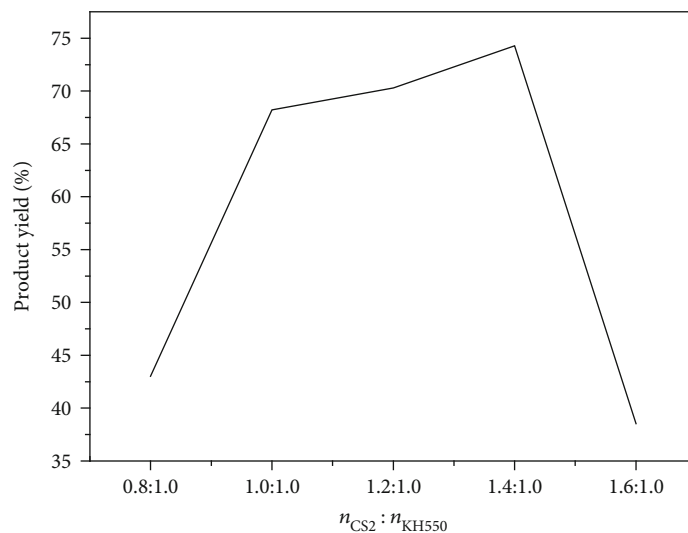


FIGURE 3: Effect of reaction raw material ratio on yield.

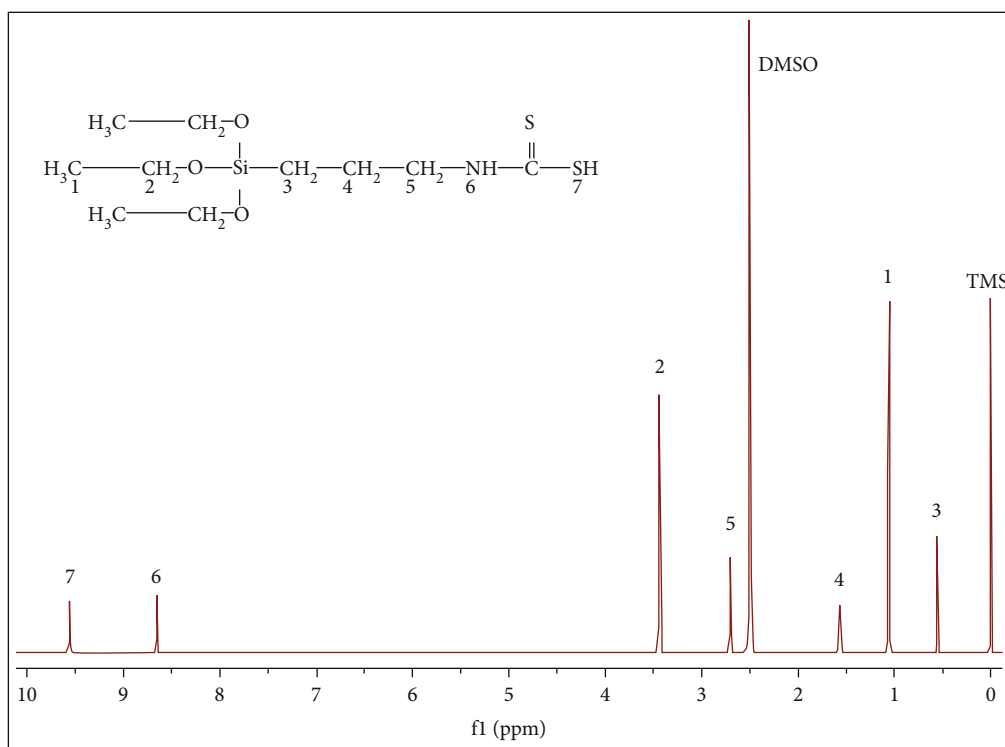


FIGURE 4: ¹H-NMR spectra of the thiohydrazide-iminopropyltriethoxysilane coupling agent.

the thiohydrazide-iminopropyltriethoxysilane coupling agent was successfully synthesized by carbon disulfide and 3-aminopropyltriethoxysilane in a radical substitution reaction.

In summary, a new reagent has been synthesized, and the structural formula is shown in Figure (6)

3.2.3. Mass Analysis. As shown in Figure 6, when the product was broken into pieces by the mass spectrometer, many molecular ion peaks appeared; however, there were stable and symmetrical structures, such as the imino group, the mercapto group, and the ethoxy group. The m/z of 320 was for the thiohydrazide-iminopropyltriethoxysilane coupling

agent. The results generated from the mass-to-charge ratio and possible fragments are shown in Table 1. The characteristic fragment that contained the ethoxy group was identified, which has an m/z of 163.

3.3. Isothermal Thermodynamic Analysis of Thiohydrazide-Iminopropyltriethoxysilane Coupling Agent

3.3.1. Thermal Stability. Figure 7 shows the nonisothermal decomposition curve of a thiohydrazide-iminopropyltriethoxysilane coupling agent. From Figure 7, since the product structure contains a mercapto group, the mercapto group

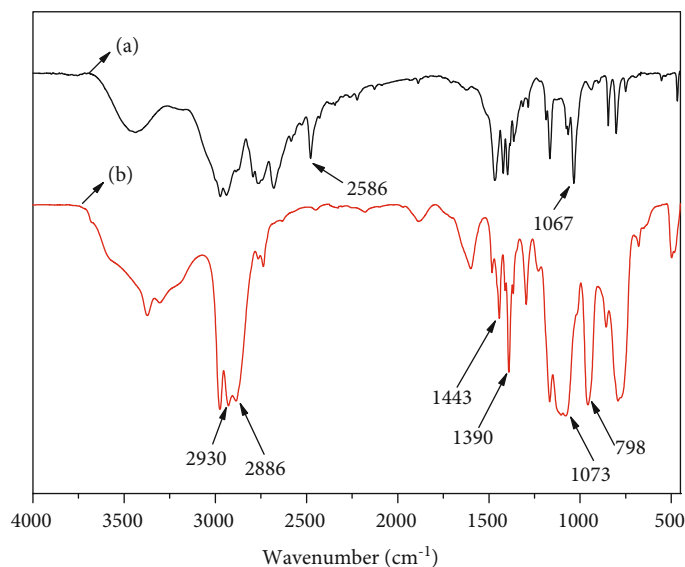


FIGURE 5: FT-IR spectra of products: (a) thiohydrazide-iminopropyltriethoxysilane coupling agent; (b) KH550.

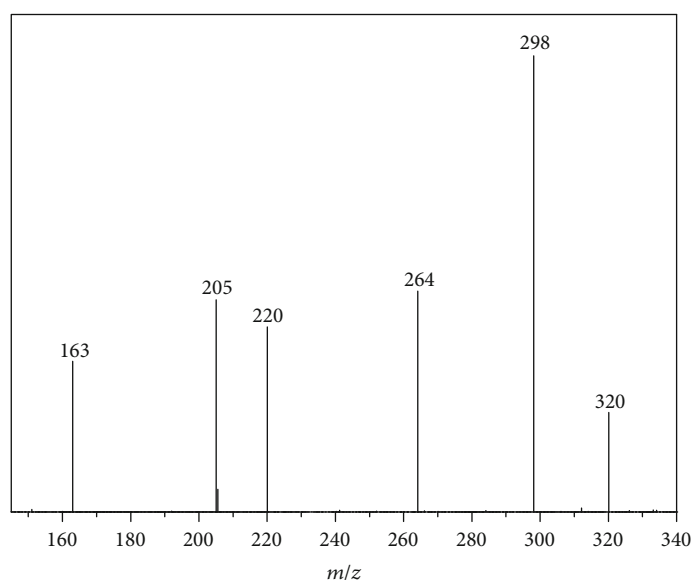


FIGURE 6: Mass spectrum of the product.

TABLE 1: The main fragment of the product analysis.

Mass-to-charge ratio	Possible fragments
163	$(OC_2H_5)_3Si+$
205	$(OC_2H_5)_3Si+C_3H_6$
220	$(OC_2H_5)_3Si+C_3H_6NH$
264	$(OC_2H_5)_3Si+C_3H_6NHSC$
298	$(OC_2H_5)_3Si+C_3H_6NHSCSH$

was thermally decomposed at a certain temperature to generate a radical which could initiate radical polymerization. The decomposition temperature and peak temperature are shown in Table 2. As could be seen from Table 2, the

thiohydrazide-iminopropyltriethoxysilane coupling agent was relatively stable before the temperature was 181.6°C, but as the temperature increases, a significant exothermal appeared. It was due to the decomposition of the thiol group. When the temperature reaches 183.7°C, the thermal decomposition of the thiol group reaches the maximum extent, and the decomposition rate was the fastest at this time. When the temperature continues to rise, the DSC curve could see that its enthalpy value begins to decrease, the thiol group contained in the product gradually decomposes completely, and the heat was in a lost state. Because the temperature was too high, the thiohydrazide-iminopropyltriethoxysilane coupling agent was completely decomposed, so a temperature that was too high was not

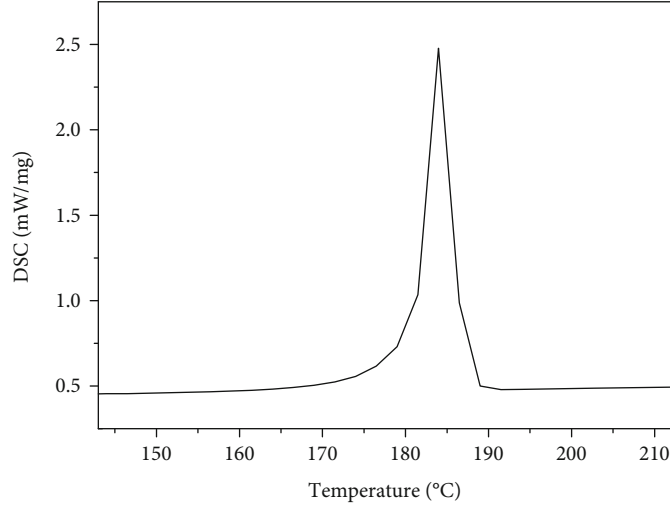


FIGURE 7: Thermal decomposition curve of the thiohydrazide-iminopropyltriethoxysilane coupling agent.

TABLE 2: Thermal decomposition temperature and peak temperature of the thiohydrazide-iminopropyltriethoxysilane coupling agent.

	Decomposition temperature (°C)	Peak temperature (°C)
Thiohydrazide- iminopropyltriethoxysilane coupling agent	181.6	183.7

meaningful for us to study its thermodynamic properties. When the temperature reaches 181.6°C, the heat provided by the entire environment was sufficient for the thiohydrazide-iminopropyltriethoxysilane coupling agent to react rapidly. Therefore, the product was a sulfhydryl-based initiator having thermal initiation properties.

3.3.2. Isothermal Decomposition Kinetic Analysis of Thiohydrazide-Iminopropyltriethoxysilane Coupling Agent. The decomposition rate constant of the reaction product during thermal decomposition is an important parameter for measuring the reaction rate, which can be obtained by changing the concentration of the reactant with time. By calculating the decomposition rate constant, the amount of change in the concentration of the reactant can be obtained, and further, the relative data such as the half-life of the reactant can be obtained by calculation.

(1) *Decomposition Constant (K_d)*. Based on the isothermal decomposing data, K_d could be calculated through the ΔH of decomposition [16]. The reaction is a first-order reaction expressed as follows:

$$R_d = \frac{-dC}{dt}. \quad (1)$$

In the DSC isothermal decomposition mode [17], the change in reactant concentration was unknown and the conversion calculation was performed using thermal enthalpy:

$$\frac{-dC}{dt} = \frac{d\Delta H \cdot C_0}{\Delta H_0 \cdot dt}, \quad (2)$$

$$dC = \frac{d\Delta H \cdot C_0}{\Delta H_0}, \quad (3)$$

$$\frac{C_0}{C} = \frac{\Delta H_0}{\Delta H_0 - \Delta H_{re}}, \quad (4)$$

$$\ln \frac{C_0}{C} = K_d \cdot t. \quad (5)$$

Combining equation (5) with the decomposition equation (4), a new equation (equation (6)) was developed as follows:

$$\ln \frac{\Delta H_0}{\Delta H_0 - \Delta H_{re}} = K_d \cdot t. \quad (6)$$

The half-life and reaction activation energy [18] were determined by a DSC isothermal decomposition mode. It could be seen from Figure 8 that the decomposition rate was the fastest at the initial stage of the isothermal reaction, the heat release was rapidly increased, and then the heat release tended to be stable. At different temperatures, the thiohydrazide-iminopropyltriethoxysilane coupling agent is decomposed for 10 min, 30 min, and 40 min, and the corresponding ΔH is shown in Table 3.

As in equation (6), the data of Table 3 was substituted into this equation. The thermal decomposition rate constant of the thiohydrazide-iminopropyltriethoxysilane coupling agent at different temperatures and different times, respectively, is shown in Table 4.

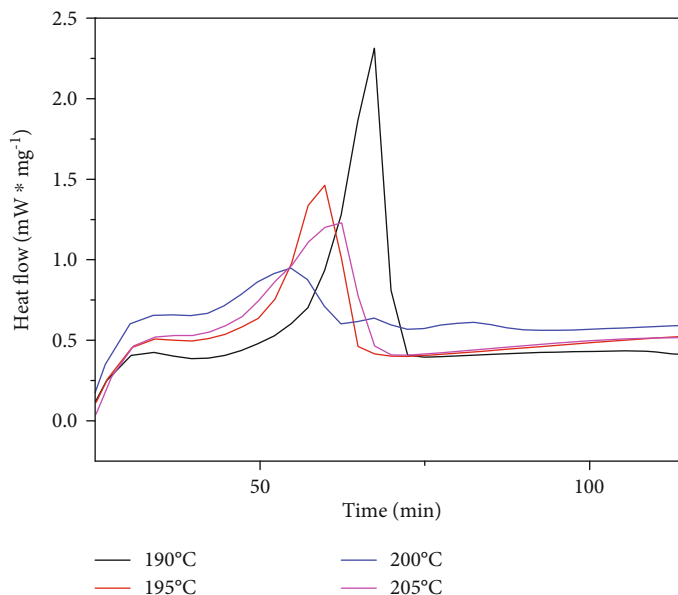


FIGURE 8: Isothermal decomposition curves of products at different temperatures.

TABLE 3: Isothermal decomposition kinetics DSC data of the thiohydrazide-iminopropyltriethoxysilane coupling agent.

	ΔH_0	ΔH_{10} (10 min)	ΔH_{30} (30 min)	ΔH_{40} (40 min)
190°C	290.9 J/g	37.6 J/g	104.6 J/g	135.9 J/g
195°C	299.9 J/g	38.4 J/g	107.1 J/g	139.3 J/g
200°C	315.7 J/g	45.8 J/g	136.3 J/g	173.9 J/g
205°C	327.0 J/g	75.0 J/g	213.9 J/g	281.6 J/g

TABLE 4: The thermal decomposition rate constant of the product at different temperatures.

	$\Delta K_{d10 \text{ min}}$	$\Delta K_{d30 \text{ min}}$	$\Delta K_{d40 \text{ min}}$	Average K_d
190°C	0.0138	0.0149	0.0157	0.0148
195°C	0.0137	0.0147	0.0156	0.0147
200°C	0.0157	0.0188	0.0200	0.0182
205°C	0.0260	0.0353	0.0494	0.0369

The Arrhenius equation equation (7) is as follows:

$$\ln K_d = -\frac{E_d}{RT} + \ln A_d. \quad (7)$$

By plotting $1/T$ and $\ln K_d$, as shown in Figure 9, it could be seen that these points were discrete, and the applied Arrhenius empirical formula is a linear function, so these data points are idealized by linear regression [19].

(2) *Linear Equation Fitting*. In the obtained equation, the intercept [20] represents the logarithm value $\ln A_d$ of the pre-factor in the Arrhenius empirical formula, and the slope represents the negative ratio of the decomposition activation

energy to the gas molar constant $-E_d/R$ in the Arrhenius empirical formula. Therefore, the activation energy of the decomposition reaction is $E_d = 108.155$ kJ/mol, and the preexponential factor is $A_d = 4.773 \times 10^8$. The thermal decomposition kinetic equation of the final thiohydrazide-iminopropyltriethoxysilane coupling agent is as follows:

$$\ln K_d = \frac{-108.155}{RT} + \ln (1.998 \times 10^{10}). \quad (8)$$

4. Conclusion

The thiohydrazide-iminopropyltriethoxysilane coupling agent was synthesized by using carbon disulfide and KH550. The optimal scheme was obtained by a single-factor experiment: the sulfhydryl-protecting agent was methyl iodide, the reaction time was 2 hours, the reaction temperature was 15°C, and $n(\text{carbon disulfide}) : n(\text{KH550}) = 1 : 1$. Under these conditions, the product yield was up to 74.28%. The product was characterized by infrared absorption spectroscopy, ^1H NMR nuclear magnetic resonance spectroscopy, and mass spectrometry. The product was identified as a novel silane coupling agent with the mercapto group.

The thermal decomposition kinetics of the thiohydrazide-iminopropyltriethoxysilane coupling agent was investigated. The thermal stability and thermodynamic parameters were analyzed and calculated by the isothermal decomposition mode. It was found that the decomposition temperature of the thiohydrazide-iminopropyltriethoxysilane coupling agent was between 181.6°C and 187.2°C. Combining the first-order reaction equation and the thermodynamic kinetic equation, the data of the thiohydrazide-iminopropyltriethoxysilane coupling agent under a constant temperature were analyzed, and the calculated decomposition rate constant and temperature value were calculated by the linear fitting method. The decomposition reaction was activated with $E_d = 108.155$

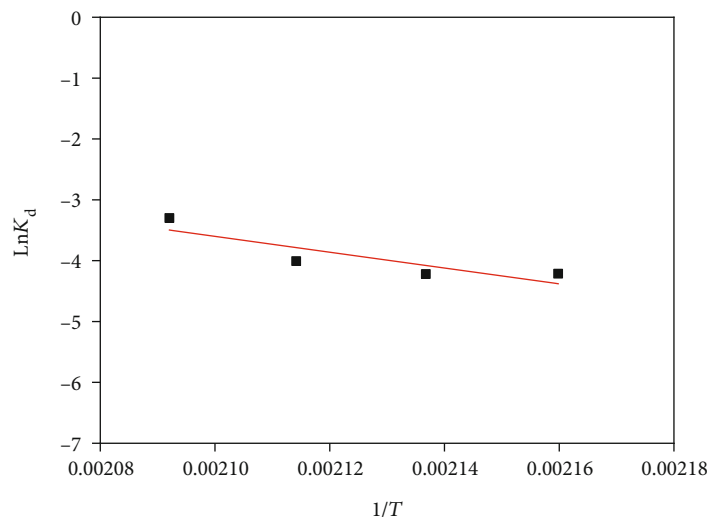


FIGURE 9: Arrhenius equation curve for thermal decomposition data of the thiohydrazide-iminopropyltriethoxysilane coupling agent.

kJ/mol, and the preexponential factor was $A_d = 1.998 \times 10^{10}$. The thermal decomposition kinetic equation of the thiohydrazide-iminopropyltriethoxysilane coupling agent was $\ln K_d = -108.155/RT + \ln (1.998 \times 10^{10})$.

4.1. The Potential of Thiohydrazide-Iminopropyltriethoxysilane Coupling Agent. We named the thiohydrazide-iminopropyltriethoxysilane coupling agent as TIPTS. Modification of Fe_3O_4 nanoparticles by TIPTS obtained Fe_3O_4 -TIPTS. Among fixed-point modifying groups, the site-nucleophilic activity of the thiol group had higher activity than the carboxyl group, the hydroxyl group, the disulfide bond, and so on. Moreover, when Fe_3O_4 nanoparticles were modified by a fixed-point modifying group for the carboxyl group and the hydroxyl group, the disulfide bond could destroy site-nucleophilic activity and the thiol group could retain the site-nucleophilic activity. Then, grafting Fe_3O_4 -TIPTS by polyether-imide (PEI) and polyethylene glycol (PEG) obtained Fe_3O_4 -TIPTS-g-(PEI-co-PEG). Inside, magnetic nanoparticles (MNPs) were used as magnetically responsive carriers, PEG was the surface-modifying agent, and PEI was the drug-loading site with which primary amine reacts with doxorubicin (DOX). Targeting nanoparticles were quite stable in various physiological solutions and exhibited a pH-sensitive property in drug release. Therefore, Fe_3O_4 -TIPTS-g-(PEI-co-PEG) is a promising nanocarrier for targeting tumor therapy in vivo.

Data Availability

The data used to support the findings of this study are available from the corresponding author upon request.

Conflicts of Interest

No potential conflict of interest was reported by the authors.

Acknowledgments

This work was financially supported by the National Natural Science Foundation of China (grant number: 21376127) and the Scientific Research Projects Foundation of the Education Department of Heilongjiang Province (grant number: YSTSXX201860).



References

- [1] Z. Xianliang, T. Hongding, and J. Liao, *Principle, Synthesis and Application of Silane Coupling Agent*, Chemical Industry Press, 2012.
- [2] T. Shengnian and L. Xing, "Surface modification of SiC powder with silane coupling agent," *Journal of the Chinese Ceramic Society*, vol. 3, 2011.
- [3] L. Chen, Y. Wang, Zia-ud-Din et al., "Enhancing the performance of starch-based wood adhesive by silane coupling agent (KH570)," *International Journal of Biological Macromolecules*, vol. 104, Part A, pp. 137–144, 2017.
- [4] L. Zhu, T. J. Zimudzi, N. Li, J. Pan, B. Lin, and M. A. Hickner, "Crosslinking of comb-shaped polymer anion exchange membranes via thiol-ene click chemistry," *Polymer Chemistry*, vol. 7, no. 14, pp. 2464–2475, 2016.
- [5] C. Resetco, B. Hendriks, N. Badi, and F. du Prez, "Thiol-ene chemistry for polymer coatings and surface modification—building in sustainability and performance," *Materials Horizons*, vol. 4, no. 6, pp. 1041–1053, 2017.
- [6] K. Jainae, N. Sukpirom, S. Fuangswasdi, and F. Unob, "Adsorption of Hg(II) from aqueous solutions by thiol-functionalized polymer-coated magnetic particles," *Journal of Industrial and Engineering Chemistry*, vol. 23, pp. 273–278, 2015.
- [7] H. Xu, H. C. Yang, L. Zhang, Y. Chen, Q. T. Ni, and F. H. Gong, "Preparation of attapulgite/polystyrene hybrid particles by thiol-lactam initiated living radical graft polymerization," *Journal of Polymer Science*, vol. 4, pp. 437–443, 2015.
- [8] Y. Hao, H. Shih, Z. Muñoz, A. Kemp, and C.-C. Lin, "Visible light cured thiol-vinyl hydrogels with tunable degradation for

- 3D cell culture,” *Acta Biomaterialia*, vol. 10, no. 1, pp. 104–114, 2014.
- [9] L. G. Bach, M. R. Islam, Y. S. Gal, and K. T. Lim, “Synthesis and characterization of TiO₂/poly(methyl methacrylate) nanocomposites via surface thiol-lactam initiated radical polymerization,” *Journal of Nanoscience and Nanotechnology*, vol. 12, no. 7, pp. 5976–5980, 2012.
- [10] C. Lulu, M. Jian, L. Yanbin, and L. Baojiao, “Preparation of grafted microparticles PHEMA-SiO₂ by surface-initiated graft polymerization in nonaqueous media and its hydrogen bonding properties to quercetin,” *Journal of Functional Polymers*, vol. 28, no. 3, pp. 272–280, 2015.
- [11] S. F. Motevalizadeh, M. Khoobi, N. Babanejad et al., “Novel pH-responsive multilayer magnetic nanoparticles for controlled drug delivery,” *Journal of the Iranian Chemical Society*, vol. 13, no. 9, pp. 1653–1666, 2016.
- [12] L. A. Survant, M. Andrejevic, J. Picker, J. van den Hoek, E. Fossum, and I. Lagadic, “Surface-initiated polymerization of styrene from one-step prepared thiol-functionalized organoclays,” *Polyhedron*, vol. 114, pp. 37–41, 2016.
- [13] M. Liqun, H. Zijian, S. Zhaoyang, C. Haiyang, C. Guoli, and W. Yazhen, “Preparation and characterization of γ -tert-butyl peroxide propyltrimethoxysilane,” *Chemical Progress*, vol. 34, no. 12, pp. 4320–4323, 2015.
- [14] N. Zheng, L. Bo, C. Hu et al., “Synthesis and optimization of 1-hydroxyethyl-5-mercapto-1H-tetrazole,” *Journal of Nanchang University (Natural Science)*, vol. 40, no. 6, pp. 575–579, 2016.
- [15] V. S. D. Carvalho and K. Tannous, “Thermal decomposition kinetics modeling of energy cane *Saccharum robustum*,” *Thermochimica Acta*, vol. 657, pp. 56–65, 2017.
- [16] M. Yu and W. Quanzhong, “Improvement on chemical reaction rate and activation energy reaction conditions and miniaturization experiment,” *Shandong Industrial Technology*, vol. 5, no. 2, pp. 5 and 40, 2017.
- [17] Q. Zhenhua, W. Benmei, C. Qunpeng, and L. Jianfen, “Discussion of data processing in determination of chemical reaction rate and activation energy,” *Guangdong Chemical Industry*, vol. 22, no. 44, pp. 154–155, 2017.
- [18] J. Lyu, D. Hu, T. Liu, and L. Zhao, “Non-isothermal kinetics of epoxy resin curing reaction under compressed CO₂,” *Journal of Thermal Analysis and Calorimetry*, vol. 131, no. 2, pp. 1499–1507, 2018.
- [19] M. I. Khan, S. Qayyum, T. Hayat, M. Waqas, M. I. Khan, and A. Alsaedi, “Entropy generation minimization and binary chemical reaction with Arrhenius activation energy in MHD radiative flow of nanomaterial,” *Journal of Molecular Liquids*, vol. 259, pp. 274–283, 2018.
- [20] S. Lesz, P. Kwapuliński, M. Nabiałek, P. Zackiewicz, and L. Hawelek, “Thermal stability, crystallization and magnetic properties of Fe-Co-based metallic glasses,” *Journal of Thermal Analysis and Calorimetry*, vol. 125, no. 3, pp. 1143–1149, 2016.

Research Article

Ohmic Contact Mechanism for Ni/C-Faced 4H-n-SiC Substrate

Seongjun Kim,¹ Hong-Ki Kim,¹ Minwho Lim,² Seonghoon Jeong,³ Min-Jae Kang,¹ Min-Sik Kang,¹ Nam-Suk Lee,¹ Tran Viet Cuong ,⁴ Hyunsoo Kim,³ Tobias Erlbacher,² Anton Bauer,² and Hoon-Kyu Shin ¹

¹National Institute for Nanomaterials Technology, Pohang University of Science and Technology, Cheongam-Ro 77, 37673 Pohang, Republic of Korea

²Fraunhofer Institute for Integrated Systems and Device Technology, Schottkystrasse 10, 91058 Erlangen, Germany

³Department of Semiconductor and Chemical Engineering, Chonbuk National University, Baekje-daero 567, 54896 Jeonju, Republic of Korea

⁴NTT Hi-Tech Institute, Nguyen Tat Thanh University, A Nguyen Tat Thanh Street, 298-300 Ho Chi Minh City, Vietnam

Correspondence should be addressed to Hoon-Kyu Shin; shinhk@postech.ac.kr

Received 17 July 2019; Revised 11 October 2019; Accepted 17 October 2019; Published 5 December 2019

Guest Editor: Francesca A. Scaramuzzo

Copyright © 2019 Seongjun Kim et al. This is an open access article distributed under the Creative Commons Attribution License, which permits unrestricted use, distribution, and reproduction in any medium, provided the original work is properly cited.

In this work, the ohmic contact mechanism of Ni electrodes on C-faced 4H-n-SiC was investigated by evaluating the electrical and microstructural properties in the contact interface as a function of annealing temperatures ranging from 950 to 1100°C. We determined that Ni-silicide, especially the NiSi phase, plays a key role in the formation of ohmic contacts rather than an increase in carbon vacancies in the C-faced SiC substrate. A vertically oriented NiSi phase was observed in the thermally annealed sample at the optimized temperature that behaves as a current path. A further increase in annealing temperature leads to the degradation of ohmic behavior due to the formation of horizontal-type NiSi in the Ni-rich Ni-silicide/NiSi/SiC structure.

1. Introduction

Many technical challenges need to be overcome to improve the performance of 4H-SiC-based power devices, such as Schottky barrier diodes (SBDs) and metal-oxide-semiconductor field-effect transistors (MOSFETs). One of them is the reproducible formation of low resistance ohmic contacts. Nickel metallization, which has the lowest specific contact resistance (ρ_{sc}), has been frequently used for this purpose [1–8]. For example, ρ_{sc} on Ni contacts to Si-faced 4H-n-SiC epitaxial layer is between 2.8×10^{-3} and $1.1 \times 10^{-6} \Omega\text{-cm}^2$ under the high temperature annealing at $\sim 1000^\circ\text{C}$, depending on the process technique and doping concentration [2, 6–8]. The thermal annealing at high temperature, however, can damage the oxide and SiC/SiO₂ interface, which is undesirable for device fabrication. In that sense, Ni-based metal structures have been also studied in order to form the low resistance ohmic contact even under the low temperature annealing process. With low annealing temperature at 750°C or 950°C, the ohmic contacts have low ρ_{sc}

values, respectively, of 8×10^{-4} and $4.2 \times 10^{-5} \Omega\text{-cm}^2$ and were achieved by using Ni/Ti/Al and Ni/Ti/Al/W metal schemes [9, 10].

The development of ohmic contact can be possible based on the sufficient understanding of the formation mechanisms of Ni contact on Si-faced 4H-n-SiC. In the case of Si-faced 4H-n-SiC, carbon accumulation at the interface and donor-like carbon vacancies (V_C) that can lower the barrier height (Φ_B) and reduce ρ_{sc} have been suggested as a possible mechanism for ohmic contact formation [2–5]. In addition, the formation of Ni-silicide by thermal treatment may play a predominant role in the formation of ohmic contacts [5–8]. Indeed, it is highly desirable to optimize the ohmic contact on the SiC substrate, particularly on C-faced 4H-SiC for vertical device structures. However, the mechanism for ohmic contact formation in C-faced 4H-n-SiC has not yet been completely elucidated.

In this study, we investigated the ohmic contact mechanism on Ni/4H-n-SiC substrate (C-faced) interfaces. The electrical properties of contacts were evaluated using the

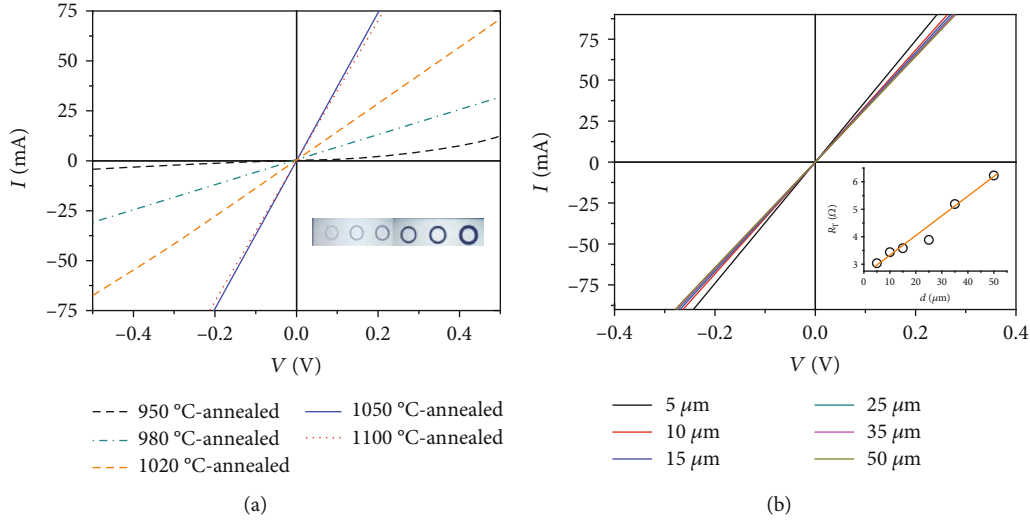


FIGURE 1: (a) I - V characteristics of Ni/n-SiC substrate contacts as a function of annealing temperature ($d = 5 \mu\text{m}$). (b) I - V curves of 1050°C-annealed sample as a function of d . The inset shows the total resistance $R_T - d$ plot.

transmission line model (TLM). The formation and degradation mechanisms of ohmic contacts with the annealing process were investigated by current-voltage-temperature (I - V - T) measurements, scanning transmission electron microscopy (STEM), and energy-dispersive X-ray spectroscopy (EDS).

2. Experimental Methods

For this study, we use commercially available 4° off-axis n-type 4H-SiC substrates with a resistivity of $0.02 \Omega\text{-cm}$ from Cree, USA. Hall-effect measurements were performed for five SiC substrate samples using the van der Pauw method and yielded an average electron carrier concentration (N) of $3.28 \times 10^{18} \pm 6.14 \times 10^{14} \text{ cm}^{-3}$ and a Hall mobility (μ) of $90.8 \pm 0.12 \text{ cm}^2/\text{V}\cdot\text{s}$. Prior to metal deposition, the samples were cleaned with $\text{H}_2\text{SO}_4:\text{H}_2\text{O}_2 = 3:1$, $\text{NH}_4\text{OH}:\text{H}_2\text{O}_2:\text{H}_2\text{O} = 1:1:5$, and buffered oxide etchant solutions for 10, 10, and 1 min, respectively.

To investigate the ohmic contacts on C-faced 4H-SiC, namely, the backside of the SiC substrate, TLM patterns with circular geometry (diameter of the inner circle was $200 \mu\text{m}$, and the distance between inner and outer circles was $d = 5, 10, 15, 25, 35,$ and $50 \mu\text{m}$) were defined using photolithography, as shown in the inset of Figure 1(a). As a contact metal, 150 nm thick Ni was deposited on the patterned SiC substrate using an e -beam evaporator. After the lift-off process, rapid-thermal annealing (RTA) was performed at 950, 980, 1020, 1050, and 1100°C for 1 min in N_2 ambient in order to stimulate a reaction between Ni and the 4H-SiC substrate. All electrical characteristics of the contacts were evaluated in a vacuum chamber (<0.02 Torr) equipped with a variable-temperature chuck system using a parameter analyzer (HP 4156A). I - V - T measurements were performed to characterize the contact properties in the temperature range of 300–420 K. STEM and EDS were also performed to investigate the structural properties of the contacts using a JEOL JEM-2100F.

3. Results and Discussion

Figure 1(a) shows the I - V characteristics of Ni contacted to the bottom of the n-type SiC substrate as a function of annealing temperature. The current and voltage were measured from adjacent TLM pads with a d of $5 \mu\text{m}$. It is shown that the I - V curves are significantly dependent on the annealing temperature. For example, the I - V curve of the 950°C-annealed sample exhibited a rectifying characteristic; however, the I - V curves of samples annealed at temperatures equal to and higher than 980°C were linear indicating the formation of ohmic contacts. Using the TLM method [11], the 1050°C-annealed sample was computed to have the lowest ρ_{sc} ($5.67 \times 10^{-4} \Omega\text{-cm}^2$) and sheet resistance (R_{sh}) of $13.6 \Omega/\text{sq}$ (Figure 1(b)). Note that ρ_{sc} for 1020°C-annealed sample ($9.63 \times 10^{-4} \Omega\text{-cm}^2$) is higher than that of the 1050°C-annealed sample, and the reliable contact parameters for 980°C-annealed sample could not be obtained due to the nonlinear relation between the total resistance (R_T) and d (not shown here). Thus, 1050°C was determined as the most optimized annealing temperature. One interesting result was that thermal annealing at only 1100°C led to a decrease in current values at the relevant voltages and an increase in ρ_{sc} ($8.0 \times 10^{-4} \Omega\text{-cm}^2$). A possible explanation for degradation of electrical properties is discussed in more detail in the last section.

Prior to this work, it was unclear whether the Ni-silicide formed at the contact interface or the out-diffusion of C atoms played a key role in the formation of ohmic contacts when Ni was deposited as an ohmic metal on n-type SiC [2–8]. According to previous studies [2–5], the out-diffusion of carbon leads to V_C , which acts as a donor, causing an increase of N underneath the contact interface. Therefore, if an out-diffusion of carbon was critical to the formation of ohmic contacts, both the increase of N and decrease of Φ_B should be observed simultaneously [2]. To investigate if the origin of ohmic contact formation was

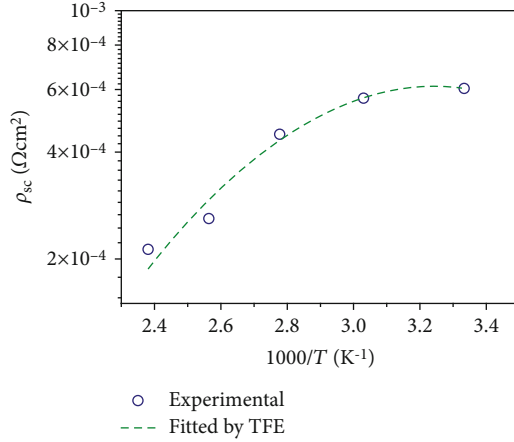


FIGURE 2: ρ_{sc} vs. $1000/T$ plot for a 1050°C-annealed sample.

dominated by the increase of N due to an out-diffusion of carbon atoms in the contact interface on C-faced 4H-n-SiC, ρ_{sc} values for the 1050°C-annealed sample were plotted as a function of annealing temperature (Figure 2). The thermionic field emission (TFE) model [11] was used to calculate ρ_{sc} since the N value predicts that the TFE model would provide a good approximation, i.e., TFE dominates when $0.5 < E_{00}/kT < 5$. Here, E_{00} is given by $E_{00} = (qh/4\pi)(N/\epsilon_s m^*)^{1/2}$, where m^* is the electron effective mass ($m^* = 0.36m_e$) and ϵ_s is the dielectric constant of 4H-SiC ($\epsilon_s = 9.66$) [5]. With $N = 3.28 \times 10^{18} \text{ cm}^{-3}$ and $T = 300 \text{ K}$, the calculation shows that E_{00}/kT was as low as 0.695 which lies in the TFE regime [11]. ρ_{sc} was calculated using

$$\rho_{sc} = \frac{\coth^{1/2}(E_{00}/kT) \cosh(E_{00}/kT)}{(qA^{**}/k^2)} \exp\left(\frac{q(\Phi_B + V_n)}{E_{00} \coth(E_{00}/kT)} - \frac{qV_n}{kT}\right), \quad (1)$$

where A^{**} is the Richardson constant ($146 \text{ A/cm}^2 \text{ K}^2$) [5] and V_n is the energy difference between the conduction band edge (E_c) and the Fermi level (E_F). From the successful theoretical fit of experimental data using Equation (1) as shown in the broken line of Figure 2, Φ_B of 0.62 eV, E_{00} of 0.019 eV, and N of $3.7 \times 10^{18} \text{ cm}^{-3}$ were obtained. Note that Φ_B was lower than the theoretically expected value ($\Phi_B = \Phi_{Ni} (5.15 \text{ eV}) - \chi_{4H-SiC} (3.6 \text{ eV}) = 1.55 \text{ eV}$) [12], whereas N evaluated by the TFE model was nearly constant compared to the value determined by Hall-effect measurement. Therefore, the above results suggest that a more dominant factor other than the generation of V_C should be used to explain the formation of an ohmic contact at the Ni/C-faced 4H-n-SiC interface.

According to the literature [2–8], various Ni-silicide phases are formed at the interface of the Ni-based contacts on 4H-n-SiC during thermal annealing. For example, Ni-rich regions, typically comprised of $Ni_{31}Si_{12}$ and Ni_2Si phases, are formed under a low annealing temperature of 600°C. The $Ni_{31}Si_{12}$ hexagonal phase, which is mainly formed at a considerably low temperature, has little effect

on the reduction of ρ_{sc} [5, 8]. As the annealing temperature is increased ($> \sim 900^\circ\text{C}$), the Ni-silicide phases recrystallize at the contact interfaces, i.e., a full transformation of $Ni_{31}Si_{12}$ into the Ni_2Si orthorhombic phase [3, 8]. Several studies have shown that this Ni_2Si phase plays a key role in determining the electrical transport characteristics at the contact interfaces, namely, the recrystallization into the Ni_2Si phase leads to a reduction of ρ_{sc} and a decrease in Φ_B [6, 8]. If this model is valid, both the uniform distribution of Ni and Si atoms at metallic regions and the linear increase of current with applied bias should be observed for the sample annealed at 950°C.

To investigate the predominant ohmic mechanism in terms of structural changes, STEM and EDS measurements were performed. Figure 3 shows the STEM images and the corresponding EDS elemental mapping for the samples annealed at 950, 1050, and 1100°C. The interface between the SiC substrate and contact metal is clearly distinguishable in the 950°C-annealed sample (Figure 3(a)). Figures 3(c) and 3(d) show that Si and C atoms out-diffused toward the contact metal region and were evenly distributed, indicating a transformation into the single Ni-silicide phase, which was expected to be Ni_2Si . However, the $I-V$ curve of the 950°C-annealed sample was strongly rectifying as shown in Figure 1(a). Therefore, we can conclude that the formation of Ni-rich Ni-silicide (NNS), especially Ni_2Si , is not the major factor in forming ohmic contacts on C-faced n-SiC. Indeed, this result is supported by Han et al. who reported that the Φ_B of Ni-silicide, comprised of Ni_2Si , is higher than Ni metal on n-type SiC [2]. Interestingly, the distinct difference between the 950°C-annealed sample and the samples with higher annealing temperatures was observed in elemental mapping images. As indicated by the superimposed white lines in Figures 3(h) and 3(l) directed by white arrows, a C-rich region was formed after thermal annealing at 1050°C or more, in which the composition of Ni-silicide in this C-rich region corresponds to NiSi [2, 7]. From a thermodynamic point of view, the formation of NiSi is valid since the difference in Gibbs free energy for NiSi at 950°C is negative ($\Delta G_{950^\circ\text{C}} = -34.4 \text{ kJ/mol}$) [7, 13]. Moreover, according to previous research, the formation of the NiSi/SiC system contributes to the significant reduction in contact resistance. Considering our and previous results mentioned above, it is likely that the formation of ohmic contacts is also related to the formation of NiSi phases rather than Ni_2Si even in the case of C-faced SiC. Thus, an ohmic contact for the Ni metallization on C-faced 4H-n-SiC can be achieved by the formation of C-rich areas corresponding to the NiSi phase.

It is also necessary to investigate why the ohmic properties degraded with annealing beyond the optimized temperature. One possible factor that increases ρ_{sc} value might be the change of the C-rich region thickness. However, the thickness of C-rich region varies between 20 and 36 nm as shown in Figures 3(h) and 3(l). Therefore, the electrical properties at the contact interface have little to no correlation with the thickness of the C-rich region. Another possible explanation for ohmic contact degradation is the structural change in the C-rich area. Indeed, ohmic behavior was observed in both the 1050°C- and 1100°C-annealed samples. Although C-rich

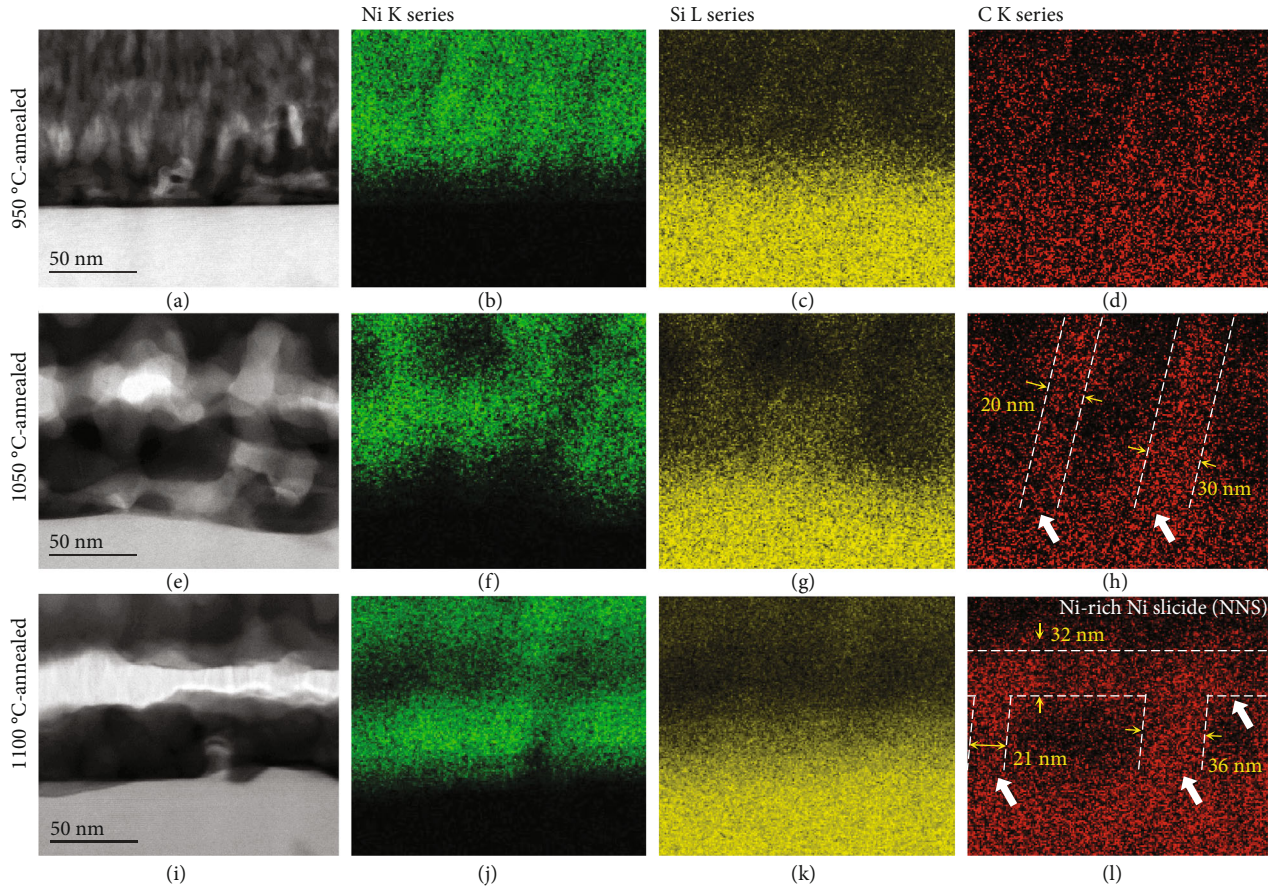


FIGURE 3: STEM and EDS elemental mapping images for (a–d) 950°C-annealed, (e–h) 1050°C-annealed, and (i–l) 1100°C-annealed sample, respectively.

regions were observed in both samples, the corresponding structures were clearly formed with different shapes. For example, for samples annealed at 1050°C, the C-rich region was formed vertically (Figure 3(h)), indicating that the current path with low resistance between the SiC and the top electrode was well formed. When the annealing temperature was increased by 50°C, i.e., in the case of 1100°C-annealed sample, C-rich areas were formed horizontally as well as vertically, as shown in Figure 3(l). In addition, NNS was formed just above the horizontal C-rich region, i.e., a Ni_2Si or a $\text{Ni}_{31}\text{Si}_{12}$ /NiSi/SiC structure was formed. As mentioned before, the formation of NiSi/SiC structures has the effect of reducing ρ_{sc} , compared with the NNS/SiC system [2, 7]. On the other hand, the formation of NNS/NiSi contacts could negatively affect the current flow. Due to the work function of NiSi (~4.5 eV) and NNS (~4.8 eV) [14], there is a contact potential difference ($q\Delta V = \Phi_{\text{NNS}} - \Phi_{\text{NiSi}}$) of 0.3 eV between the NNS/NiSi structure. Therefore, to produce the same current value for the NNS/NiSi/SiC and NiSi/SiC structures, an additional voltage of 0.3 V should be applied to the former structure. Eventually, the increase in ρ_{sc} of the contact annealed above the optimized temperature was due to the horizontal formation of the C-rich region causing the NNS/NiSi/4H-n-SiC structure. Indeed, it is evident that the formation of the horizontal C-rich area restricts current flow

although the exact origin of ohmic contact degradation on Ni/C-faced 4H-n-SiC should be further investigated.

4. Conclusions

The ohmic contact mechanism of Ni contact to C-face and n-type 4H-SiC can be characterized as follows:

- (1) The carrier concentrations extracted from Hall-effect and $I - V - T$ measurements for the sample annealed at optimized conditions (1050°C) are nearly constant. This proves that V_{C} , acting as donors, have little contribution to the formation of ohmic contacts
- (2) The evidence for the formation of various Ni-silicide phases after thermal annealing was confirmed from EDS elemental mapping. It was shown that the C-rich area corresponding to the NiSi phase plays a key role in the formation of ohmic contacts since the linear $I - V$ curve was observed only for the samples having C-rich regions, especially, vertically shaped C-rich regions
- (3) The degradation of ohmic contacts by annealing at higher temperatures beyond the optimized temperature can be explained in terms of the structural

change of the C-rich area. After annealing at the optimized temperature, the C-rich area formed vertically, acting as an electron pathway. Above the optimized temperature, the ohmic contacts degrade because a horizontal C-rich region was developed in the contact metal region, leading to an increase in contact resistance due to the formation of NNS/NiSi contacts. However, the detailed effect of the Si-rich Ni-silicide and the horizontal C-rich region needs further investigation

Data Availability

The datasets generated during and/or analyzed during the current study are available from the corresponding author on reasonable request.

Conflicts of Interest

The authors declare that they have no conflicts of interest.

Authors' Contributions

Seongjun Kim and Hong-Ki Kim contributed equally to this work.

Acknowledgments

This research was supported by the GRDC Program through the National Research Foundation funded by the MSIT of Korea (NRF-2017K1A4A3013716).

References

- [1] F. L. Via, F. Roccaforte, A. Makhtari, V. Raineri, P. Musumeci, and L. Calcagno, "Structural and electrical characterisation of titanium and nickel silicide contacts on silicon carbide," *Microelectronic Engineering*, vol. 60, no. 1-2, pp. 269–282, 2002.
- [2] S. Y. Han, K. H. Kim, J. K. Kim et al., "Ohmic contact formation mechanism of Ni on *n*-type 4H-SiC," *Applied Physics Letters*, vol. 79, no. 12, pp. 1816–1818, 2001.
- [3] I. P. Nikitina, K. V. Vassilevski, N. G. Wright, A. B. Horsfall, A. G. O'Neill, and C. M. Johnson, "Formation and role of graphite and nickel silicide in nickel based ohmic contacts to *n*-type silicon carbide," *Journal of Applied Physics*, vol. 97, no. 8, p. 083709, 2005.
- [4] R. Kisiel, M. Guziewicz, K. Golaszewska, M. Sochacki, and W. Paszkowicz, "Mechanisms of carriers transport in Ni/*n*-SiC, Ti/*n*-SiC ohmic contacts," *Materials Science-Poland*, vol. 29, p. 233, 2011.
- [5] A. V. Kuchuk, P. Boriwicz, M. Wzorek et al., "Ni-based ohmic contacts to *n*-type 4H-SiC: the formation mechanism and thermal stability," *Advances in Condensed Matter Physics*, vol. 2016, Article ID 9273702, 26 pages, 2016.
- [6] M. W. Cole, P. C. Joshi, and E. Ervin, "Fabrication and characterization of pulse laser deposited Ni₂Si ohmic contacts on *n*-SiC for high power and high temperature device applications," *Journal of Applied Physics*, vol. 89, no. 8, pp. 4413–4416, 2001.
- [7] S. Tanimoto, M. Miyabe, T. Shiiyama et al., "Toward a better understanding of Ni-based ohmic contacts on SiC," *Materials Science Forum*, vol. 679-680, pp. 465–468, 2011.
- [8] A. V. Kuchuk, V. P. Kladko, K. Golaszewska et al., "The formation mechanism of Ni-based ohmic contacts to 4H-*n*-SiC," *Materials Science Forum*, vol. 717-720, pp. 833–836, 2012.
- [9] X. F. Zhang, Y. D. Tang, H. J. Shen et al., "Study on simultaneous formation of ohmic contacts on *p*- and *n*- type 4H-SiC using Ni/Ti/Al ternary system," in *2014 12th IEEE International Conference on Solid-State and Integrated Circuit Technology (ICSICT)*, Guilin, China, 2014.
- [10] Y. He, H. Lv, X. Tang et al., "Ohmic contacts simultaneously formed on *n*-type and *p*-type 4H-SiC at low temperature," *Journal of Alloys and Compounds*, vol. 805, article S0925838819326234, pp. 999–1003, 2019.
- [11] D. K. Schroder, *Semiconductor Material and Device Characterization*, John Wiley & Sons, Hoboken, NJ, USA, 3rd edition, 2006.
- [12] M. Wiets, M. Weinelt, and T. Fauster, "Electronic structure of SiC(0001) surfaces studied by two-photon photoemission," *Physical Review B*, vol. 68, article 125321, 2003.
- [13] C.-S. Lim, K.-B. Shim, D.-W. Shin, and K. H. Auh, "Phase distribution and interface chemistry by solid state SiC/Ni reaction," *The Korean Journal of Ceramics*, vol. 2, no. 1, p. 19, 1996.
- [14] J. A. Kittl, M. A. Pawlak, A. Lauwers et al., "Work function of Ni silicide phases on HfSiON and SiO₂: NiSi, Ni₂Si, Ni₃₁Si₁₂, and Ni₃Si fully silicided gates," *IEEE Electron Device Letters*, vol. 27, no. 1, pp. 34–36, 2006.

Research Article

Comprehensive Study of Kinetics of Processes Competing during PECVD Ultrathin Silicon Layer High-Temperature Annealing

Romuald B. Beck ^{1,2} and Kamil Ber¹

¹*Institute of Microelectronics and Optoelectronics, Warsaw University of Technology, Koszykowa 75, 00-662 Warsaw, Poland*

²*Centre for Advanced Materials and Technologies-CEZAMAT, Poleczki 19, 02-822 Warsaw, Poland*

Correspondence should be addressed to Romuald B. Beck; r.beck@imio.pw.edu.pl

Received 2 July 2019; Revised 9 October 2019; Accepted 20 November 2019; Published 3 December 2019

Guest Editor: Francesca A. Scaramuzzo

Copyright © 2019 Romuald B. Beck and Kamil Ber. This is an open access article distributed under the Creative Commons Attribution License, which permits unrestricted use, distribution, and reproduction in any medium, provided the original work is properly cited.

Application of low-temperature PECVD is a very tempting option for formation of ultrathin silicon layers for nanoelectronic and nanophotonic applications, as followed by annealing of this layer, regardless if executed as individual process performed in controlled ambient or during following high-temperature processes, allows for phase and content changes in the silicon layer. Understanding complex changes that can take place during such process, which depend on its temperature, conditions (e.g., oxygen availability), and timeframe, is a fundamental requirement for conscious application of such technology. It is worth realizing that nanodevices with their unprecedented variety of structures and devices require many different fabrication technologies. Hence, depending on the application in mind, different results of ultrathin silicon layer annealing may appear advantageous. During high-temperature processing (e.g., annealing) of PECVD ultrathin silicon layer, three competing effects have to be taken into account. These are amorphous silicon recrystallization and oxidation of amorphous and crystalline (as-deposited or just recrystallized from as-deposited amorphous phase) silicon (both of which by nature exhibit different kinetics). So far, most of attention has been paid to silicon recrystallization, which was justified by the fact that under experimental conditions studied (silicon multilayers) oxidation was certainly of less importance. In certain applications, the required device structure consists of single (and not multiple) ultrathin silicon layer, and thus, oxidation effects certainly have to be included into considerations. Understanding dynamics and very complex relations between these individual effects is thus mandatory for using consciously this technique and achieving needed properties of the layer. It has to be stated clearly that although the achieved results, presented in this study, refer to the silicon layers fabricated under certain conditions (particular type of PECVD reactor and process parameters), they can, however, be easily extrapolated for similar cases too. The presented below results are, to our knowledge, the first successful attempt to address these issues.

1. Introduction

Silicon nanocrystals have been investigated very intensively for more than two decades. Many potential applications have been considered and many methods of their formation studied. For very broad (216 references) and recent review of these issues, see [1].

In many applications, we find double oxide barrier structure (ultrathin layer stack—oxide/silicon/oxide). Depending on application, different requirements on the physical structure and properties of silicon ultrathin layer in this stack can be requested. The most intriguing case is

the possibility of obtaining silicon nanocrystals (nanodots) in the dielectric (oxide) matrix, which can be achieved by very carefully achieved combination of recrystallization and oxidation processes. As both of these processes require high temperature, they can take place at the same time, simultaneously, providing appropriate conditions are satisfied. It is worth realizing that the main difference between the conditions needed for them is the availability of oxygen, which is indispensable for the oxidation process, while not needed for recrystallization.

In reality, oxygen-free conditions can only be obtained in high-temperature annealing process in case of complete lack

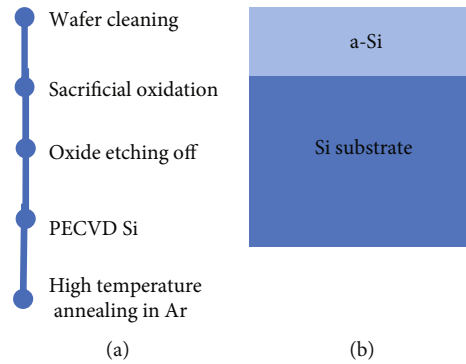


FIGURE 1: Schema of the (a) used process flow and the (b) fabricated structure.

of oxygen source in the reactor, i.e., no oxygen in supplied gas nor oxygen is released (e.g., outdiffused) from any layer that the annealed structure consists of. While the former condition is relatively easy to provide, the latter one is not (as it will be shown in this paper).

So far, many studies on amorphous silicon recrystallization ignored silicon oxidation and its potential effect on high-temperature recrystallization process (e.g., [2–4]). This approach was justified in some of these works by the fact that in the multilayer structure (some tens of ultrathin silicon layers located in between silicon oxide layers) with high-temperature stoichiometric thermal oxide used in these investigations, the probability of releasing oxygen from the oxide layers was very low. At the same time, most of the silicon layers in the stack were far beyond diffusion length of oxygen from ambient gas during high-temperature annealing. Hence, measured by photoluminescence, Raman or XRD signals averaged across the whole stack could not identify changes in SiO_2 content.

In the studied case of single ultrathin silicon layer behavior, where quantitative data were needed, spectroscopic ellipsometry was used for the investigation of changes in phase and thickness of ultrathin PECVD silicon layer.

This detailed study is believed to provide grounds for practical use of annealing and/or oxidation of PECVD ultrathin silicon layers to fabricate different nanoelectronic and nanophotonic devices.

2. Experimental

2.1. Sample Preparation and Technology. In the experiments, Si (100) 5–9 Ωcm boron-doped wafers were used as substrates. In order to achieve atomically flat silicon surface after standard RCA-based (HF-last) cleaning, the wafers underwent so-called “sacrificial oxidation” followed by selective oxide etch (as shown in Figure 1). This allowed to achieve atomic flat silicon and defect-free monocrystalline surface (confirmed previously by TEM observations).

Basing on previous results presented in [5], which have proved that the recrystallization process is practically not influenced by direct contact of PECVD layer with monocrystalline silicon substrate, and on a spectroscopic ellipsometry study presented in [6] proving that an ultrathin silicon PECVD layer can be successfully analyzed on Si substrate,

in this work, the ultrathin silicon was PECVD deposited directly onto the monocrystalline silicon wafer.

For the PECVD processing, the Oxford Plasma Technology 80+ system was used. The silicon PECVD process optimized for low deposition rates as reported previously in [5, 7, 8] has been used. Deposition of silicon PECVD layers was performed using SiH_4 (2%): He diluted in 5N purity argon (150 sccm and 50 sccm, respectively); the deposition temperature is 350°C and the R.F. power is 25 W.

Within this study, two types of samples were fabricated. They differed by thickness of PECVD Si layer only (the same deposition parameters were used except for deposition time) and will be referred to hereafter as “thin” and “thick” (as-deposited layer thicknesses were 53 Å and 84 Å, respectively). These two types of samples with differing thicknesses of Si PECVD layer appeared to be indispensable, as will become clear in Section 3 of this paper, for analysis of reasons of oxide growth saturation during high-temperature annealing.

High-temperature annealing was performed in typical semiconductor high-temperature furnace in quartz tube. Argon of 5N (99.999%) purity was used for this purpose. In order to have fair comparison of results of annealing, the wafers were divided into quarters for annealing. The annealing conditions and times were chosen based on the previous experiments and were set to 700°C , 800°C , 900°C , and 1000°C and 1, 2, 3, and 5 minutes, respectively.

2.2. Characterization Method of the Obtained Structures and Results of Annealing. The results of structure manufacturing were then examined by spectroscopic ellipsometry study. This method was already proved (e.g., in [5–11]) to be very sensitive and reliable, while fast and nondestructive.

For spectroscopic ellipsometric studies UVISEL-NIR by Jobin-Yvon and supplied with this equipment modelling software has been used. It allows performing ellipsometric measurements within wide range of wavelengths, i.e., from 190 nm to 880 nm, if necessary under different angles of beam incidence. As a rule, measurements and then fitting were performed in the whole allowed by the tool wavelength spectrum. The enclosed to this tool materials’ data base and several optical models to choose from allow for nondestructive and very sophisticated characterization of

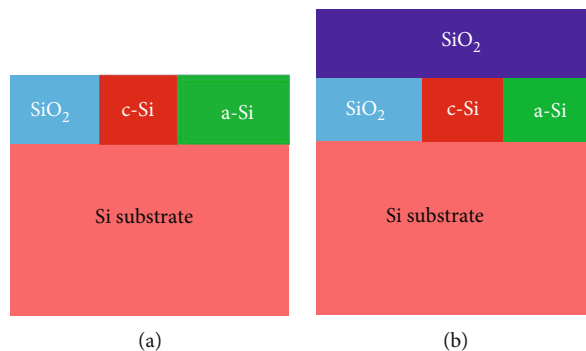


FIGURE 2: Schemas of optical models used for analysis of spectroscopic ellipsometry data: (a) for the as-deposited single PECVD Si layer parameter determination and (b) for evaluation of structure properties after annealing process. In order to differentiate the two silicon oxides, the oxide phase in the silicon layer will be referred to as “SiO₂ in PECVD Si,” while continuous oxide layer as “SiO₂ on top”.

TABLE 1: Thickness and phase composition of as-deposited “thin” and “thick” PECVD layers.

	“Thin” layer		“Thick” layer	
	Composition (%)	Phase thickness (Å)	Composition (%)	Phase thickness (Å)
a-Si	49	26	68	57
c-Si	30	16	15	13
SiO ₂	21	11	17	14
Total for PECVD silicon layer	100	53	100	84

single and multiple layers. When used carefully, it allows not only to determine individual layer thickness (even in the multiple layer stack) but also (with some limitations) to study phase compositions of the layers. For more information on these models, see [12]. Formally, content of up to three phases or compounds within a single layer is possible to be evaluated from this optical model. These features have been fully explored in this study. The validity of this approach has been already proved and discussed in more details in [6].

In order to discuss and compare the behavior of each of individual phases in PECVD silicon layer during the studied high-temperature processes, the concept of “phase layer thickness” will be used hereafter. This concept has already been introduced and discussed in our previous works (e.g., in [5, 6, 8]). The multiphase PECVD silicon layer is described in optical models used in this study by its physical thickness and its composition expressed in percentage of the layer. The used hereafter terms “phase thickness” (a-Si phase thickness, c-Si phase thickness, or SiO₂ phase thickness) are, thus, obtained by multiplying overall physical thickness of the layer by composition percentage of the particular phase. As a result of this, the overall PECVD Si layer thickness (as evaluated from ellipsometric measurements using the assumed optical model) is equal to the sum of these “phase layer thicknesses.” The advantage of this approach is that using these parameters one can independently follow possible changes in both, in physical layer thickness and in its composition.

It should be stressed, however, that phase thickness concept neither assumes nor provides information on location of particular phases constituting the layer (as has already been discussed in [8]).

Each of the produced samples has been measured in at least 3 points in order to avoid that some local behavior artefact may be misinterpreted as a characteristic feature of the tested sample. Providing the difference in results of analysis performed in each of all the measured points was acceptably small, the average values were then calculated and used for the analysis and discussion. In few occasions only, where the data scatter on the sample was considered unacceptably high, the statistics of the measurements was improved by measuring at more individual locations.

Such an approach is justified by the fact that spectroscopic ellipsometer spot size is by far greater than that of the expected nanocrystals. This means that this measurement method is, by nature, providing information on average character over the spot area in the sample.

3. Results and Discussion

3.1. Characterization of As-Deposited PECVD Si Layers. The ellipsometric analysis of the as-deposited PECVD Si films was performed using an optical model shown schematically in Figure 2(a). In this model, three phases are expected in this single layer, namely, amorphous silicon phase (a-Si), nanocrystalline silicon phase (c-Si), and silicon oxide phase (SiO₂). It allows to evaluate the initial content of the layer and hence allows to follow changes in phase composition of this layer resulting from the studied annealing processes.

The obtained composition of the as-deposited “thin” and “thick” PECVD layers is shown in Table 1.

It is interesting to realize that although the main contribution to the as-deposited PECVD layer thickness (volume) comes (as expected) from a-Si, there already exist also nanocrystalline silicon (c-Si) and silicon oxide (SiO₂) phases. The

difference in thickness between the “thin” and “thick” layers is primarily due to the difference in amorphous phase content, while c-Si and SiO₂ phases change only a little. Another intriguing fact is that c-Si seems to decrease with PECVD time (is thinner for thick layer). This behavior is in agreement with observations obtained for high-temperature annealing which will be discussed below. While the presence of both phases of silicon is obvious, the origin of the SiO₂ phase is, at the first glance, not.

Although no oxygen is used in PECVD of silicon layer, one has to remember that humidity is very difficult to pump down in vacuum reactor chambers, so (unless load-lock system is used) its presence in the reaction chamber has to be taken into account. On the other hand, bare silicon surface is exceptionally reactive when exposed to ambient atmosphere and natural oxide grows on such a surface in a matter of minutes. Hence, it is reasonable to attribute the detected in as-deposited layer SiO₂ phase to thin natural oxide spontaneously grown on silicon wafer surface after wafer cleaning procedure prior to PECVD process and some SiO₂ particles resulting from reaction of deposited Si with oxygen leftovers present in the reaction chamber during PECVD.

It should be stressed that fittings of the optical model presented in Figure 2(a) to experimentally obtained spectroscopic ellipsometry data were very good (RMS ≤ 0.1 (RMS (Root Mean Square) deviation error in this case is representing the accuracy of fitting theoretical optical model to the real results of ellipsometric measurements, hence confidence level to evaluate this method parameter of the optical model (whether it is thickness, thickness and/or optical properties, or thickness and/or composition).) for the whole measured spectrum), thus should be considered as reliable.

During high-temperature annealing, especially in high purity gases (in our case Ar 5 N better than 99.999% was used), it is expected that (depending on temperature and time) only annealing process leading to reduction of defect density in the as-deposited silicon layer (PECVD Si) or this layer recrystallization, resulting in the formation of silicon nanocrystals, takes place. In extreme situation, there potentially exists a possibility of complete recrystallization of as-deposited silicon layer, i.e., formation of a single crystal (monocrystalline) layer across the wafer. The situation differs significantly if there is oxygen available during the annealing process and whether its source is limited or unlimited. Under such conditions, we can expect competing (with annealing) process of oxidation. Consequently, depending on the amount of oxygen available for oxidation, we can expect either continuous, unlimited growth of silicon oxide phase or its saturation due to consumption of all available oxygen in the system.

For this reason, in the studies on the results of annealing experiments (similarly as in [5]), a slightly different optical model of the structure for spectroscopic ellipsometry data analysis was used. It differs by additional oxide layer placed on top of the silicon layer (defined exactly as for as-deposited silicon PECVD layer) and is shown schematically in Figure 2(b). In order to distinguish in the discussion below the oxides, the additional one will be hereafter referred to as

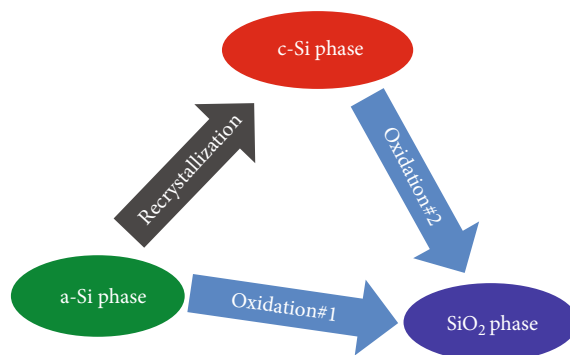


FIGURE 3: Schema of effects competing during high-temperature processes for PECVD silicon ultrathin layer containing structures.

“SiO₂ on top,” while the one present in the silicon layer as “SiO₂ in PECVD Si.”

3.2. Silicon Oxidation. As this has been already mentioned above, there already exists SiO₂ phase in the as-deposited silicon layer. Further changes in oxide phase content strongly depend on the additional availability of oxidant species during high-temperature annealing processes. Few more potential sources of oxygen that can fuel silicon oxidation can be named. Summarizing, we could expect them to be as follows:

1. Natural silicon oxide layer located between the silicon monocrystalline substrate and PECVD Si
2. Water vapor adsorbed on sample surfaces before their loading into a high-temperature furnace
3. Water vapor adsorbed on reactor walls during its loading/unloading and, thus, present during PECVD Si (this can be prevented by using loadlock system in PECVD reactor)
4. Diffusion through the wall of quartz tube in the high-temperature furnace used for annealing (which can, potentially, be prevented fully only by double wall quartz tube system and is strongly quartz tube temperature history dependent)

Under these circumstances during high-temperature annealing, along with the processes mentioned above (defect annealing, recrystallization), we also have to take into account the process of oxidation of amorphous silicon a-Si (represented in Figure 3 as “oxidation#1”). We also have to consider another oxidation path, which consumes nanocrystalline silicon c-Si (represented in Figure 3 as “oxidation#2”). It should be underlined that these two processes can potentially have different kinetics, due to difference in crystalline structure of silicon consumed for thermal oxidation. It also has to be remembered that kinetics of both processes is highly dependent on availability of free silicon (either a-Si or c-Si for “oxidation#1” and “oxidation#2,” respectively) and of free oxygen. The specificity of the structures under consideration is that providing all silicon from the PECVD Si layer is already consumed, oxidation can continue further

by consumption of silicon from monocrystalline substrate. In order to be able to take into account this effect, two series of samples were fabricated, i.e., with “thin” PECVD Si and “thick” PECVD Si.

The complexity of results of high-temperature annealing of PECVD Si layer can be schematically presented as shown in Figure 3.

Consequently, in order to understand the experimentally obtained results of annealing of structure of interest, we have to compare the kinetics of all three processes potentially involved. It should be realized that in many potential applications the ultimate goal of processing would be formation of silicon nanocrystal (nanodot) matrix suspended within the oxide volume. Depending on their relative rate, this final aim may or may not be possible to achieve by annealing or annealing/oxidation process. Hence, even more important is careful analysis of these competing processes.

The following part of this paper describes the experiments and analysis of the results aimed at fulfilling this requirement.

3.3. Silicon Recrystallization. Recrystallization of amorphous silicon thin layers in high-temperature treatments formed by various methods has already been reported before (e.g., [1–5, 12–18]).

In the preceding study experiments, we have experimentally verified a wide range of annealing temperatures and times, i.e., temperatures from 350°C up to 1100°C and times from few minutes to a quarter of an hour. The obtained results have already been published in [8]. Basing on the results in this study, values of these parameters have been narrowed to temperature range between 700°C and 1000°C and limited annealing time to 5 minutes only for current experiments. In order to remove from the studied system difficult to control source of oxygen while not affecting recrystallization process (as it was already determined in [5]), in the current study, no SiO₂ layers were fabricated below and top of the PECVD silicon layer.

Using two types of samples, “thin” and “thick,” was also advantageous from the perspective of study of recrystallization effects. They allowed us to verify if recrystallization behavior is dependent (within examined range) on the initial thickness and volume of amorphous silicon layer.

3.4. Oxidation and Recrystallization Kinetics: Temperature Dependencies. The obtained results are presented in Figures 4 and 5. Comparing the results obtained for “thin” and “thick” PECVD Si film annealing, one can realize that although there are some differences between them, some universal characteristic features can also be noticed. In fact, we can realize that the “thick” case copies the behavior of all the annealed layers under study of the “thin” one, but in a different timeframe. It is interesting to realize that some things seem to happen much slower for the “thin” than for the “thick” case. This has already been reported in numerous papers in respect to crystallization process and attributed to difference in stress in the layers (e.g., [3, 13, 14]). In this study, this refers not only to the qualitative behavior of silicon phases but also to oxides. In both cases, we can see that

the lowest annealing temperature (700°C) is too low to get recrystallization effects within the PECVD Si film (see Figures 4(a) and 5(a)). This is in agreement with the results of studies presented before for various methods of layer deposition (e.g., [13]). On the contrary, during the first minute, the originally observed crystalline phase of this layer (c-Si) disappears (completely for “thick” and almost completely for “thin” case). It is intriguing to realize that this trend is similar to the one observed for low-temperature annealing (350°C) that takes place *in situ* during PECVD itself. As already reported above, as-deposited “thick” silicon layers contained less (percentagewise) c-Si phase content than the “thin” one (deposited shorter, hence exposed shorter to raised deposition temperature).

Interestingly, the silicon oxide phase within the PECVD Si (“SiO₂ in PECVD Si”) layer remains almost constant during annealing, while oxide on the top of the structure grows. The oxide growth is slow and tends to saturate for annealing times longer than 3 minutes. This can be explained either by typical for this temperature range behavior of kinetics of silicon oxidation (see [15]) or exhausted already (at this moment) source of free oxygen needed to continue the oxidation process.

For 800°C, we still can see the initial period (first minute) during which c-Si disappears (see Figures 4(b) and 5(b)). In this case, however, from this moment noticeable (for “thin” case) and almost complete (for “thick” case) recrystallization of silicon phase occurs. The kinetics of this process differs significantly depending on the original thickness of the silicon layer. For the “thick” one, recrystallization rate is very high, much higher than that for the “thin.” Within a minute (between 1 and 2 minutes of annealing), it reaches its final state (for which more than 90% of free silicon is nanocrystalline). This is not the case for the “thin” silicon layer, for which recrystallization is relatively slow and it takes 5 minutes to achieve approximately 75% of c-Si phase content in free silicon. This observation can be considered as supporting report of Zacharias and Streitenberger [19] in which they have shown that crystallization temperature is strongly dependent on initial a-Si layer thickness and it abruptly increases with decreasing silicon layer thickness. It should be noticed, however, that according to [19] the crystallization temperatures for Si layer of similar thickness to the ones in our study, i.e., approximately 5 nm and 8 nm (corresponding to “thin” and “thick” cases), are approximately 1050°C and 1000°C, respectively, thus are significantly higher than those observed in our study.

Considering the influence of internal stress in a-Si layers on recrystallization behavior (among others, temperature), which has been shown and discussed by Zacharias and Streitenberger in [19], one could draw then indirect conclusion that PECVD a-Si layers fabricated in our study exhibit far less internal stress than those studied by Zacharias et al. It should be kept in mind, however, that while in [19] a-Si thermal recrystallization was performed using multilayer stacks in which each of the a-Si layers was located in between two SiO₂ (plasma oxidized) layers, in our study, a-Si was deposited directly on monocrystalline silicon substrate with potentially only natural oxide at its both interfaces. Also, the

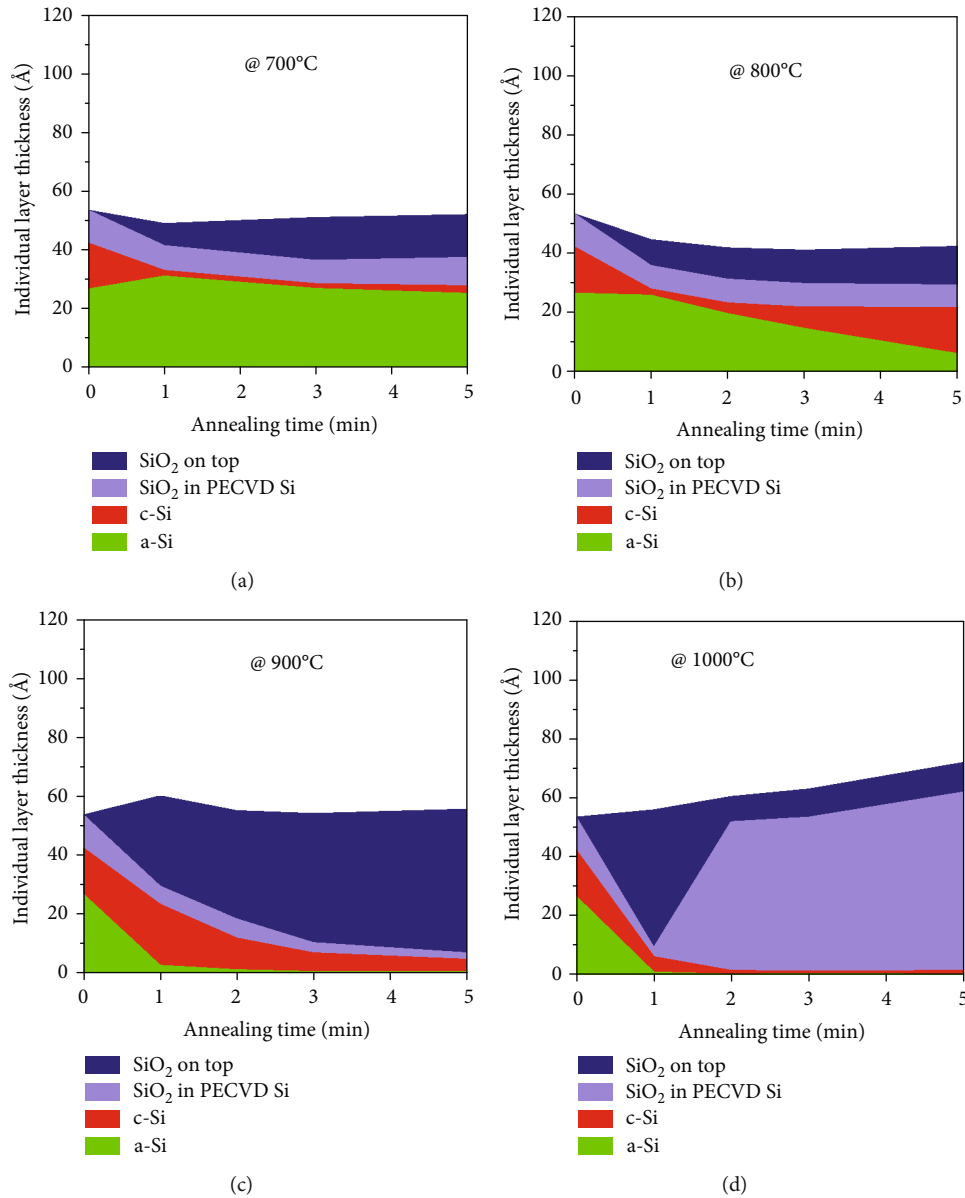


FIGURE 4: Individual layer and phase reaction to annealing in pure argon at (a) 700°C, (b) 800°C, (c) 900°C, and (d) 1000°C of “thin” PECVD Si layer. PECVD Si layer consists of a-Si, c-Si, and SiO₂ in PECVD Si phases. SiO₂ on top is determined as a separate layer.

method of a-Si layer formation was different in [19], as magnetron sputtering (presumably with no external heating during deposition) was used for this purpose in this work.

As can be seen in Figures 4(b) and 5(b), in this temperature, oxide formation is also slow and in both cases oxide thickness saturation can be observed. In fact, oxide thicknesses are very similar for both groups of samples.

The recrystallization process behaves differently for 900°C. In both cases (“thin” and “thick,” see Figures 4(c) and 5(c), respectively), we do not observe any more amorphization of the initial c-Si phase (reported above for the beginning of annealing at lower temperatures). Instead, we can see that in this temperature both “thick” and “thin” silicon layers get practically completely recrystallized during this first minute of annealing. As regards oxide formation, in this temper-

ature, oxide thickness is similar in both cases. This is not surprising as although recrystallized silicon phase is decreasing during the annealing after the first minute, even for “thin” silicon layer some c-Si are left and can potentially undergo oxidation providing there is still some free oxygen available in the system. The oxide growth is slightly higher than for 800°C, which is consistent with oxidation process kinetics temperature dependence. More detailed discussion on the oxidation issues are to be found below.

In 1000°C, alike in 900°C, recrystallization of amorphous silicon for both “thick” and “thin” cases is completed within the first minute of annealing (see Figures 4(d) and 5(d)). We can, however, observe very high consumption rate of silicon (after the first minute) by oxidation, which at 1000°C is very fast indeed. In fact, for the “thin” case, free silicon is

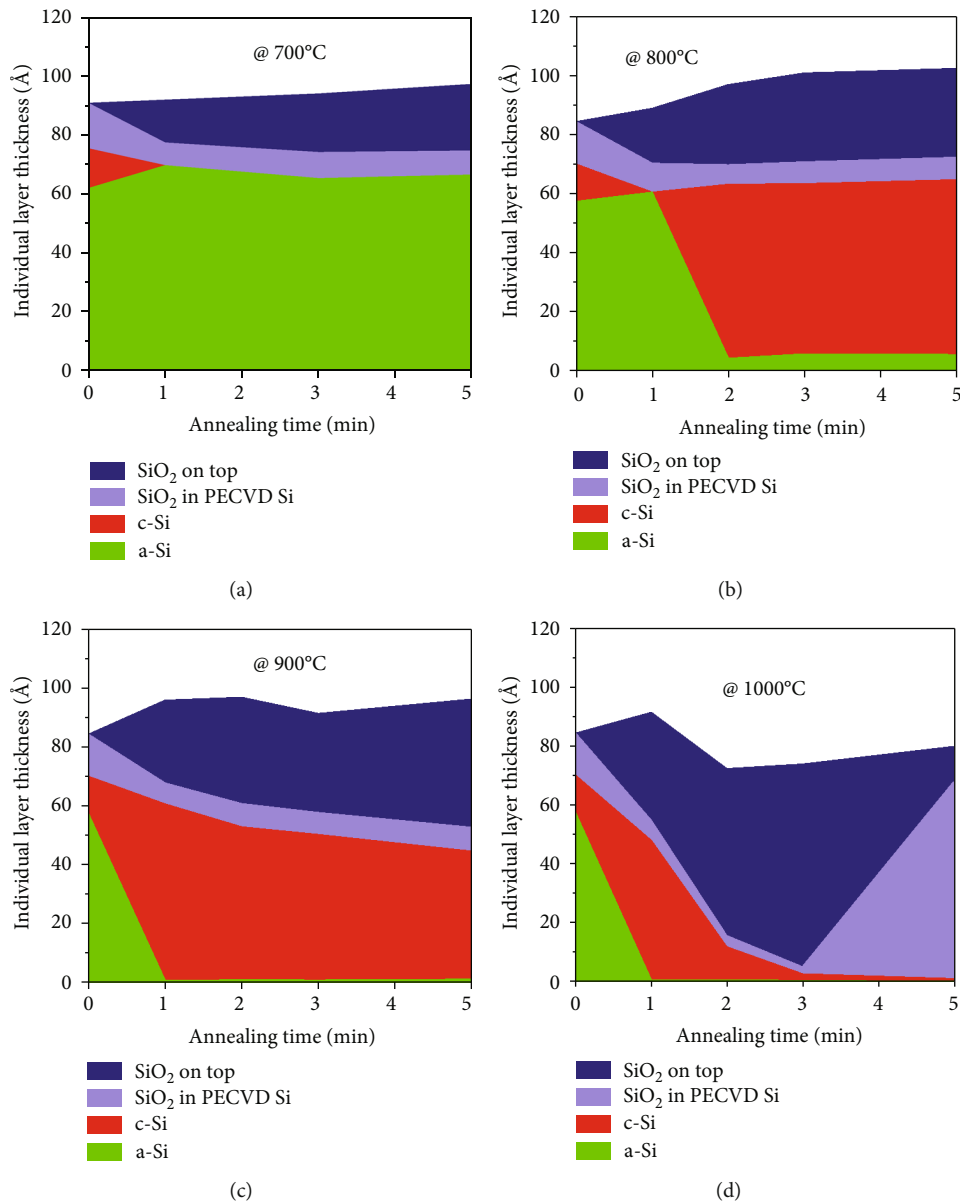


FIGURE 5: Individual layer and phase reaction to annealing in pure argon at (a) 700°C, (b) 800°C, (c) 900°C, and (d) 1000°C of "thick" PECVD Si layer. PECVD Si layer consists of a-Si, c-Si, and SiO₂ in PECVD Si phases. SiO₂ on top is determined as a separate layer.

consumed almost completely during the first 2 minutes, while for the "thick" layer case this takes only one minute longer (at 3 minutes).

It is interesting to realize that for all temperatures lower or equal to 900°C, the oxide growth is attributed by optical model to the continuous "SiO₂ on top" layer, while "SiO₂ in PECVD Si" holds almost completely stable within the whole range of examined annealing times. This is no more true for 1000°C for which (in both cases) "SiO₂ on top" is at some moment of annealing "replaced" by "SiO₂ in PECVD Si." For the "thin" case, this happens in between the first and second minutes of annealing, while for the "thick" case sometime between the third and fifth minutes of annealing.

In order to try to understand better the effects leading to the results described above, one should draw attention to few more facts.

For more in-depth analysis of oxidation process, a different representation of the obtained experimental data is advantageous. For this purpose, it is better to consider total oxide thickness ("SiO₂ on top" plus "SiO₂ in PECVD Si") and total free silicon (a-Si plus c-Si) in the studied systems. The obtained time dependencies for all studied temperatures and both "thin" and "thick" cases are shown in Figure 6.

From Figure 6(a), it becomes clear that for 800°C and below, for both "thin" and "thick" cases free silicon behaves similarly. We observe saturation of its consumption by oxidation and it remains even for the longest annealing times used in the experiment. The situation for 900°C, however, depends on the initial thickness of the annealed layer. For the "thin" case, free silicon disappears almost completely, while for the "thick" case a lot of it remains still available in the layer. We can see that the rate of silicon consumption

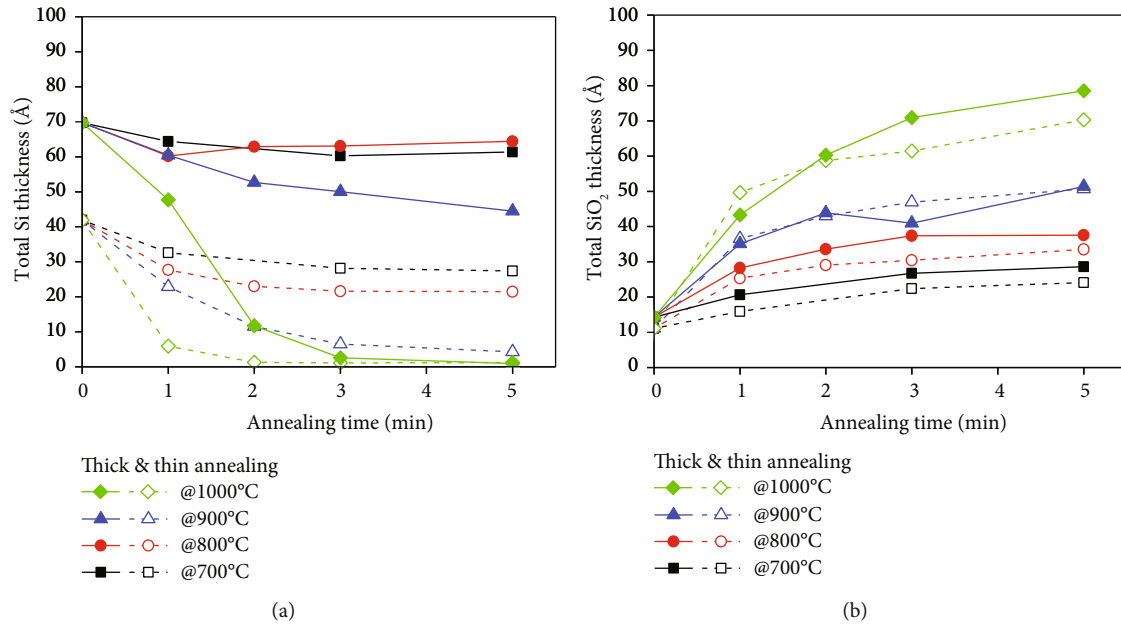


FIGURE 6: Changes during high-temperature annealing for two types of samples with “thin” PECVD Si layer (dashed lined and empty symbols) and with “thick” PECVD Si layer (full lines and symbols) of (a) total free silicon (a-Si+c-Si) and (b) total oxide thickness (“SiO₂ on top”+“SiO₂ within PECVD Si”).

in both cases seems almost independent on initial silicon thickness. For annealing at 1000°C, the rate of silicon consumption by oxidation differs at first glance dramatically. Careful look allows, however, to realize that the kinetics of free silicon consumption at the beginning stages of annealing is similar (compare the “thin” case up to 1 min and the “thick” case up to 2 minutes), while the main difference is that it takes at least one more minute to consume free silicon in the “thick” PECVD Si layer. In fact, practically all the free silicon is consumed within 2 minutes of annealing for “thin” and 3 minutes for “thick” cases at this temperature. If oxidation kinetics would be controlled by silicon availability, the oxide growth should completely stop after 2 min for “thin” and after 3 min for “thick” PECVD Si layer annealing. In Figure 6(b), we can see that this is not the case. Oxide growth does take place in this time regime and its rates are very similar (see also Figure 7). This leads clearly to a conclusion that oxidation kinetics is controlled by oxygen and not by silicon availability. Once free silicon originating from PECVD Si layer is not available any more for the oxidation process, silicon from the silicon substrate layer is consumed. This effect cannot be recognized in by ellipsometric measurements and available optical models.

Looking at the presented kinetics of oxide formation in Figure 6(b), one can realize that the starting point for “thin” and “thick” layers differs by few Angstroms. Taking this into account, results in oxidation rate (see Figure 7) for annealing temperatures up to 900°C of both “thick” and “thin” cases are being practically the same (with the exception of one point at 3 minutes for “thick” one, which will be discussed in more details below). Interesting effect occurs for 1000°C, where at the beginning of annealing oxidation rates differ significantly, with gradual slowdown in time for “thick” layers and abrupt for “thin” ones. Still, both oxidation rates meet at the end of

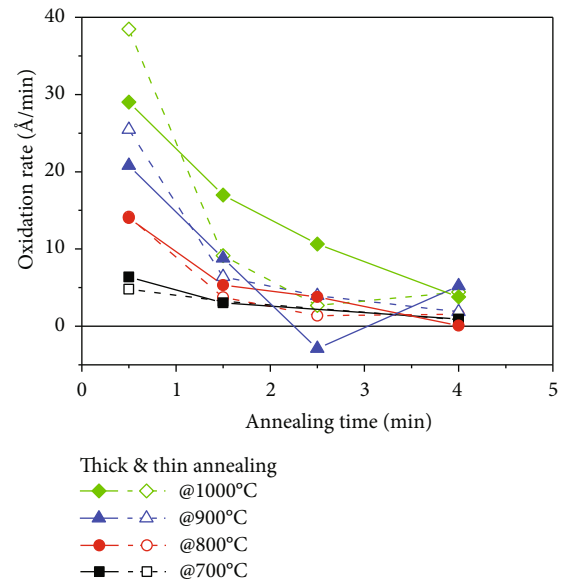


FIGURE 7: Oxidation rates (calculated from data shown in Figure 6(b), attributed to the center of each of time slots) during high-temperature annealing for the two types of samples, with “thick” and “thin” PECVD Si layers (full symbols/solid lines and open symbols/dashed lines, respectively).

the examined annealing time range, i.e., between 3 and 5 minutes. This can potentially be a consequence of the observation referred already above (see also Figure 6(a)) that at 1000°C free silicon is consumed in the “thin” layer already by the end of the second minute of annealing, while for the “thick” layer it takes one more minute (no free silicon is practically available after the third minute of annealing). Hence,

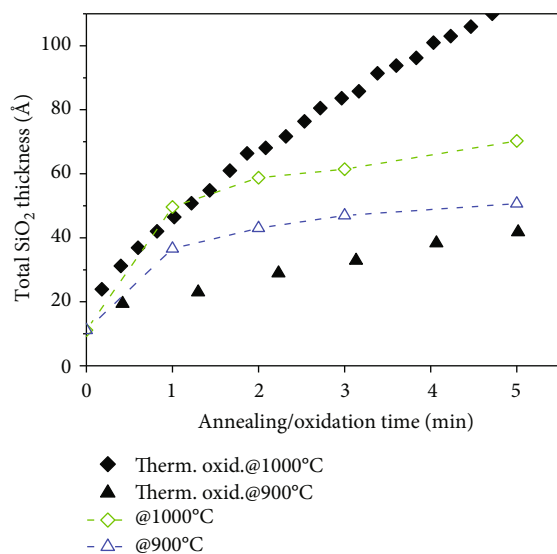


FIGURE 8: Total oxide thickness (“SiO₂ on top”+“SiO₂ within PECVD Si”) changes during high-temperature annealing for the two types of samples: with “thin” PECVD Si layer (full lines and open symbols) and for standard RTO (data from [20]) (full symbols).

at this temperature, we can divide the examined annealing time range into three stages:

- (1) Oxidation consumes only free silicon from the PECVD Si layer (this takes place during the first minute of annealing for “thin” layers and 2 minutes for “thick” ones)
- (2) Transition period, during which free silicon from the PECVD Si film does not provide enough silicon for oxidation (this takes place during the next 1-2 minutes range for “thin” and 2-3 minutes range for “thick” (see Figure 6(a)))
- (3) Oxidation can take place only by consuming monocrystalline silicon substrate (takes place from the 2nd minute for “thin” and the 3rd minute onwards for “thick” layers)

All the presented discussion on oxidation kinetics has not so far referred to the problem of limitation of availability of oxygen during the annealing process. In order to address this issue, it is suggested to compare experimentally observed oxide growth during annealing with kinetics of oxidation performed with unlimited supply of oxygen (Rapid Thermal Oxidation (RTO) [20]). The comparison for two temperatures, namely, 900°C and 1000°C, and the “thin” case is shown in Figure 8. It can be clearly seen that oxidation rates behave significantly different for both temperatures compared.

For 1000°C, oxide growth during the first two minutes is almost identical for rapid thermal oxidation (RTO) and oxidation during PECVD silicon layer annealing. Only afterwards, oxidation rate during RTO exceeds that for

annealing. Taking into consideration that for the “thin” case for annealing times longer than 2 minutes, oxidation takes place by consumption of monocrystalline silicon substrate (see discussion above), exactly as in the case for RTO, this difference can only be attributed to the limitation of oxygen in the reaction chamber of annealing furnace. In consequence, this observation fully supports the conclusion presented in this study that oxidation rate is controlled by the deficiency of free oxygen in the system. It has to be realized then that depending on the nature of oxygen source in the experimental system oxidation may continue or can ultimately stop. The moment it happens, as well as the degree of oxygen limitation (hence also oxidation rate) is strictly individual, as according to our discussion above, the potential sources of oxygen in the system can vary significantly between different procedures and equipment used in particular laboratories.

For 900°C, the situation is different. The overall oxide thickness (sum of “SiO₂ on top” and “SiO₂ in PECVD Si”) resulting from the annealing in this temperature is much higher than that achieved during RTO (see Figure 7). At first glance, this seems to be nonsense. How can the actual oxidation rate be higher than the thermal oxidation rate under standard conditions (i.e., with unlimited silicon and oxygen supply) at the same temperature? This effect can be explained by the following fact. Standard thermal oxidation takes place at the already formed oxide-silicon substrate interface due to oxygen supplied from the ambient atmosphere to this plane by means of numerous mechanisms (highly dependent on the current thickness of the oxide layer, see [21]). Thus, in typical process, we have a chemical reaction that takes place primarily at a certain plane. In our case, on the contrary to the typical situation, we have oxygen atoms not only in the ambient atmosphere but some of them are already incorporated in the PECVD Si layer volume. Hence, oxidation in the studied case does not take place at a single “reaction plane,” but in the whole volume of PECVD Si layer. This way, oxide growth higher than that for the typical process is possible and justified. This hypothesis can be also supported by an observation that as oxidation time increases and according to our mentioned above observations, availability of free oxygen becomes reduced, the difference between oxidation behavior of PECVD Si and RTO process becomes smaller and it seems reasonable to expect that will become negligible for longer annealing times.

It also has to be pointed out that for both “thick” and “thin” cases for 900°C, “SiO₂ in top” prevails “SiO₂ in PECVD Si,” while for annealing times longer than 2 minutes at 1000°C it is the other way round. One has to realize that these two types of oxides are not the same in at least two ways. While “SiO₂ on top” is assumed to be a continuous layer on top of the sample, “SiO₂ in PECVD Si” may not be. From the optical model point of view, it is one of the phases present in the layer on top of silicon substrate and covered by continuous “SiO₂ on top.” Once “SiO₂ in PECVD Si” prevails free silicon content (sum of the other two phases in this layer, i.e., a-Si+c-Si), it becomes reasonable to assume that the remaining silicon is located in this layer in one of the two forms shown schematically on Figure 9. Under these



FIGURE 9: Schematic view of two potential interpretations of complex composition in PECVD Si layer: (a) continuous crystalline silicon “sublayer” and (b) matrix of silicon nanocrystals, both within the oxidized PECVD Si layer.

circumstances, one can potentially have either very thin, continuous crystalline silicon layer (Figure 9(a)) or silicon nanocrystals surrounded by silicon oxide (Figure 9(b)). These two forms cannot be distinguished by means of ellipsometry due to averaging effect resulting from size of ellipsometric spot (of the order of hundred micrometers) compared to a size of silicon nanocrystals (of the order of nanometers). If we realize that for 1000°C both “thick” and “thin” cases exhibit only few Angstroms of c-Si phase left, then oxide matrix with some intrusions of silicon nanocrystals seems to be by far a more probable option. For 900°C , however, there is a significant difference between the “thin” and “thick” cases. The “thin” case reminds situation observed for 1000°C , with only few Angstroms of silicon remaining after the first minute of annealing. For the “thick” case, however, even for 5 minutes annealing, there remains most of the initial silicon phase thickness. This can be explained by considerable oxidation kinetics slow down for annealing times above 2 minutes observed in Figure 6(b) (or Figure 7). As a consequence, it seems justified to claim that in temperatures around 900°C , we can independently control recrystallization and oxidation process by means of annealing time. Choosing appropriate initial silicon PECVD layer thickness provides opportunity to control nanocrystal size under these conditions. Further optimization is needed to establish precise dependencies between these parameters. It is important to realize that due to stress dependency of crystallization behavior, any change in PECVD silicon deposition process which may change the internal stress in this layer will inevitably influence the temperature and time dependence of the optimum annealing conditions.

4. Summary

The comprehensive study presented above allowed to obtain important observations and draw from them numerous conclusions that are potentially of great interest for considerations on methods of fabrication of different types of structures and devices for electronic and photonic applications.

Within this study, it has been proved once again how valuable spectroscopic ellipsometry-based analysis can be for providing information on structure and phase composition of complex ultrathin layers and studies on their variability and changes during processing. Using consequently the same optical model along the annealing process analysis provided unique opportunity of straightforward following complex processes taking place during this high-temperature annealing.

The obtained results proved that the proposed dual path between free silicon and silicon oxide phase (path via recrystallization and then oxidation in parallel to direct oxidation of amorphous phase of silicon) allows to represent, analyze, and explain complex events that take place during high-temperature annealing of primarily amorphous PECVD silicon layer.

Providing ultrapure neutral gas (e.g., 5 N purity) for high-temperature processing does not ensure oxygen-free ambient atmosphere during it. There exist numerous sources (limited and unlimited in time) that have to be taken into consideration when analyzing results of the high-temperature process, especially in nanoscale. This is particularly true for silicon due to exceptionally quick growth of natural oxide even at room temperature.

The oxygen present within the ultrathin layer can change significantly the behavior and kinetics of the events taking place during high-temperature processing. In this study, it has led, for example, to oxidation rates higher than that for standard oxidation (with unlimited supply of oxygen).

The discussed results in this paper proved very high dependence of both oxidation and recrystallization process on temperature. From the perspective of recrystallization process, 700°C is too low to observe this effect, while 1000°C is too high (recrystallized silicon is almost instantly consumed by oxidation).

The process of silicon recrystallization in lower temperatures studied (i.e., 700°C and 800°C) is preceded by the decomposition of silicon crystals regardless of the initial thickness, while for temperatures above (i.e., 900°C and 1000°C) amorphization process cannot be noticed. Nanocrystalline silicon phase replaces amorphous silicon very quickly (regardless of the initial deposited layer thickness) and its content decreases in time due to the oxidation process.

Recrystallization rate and its temperature dependence are also strongly affected by the method and formation conditions (deposition parameters) used for silicon layer fabrication, which can be explained by different internal stress in the layer.

Similar to recrystallization, for oxidation, lower temperatures (i.e., 700°C and 800°C) are not sufficient to consume free-silicon phase in the deposited layer. On the contrary, annealing at 1000°C leads very quickly to complete consumption of free-silicon phase in the layer.

From the perspective of potential applications, the most interesting are temperatures around 900°C , for which, depending on the initial silicon layer thickness, one can achieve either completely recrystallized silicon phase in the form of nanocrystals (alternatively atomic thin silicon layer) suspended within the oxide.

Oxidation process, after certain time, becomes controlled (limited) additionally by oxygen availability in the reactor

and in the deposited silicon layer. This makes it sensitive to the methods of silicon layer deposition and preprocessing (chemistries and their sequence).

Choosing appropriate initial thickness, annealing temperature, and time while controlling oxygen supply sources (also on the level of silicon substrate preprocessing and deposition method and its conditions) should allow achieving repetitive results of otherwise very difficult to obtain structures.

It has to be underlined that this requires individual optimization process, as the kinetics of nanocrystalline phase oxidation at some moment begins to depend on the used methods of silicon layer deposition and preprocessing steps.

It also seems justified to conclude that PECVD Si ultrathin layers manufactured for the purpose of this study exhibit much smaller internal strain than the ones fabricated by magnetron sputtering method. This, in turn, results in lower crystallization temperature favoring this process vs. oxidation and in consequence increasing the technological window for separation of recrystallization from oxidation in temperature and time domains.

Data Availability

The data are collected and archived at the Institute of Microelectronics and Optoelectronics, Warsaw University of Technology, as a part of documentation of results achieved during two research projects, funded via National Grants by the National Science Centre-DEC-2011/03/B/ST702595 (UMO-2011/03/B/ST7/02595) and funded by the National Centre for Research and Development (NCBiR) under grant no. V4-Jap/3/2016 (“NaMSeN”) in the course of “V4-Japan Advanced Materials Joint Call,” as well as during diploma work of Kamil Ber.

Disclosure

This paper is developed from the conference abstract presented on the 2016 Joint International EUROSIOI Workshop and International Conference on Ultimate Integration on Silicon.

Conflicts of Interest

The authors declare that they have no conflicts of interest.

Acknowledgments

This work was partly funded via National Grants by the National Science Centre-DEC-2011/03/B/ST702595 (UMO-2011/03/B/ST7/02595) and partly by the National Centre for Research and Development (NCBiR) under grant no. V4-Jap/3/2016 (“NaMSeN”) in the course of “V4-Japan Advanced Materials Joint Call.” The authors acknowledge all the valuable feedbacks received at the conference.

References

- [1] L. Mangolini, “Synthesis, properties, and applications of silicon nanocrystals,” *Journal of Vacuum Science & Technology B*, vol. 31, no. 2, pp. 020801–020829, 2013.
- [2] M. Zacharias, J. Bläsing, K. Hirschman, L. Tsybeskov, and P. M. Fauchet, “Extraordinary crystallization of amorphous Si/SiO₂ superlattices,” *Journal of Non-Crystalline Solids*, vol. 266–269, pp. 640–644, 2000.
- [3] S. Hazra, I. Sakata, M. Yamanaka, and E. Suzuki, “Stress as a governing parameter to control the crystallization of amorphous silicon films by thermal annealing,” *Applied Physics Letters*, vol. 80, no. 22, pp. 4115–4117, 2002.
- [4] D. J. Lockwood, G. F. Grom, L. Tsybeskov et al., “Self-organization and ordering in nanocrystalline Si/SiO₂ superlattices,” *Physica E: Low-dimensional Systems and Nanostructures*, vol. 11, no. 2–3, pp. 99–103, 2001.
- [5] K. Ber and R. B. Beck, *Analysis of competing processes of oxidation and recrystallization of amorphous silicon layers in double dielectric barrier ultra-thin structures, presented at 18th Workshop in Microelectronics - WODIM 2014 in Cork, 2014.*
- [6] R. B. Beck and K. Ber, “Ellipsometric spectroscopy as a tool for investigation of nanocrystals in ultrathin PECVD silicon layers’ behavior during high temperature annealing,” in *European Materials Research Society 2016 Fall Meeting (E-MRS 2016 Fall Meeting)*, Warsaw, Poland, September 2016.
- [7] R. Mroczynski and R. B. Beck, “Application of plasma enhanced chemical vapor deposition silicon oxynitride layers in nonvolatile semiconductor memory devices,” *Journal of Vacuum Science & Technology B: Microelectronics and Nanometer Structures*, vol. 27, no. 1, pp. 494–497, 2009.
- [8] K. Ber and R. B. Beck, “Formation of ultrathin silicon layers by PECVD and their modification for nanoelectronic and nanophotonic applications,” in *Proc. SPIE 8902, Electron Technology Conference 2013*, Ryn, Poland, July 2013.
- [9] A. H. Jayatissa, M. Suzuki, Y. Nakanishi, and Y. Hatanaka, “Ellipsometric study of thermal and laser annealed amorphous and microcrystalline silicon films,” *Applied Surface Science*, vol. 92, pp. 300–305, 1996.
- [10] S. Charvet, R. Madelon, F. Gourbilleau, and R. Rizk, “Spectroscopic ellipsometry analyses of sputtered Si/SiO₂ nanostructures,” *Journal of Applied Physics*, vol. 85, no. 8, pp. 4032–4039, 1999.
- [11] P. Petrik, W. Lehnert, C. Schneider et al., “In situ measurement of the crystallization of amorphous silicon in a vertical furnace using spectroscopic ellipsometry,” *Thin Solid Films*, vol. 383, no. 1–2, pp. 235–240, 2001.
- [12] https://www.horiba.com/en_en/spectroscopic-ellipsometry/.
- [13] S. Hernandez, A. Martínez, P. Pellegrino et al., “Silicon nanocluster crystallization in SiO_x films studied by Raman scattering,” *Journal of Applied Physics*, vol. 104, no. 4, article 044304, 2008.
- [14] J. Lopez-Vidrier, S. Hernández, D. Hiller et al., “Annealing temperature and barrier thickness effect on the structural and optical properties of silicon nanocrystals/SiO₂superlattices,” *Journal of Applied Physics*, vol. 116, no. 13, p. 133505, 2014.
- [15] R. B. Beck, “Formation of ultrathin silicon oxides—modeling and technological constraints,” *Materials Science in Semiconductor Processing*, vol. 6, no. 1–3, pp. 49–57, 2003.

- [16] M. Y. Chan and P. S. Lee, "Fabrication of silicon nanocrystals and its room temperature luminescence effects," *International Journal of Nanoscience*, vol. 05, no. 04n05, pp. 565–570, 2006.
- [17] L. Tsybeskov, G. F. Grom, M. Jungo et al., "Nanocrystalline silicon superlattices: building blocks for quantum devices," *Materials Science and Engineering: B*, vol. 69-70, pp. 303–308, 2000.
- [18] M. Zacharias, J. Bläsing, P. Veit, L. Tsybeskov, K. Hirschman, and P. M. Fauchet, "Thermal crystallization of amorphous Si/SiO₂ superlattices," *Applied Physics Letters*, vol. 74, no. 18, pp. 2614–2616, 1999.
- [19] M. Zacharias and P. Streitenberger, "Crystallization of amorphous superlattices in the limit of ultrathin films with oxide interfaces," *Physical Review B*, vol. 62, no. 12, pp. 8391–8396, 2000.
- [20] J. Nulman, "Rapid thermal growth of thin silicon dielectrics for ULSI applications," *Proceedings of the First International Symposium on Ultra Large Integration Science and Technology: ULSI Science and Technology/1987; Electrochemical Society Incorporated*, pp. 141–154, 1987.
- [21] R. B. Beck and B. Majkusiak, "The initial growth rate of thermal silicon oxide," *Physica Status Solidi (a)*, vol. 116, no. 1, pp. 313–329, 1988.